Diss. ETH Nr. 8061

PALEOMAGNETIC AND MAGNETIC ANISOTROPY TECHNIQUES
APPLIED TO
TECTONICALLY DEFORMED REGIONS

A dissertation submitted to the

SWISS FEDERAL INSTITUTE OF TECHNOLOGY ZURICH

for the degree of

Doctor of Natural Sciences

presented by

ANN MARIE HIRT-TASILLO

M.Sc. Geology, University of Toronto

born on July 6, 1955
Citizen of the U.S.A. and Switzerland, Stilli, Aargau

accepted on the recommendation of

Prof. Dr. W. Lowrie, examiner

Prof. Dr. J. G. Ramsay, co-examiner

PD Dr. F. Heller, co-examiner

1986

TABLE OF CONTENTS

ABSTRACT

Paleomagnetic techniques and analysis of the anisotropy of magnetic susceptibility (AMS) have been applied to several tectonic problems in order to gain a better understanding of how the magnetization of rocks is affected by tectonic deformation. Two paleomagnetic studies were done in geologic areas which have different tectonic histories. The first study uses the paleomagnetic vectors to analyze the origin of curvature of the Northern Apennine mountains in the Umbria-Marches region. Oroclinal bending of the fold belt had been inferred by earlier paleomagnetic results from the upper Cretaceous Scaglia formation. Characteristic remanent magnetization (ChRM) directions were defined for twenty-six new sites in the early Cretaceous Majolica formation that were located throughout the fold belt. These data, along with data from five previously studied magnetostratigraphic sections, show an insignificant correlation between the fold axes and the paleomagnetic vectors. From this is deduced that the curvature of the fold belt is primary. The mean direction of the sites from the Majolica formation agrees with measured directions in Istria and Gargano, autochthonous areas of the Adriatic promontory. Although the Umbria-Marches region had suffered thrust décollement on the underlying Triassic evaporites during the late Tertiary orogeny, this was not accompanied by large-scale rotation or translation relative to the Adriatic promontory.

The second paleomagnetic study examines the effects of deformation on the remanent magnetization in the Lower Glarus nappe complex of the Helvetics in eastern Switzerland. The rocks of this area have undergone extreme deformation. An estimation of the amount and the orientation of this deformation would be useful in the analysis of the paleomagnetic information. The AMS was measured at twenty-seven sites located in the Permian-Triassic red beds of the Lower Glarus Nappe complex. The finite strain was calculated at twelve of these sites from reduction spots measured on three nonperpendicular planes. The orientations of the principal axes of the susceptibility magnitude and finite strain ellipsoids were in good agreement. The ellipsoids are flattened in the cleavage plane and a north-south lineation was defined. The principal axes of the two ellipsoids can be correlated with one another in several ways. Five methods of correlation were evaluated and compared, and for one method the AMS provides an accurate approximation of the finite strain. Based on this

correlation, AMS data were then used to define the orientations and magnitudes of the finite strain at each site in the nappe complex.

Paleomagnetic directions were evaluated at fifteen sites in the Lower Glarus Nappe complex. Both secondary and characterisitic components of magnetization were isolated. Although the secondary directions of the sites were scattered, they may have been acquired during the Alpine deformation in the Oligocene - Miocene. The ChRM directions display a large between-site scatter. AMS results suggest that hematite, which is the only magnetic carrier, has been statistically realigned within the cleavage plane. The expected Permian-Triassic direction has been affected by the Alpine deformation. The ChRM directions are streaked along a great circle, away from the expected Permian-Triassic direction of magnetization. This spread can be explained by a penetrative simple shear deformation associated with the nappe-internal deformation.

In the final study, AMS was used to help define the strain in the Sudbury Basin, which is located in the Canadian Shield. The basin is believed to have been formed by a meteorite impact, and its circular cross-section has been subsequently deformed into its present elliptical shape. Sixteen sites were sampled in the Chelmsford formation and the finite strain was measured directly at ten of these sites, using concretions as strain markers. Corresponding principal axes of the finite strain and susceptibility magnitude ellipsoids were coaxial. The magnetic fabric is similar throughout the Chelmsford formation: the minimum axes of the susceptibility were subnormal to the cleavage plane or parallel to the short axis of the basin; and the magnetic foliation plane had a trend which is subparallel to the long axis of the basin. Three of the correlation methods defined in the Glarner Alps study provided good approximations of the finite strain.

The AMS was also measured for nineteen sites in the Onaping breccia of the Sudbury Basin. The sites showed a gradual change in their magnetic fabric with increasing deformation, where sites in the northwest are relatively undeformed and their magnetic susceptibility is isotropic and where sites in the southwest have a fabric controlled by the cleavage. Mineral fragments in the breccia are possible strain markers for the Onaping. To extend the Onaping microfabric results to finite strain for the basin more must be known about the validity of correlating AMS and microfabric data. The legitimate use of such a correlation to determine finite strain for a site has never been completely evaluated. A preliminary test was made using a microfabric in the Chelmsford formation, defined by quartz

grains which have been deformed through pressure dissolution. This microfabric was correlated for several specimens with the AMS of these same specimens. The AMS of all the individual specimens at a site were then converted into an equivalent strain, using this correlation. The site mean strain derived from all the specimens is in good agreement with the total finite strain derived from the concretions. The correlation of the AMS with a microfabric appears to be a valid method to calculate a representative strain for an entire site.

Seite Leer /
Blank leaf

ZUSAMMENFASSUNG

Paläomagnetische Methoden und die Analyse der Anisotropie der magnetischen Suszeptibilität (AMS) wurden auf mehrere tektonische Probleme angewendet, um ein besseres Verständnis darüber zu erhalten, wie der Gesteinsmagnetismus durch tektonische Verformung beeinflusst wird. Zwei paläomagnetische Studien wurden in Gebieten mit unterschiedlicher tektonischer Geschichte ausgeführt. Die erste Studie benützt paläomagnetische Vektoren zur Bestimmung der Ursache der Krümmung der nördlichen Appenninen in der Region Umbrien-Marche. Frühere paläomagnetische Resultate aus der Scaglia-formation (Obere Kreide) lassen auf oroklinale Krümmung des Faltengürtels schliessen. Die Richtung der charakteristischen remanenten Magnetisierung (ChRM) wurde für 26 neue Lokalitäten, verteilt über den ganzen Faltengürtel der Majolica-formation (Untere Kreide), bestimmt. Diese Daten, zusammen mit Resultaten von fünf vorgängig studierten magnetostratigraphischen Sektionen, zeigen keine signifikante Korrelation zwischen den Faltenaxen und den paläomagnetischen Vektoren. Dies bedeutet, dass die Krümmung des Faltengürtels primären Ursprungs ist. Der Mittelwert der Richtungen aller Lokalitäten der Majolica-formation stimmt überein mit den in den autochthonen Gebieten des adriatischen Sporns Istria und Gargano gemessenen Richtungen. Obwohl die Region Umbrien-Marche während der Gebirgsbildung im späten Tertiär entlang von triassischen Evaporithorizonten abgeschert wurde, fand während dieses Prozesses keine bedeutende Rotation oder Verschiebung relativ zum adriatischen Sporn statt.

Die zweite paläomagnetische Studie befasst sich mit dem Einfluss der tektonischen Verformung auf die remanente Magnetisierung im unteren Glarus-deckenkomplex der Helvetischen Alpen in der Ostschweiz. Die Gesteins-formationen dieses Gebietes wurden extremen Verformungen unterworfen. Eine Abschätzung des Ausmasses und der Richtung dieser Verformungen wäre nützlich für die Analyse der paläomagnetischen Daten. Zu diesem Zweck wurde die AMS von 27 Lokalitäten in den permotriassischen Rotserien des unteren Glarus-deckenkomplexes gemessen. Für zwölf dieser Lokalitäten wurde die finite Verformung, basierend auf Messungen von Reduktionsflächen in drei nicht orthogonalen Ebenen, berechnet. Die Orientierung der Hauptachse des Betragsellipsoids der Suszeptibilität und des finiten Verformungsellipsoids zeigten gute Uebereinstimmung. Die Ellipsoide sind in der Schieferung abgeplattet und

weisen ein Nord-Süd-linear auf. Die Hauptachsen der Ellipsoide können nach verschiedenen Methoden korreliert werden. Fünf Korrelationsmethoden wurden evaluiert und miteinander verglichen, wobei es sich zeigte, dass eine der fünf Methoden eine genaue Abschätzung der finiten Verformung mit Hilfe der AMS ermöglicht. Gestützt auf diese Korrelationsmethode wurden dann die Richtung und der Betrag der finiten Verformung für jede Lokalität im Deckenkomplex aus den AMS-messungen abgeleitet.

Die paläomagnetischen Richtungen für fünfzehn Lokalitäten im unteren Glarus-deckenkomplex wurden bestimmt. Sekundäre und charakteristische Komponenten der Magnetisierung wurden identifiziert. Trotz einer gewissen Streuung der Sekundärrichtungen verschiedener Lokalitäten ist es möglich, dass diese Magnetisierungsrichtungen während der alpinen Verformung im Oligozän-Miozän entstanden. Die ChRM-richtungen zeigen eine grosse Streuung zwischen den Lokalitäten. Die AMS-resultate lassen darauf schliessen, dass Hämatit, welcher der einzige magnetische Träger ist, sich in der Schieferung statistisch linear orientierte. Die erwartete Perm-Trias-richtung wurde von der alpinen Deformation beeinflusst. Die ChRM-richtungen sind entlang eines Grosskreises verteilt, abgelenkt von der erwarteten Perm-Trias-magnetisierungs-richtung. Diese Verteilung ist zu erwarten, wenn man eine durchdringende einfache Scherverformung in Zusammenhang mit der inneren Deckenverformung annimmt.

In einer weiteren Studie wurde mit Hilfe der AMS die Verformung des Sudbury-beckens innerhalb des Kanadischen Schilds bestimmt. Es wird angenommen, dass das Becken durch den Einschlag eines Meteoriten entstanden ist und seine ursprüngliche Kreisform durch nachträgliche Verformung in die gegenwärtige elliptische Form überführt wurde. Von sechzehn Lokalitäten in der Chelmsford-formation wurden Proben entnommen, und die finite Verformung wurde für zehn dieser Lokalitäten an Konkretionen direkt gemessen. Die entsprechenden Hauptachsen des finiten Verformungsellipsoids und des Betragsellipsoids der Suszeptibilität sind koaxial. Die magnetische Textur der Chelmsford-formation ist überall ähnlich: die Minimalachsen der Suszeptibilität sind normal zur Schieferung oder parallel zur kurzen Achse des Beckens; die magnetische Foliationsebene hat eine parallele Orientierung zur langen Achse des Beckens. Drei Korrelationsmethoden, welche in der Studie über den Glarus-deckenkomplex vorgestellt wurden, ergaben eine gute Abschätzung der finiten Verformung mittels der gemessenen AMS.

AMS-messungen wurden auch für zwanzig Lokalitäten in den Onaping-brekzien des Sudbury-beckens ausgeführt. Diese zeigen eine graduelle Veränderung in der magnetischen Textur mit ansteigendem Deformationsgrad. Lokalitäten im nord-westlichen Teil sind relativ wenig verformt, und die magnetische Suszeptibilität ist isotrop, während die Textur im süd-östlichen Teil von der Schieferung bestimmt ist. Mineralische Fragmente in den Brekzien sind mögliche Indikatoren für die Verformung in der Onaping-formation. Um die Resultate über die mikroskopische Textur auf die finite Verformung des Beckens ausdehnen zu können, müsste mehr über die Gültigkeit der Korrelation der AMS und der mikroskopischen Textur bekannt sein. Die Zuverlässigkeit solcher Korrelationsmethoden zur Bestimmung der finiten Verformung einer Lokalität wurde noch nie umfassend geprüft. Ein Vorversuch wurde durchgeführt unter Benützung einer mikroskopischen Textur des Chelmsford-gebietes bestehend aus Quartzkörnern, welche durch Drucklösung verformt wurden. Die mikroskopische Textur verschiedener Proben wurde mit der AMS der gleichen Proben korreliert. Von den Korrelationsresultaten wurde mittels der Werte der AMS für jede Probe einer bestimmten Lokalität eine äquivalente Verformung abgeleitet. Der Mittelwert der Verformung aller Proben der Lokalität ist in guter Uebereinstimmung mit der totalen finiten Verformung, welche von den Konkretionen abgeleitet wurde. Dieses Resultat unterstützt die These, dass die Korrelation der AMS mit einer mikroskopischen Textur eine gültige Methode zur Berechnung der representativen Verformung für eine ganze Lokalität darstellt.

Seite Leer /
Blank leaf

ACKNOWLEDGEMENTS

Seite Leer /
Blank leaf

NOTATION

Symbols are defined the first time they occur. The following are commonly used:

NRM   - natural remanent magnetization

IRM   - isothermal remanent magnetization

CRM   - chemical remanent magnetization

ChRM - characteristic remanent magnetization

AMS   - anisotropy of magnetic susceptibility

M   - intensity of magnetization

M_s - saturation or spontaneous magnetization

M_o - intensity of the natural remanent magnetization

H   - magnetic field

H_c - coercive force

H_{cr} - coercivity of the maximum remanence

AF   - alternating field (demagnetization)

k   - susceptibility

k_{max} - maximum axis of the susceptibility magnitude ellipsoid, also expressed as k_1

k_{int} - intermediate axis of the susceptibility magnitude ellipsoid, also expressed as k_2

k_{min} - minimum axis of the susceptibility magnitude ellipsoid, also expressed as k_3

$\bar{k}$ - mean susceptibility, $(k_1 k_2 k_3)^{1/3}$

ε_i' - $\ln(X_i/\bar{X})$ for i = 1 to 3, where X_i are the principal axes of the finite strain ellipsoid, also expressed as X, Y and Z with X<Y<Z and $\bar{X} = (X_1 X_2 X_3)^{1/3}$

s.d.   - standard deviation

All measurements are expressed in S.I. units of magnetic induction (B, Tesla) and magnetic dipole moment (M, A/m).

Chapter 1. INTRODUCTION

1.1 Some Applications of Paleomagnetism in Tectonic Studies

Paleomagnetism has long been recognized as a method to study large scale tectonic problems. In 1926, Mercanton first suggested that paleomagnetism could be a useful tool in testing Wegener's hypothesis of polar wander and continental drift (McElhinney, 1973). Although Mercanton's idea was not explored immediately, enough paleomagnetic data had been collected by 1960 to support the conclusion that the continents had moved from their present positions (Cox and Doell, 1960). Since 1960, numerous paleomagnetic studies have established an apparent polar wander (APW) path for each continent (Irving, 1977, 1979; Morel and Irving, 1978; Smith et al., 1981).

Many plate motions predicted by paleomagnetic studies can be verified from the oceanic magnetic anomalies. One example in which paleomagnetic data suggested large scale plate motion over a short period of time involves the Indian subcontinent. India was part of the Gondwana supercontinent during the Mesozoic, and was located between 50°S and 20°S latitude. With the start of the split up of eastern Gondwana from western Gondwana in the Late Jurassic, India proceeded to move northward at rates of 15-20 cm/year (Klootwijk, 1979a). Collision with Eurasia occurred approximately 55 Ma ago at 7-10°N latitude (Figure 1.1a). This is further south than the former southern boundary of Eurasia predicted by Irving (1977). Klootwijk (1979b) suggested from his paleomagnetic investigations in Ladakh that the northward convergence of the Indian subcontinent with Eurasia has continued over 2500km from 55 Ma until the present (Figure 1.1b).

Paleomagnetism has been useful in determining the role of the Adriatic promontory in Mediterranean plate motions (Channell and Horváth, 1976; Van den Berg et al., 1978; Channell et al., 1979; Lowrie, 1980, 1986). The promontory is defined by the distribution of the northern and southern Tethyan facies types, ophiolites and earthquake epicenters. It includes Sicily, peninsular Italy, the Southern Alps and Istria.

The autochthonous areas of the Adriatic promontory are characterized by paleomagnetic directions which are consistent among each other. These directions are significantly more westerly than contemporaneous directions for the stable European continent, but are similar to African directions of the same age (Figure 1.2). This suggests that the movement of the
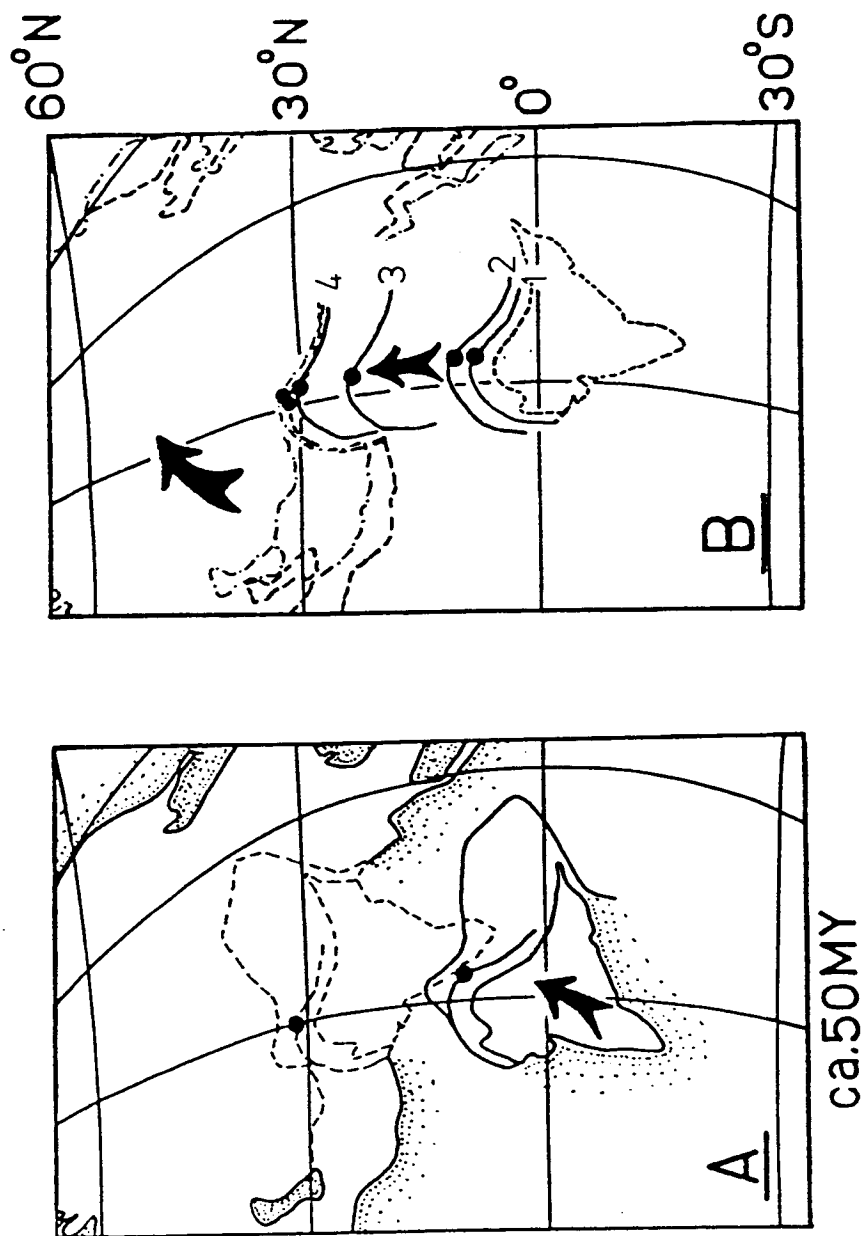
Figure 1.1. A.) Position of the Indo-Pakistan subcontinent at the time of collision with Eurasia as compared to the contemporaneous paleoposition of Eurasia predicted by Irving (1977). B.) Proposed subsequent paleopositions of the Indo-Pakistan subcontinent from paleomagnetic data of the Ladakh volcanics. Explanation of numbers: 1.) and 2.) Early-Middle Eocene paleoposition, 3.) Miocene paleoposition, and 4.) Recent position of the subcontinent. The Eurasian paleoposition is given by the dashed line for 50Ma and by the dashed-dot line for 20 Ma (Irving,1977). (From Klootwijk, 1979b).
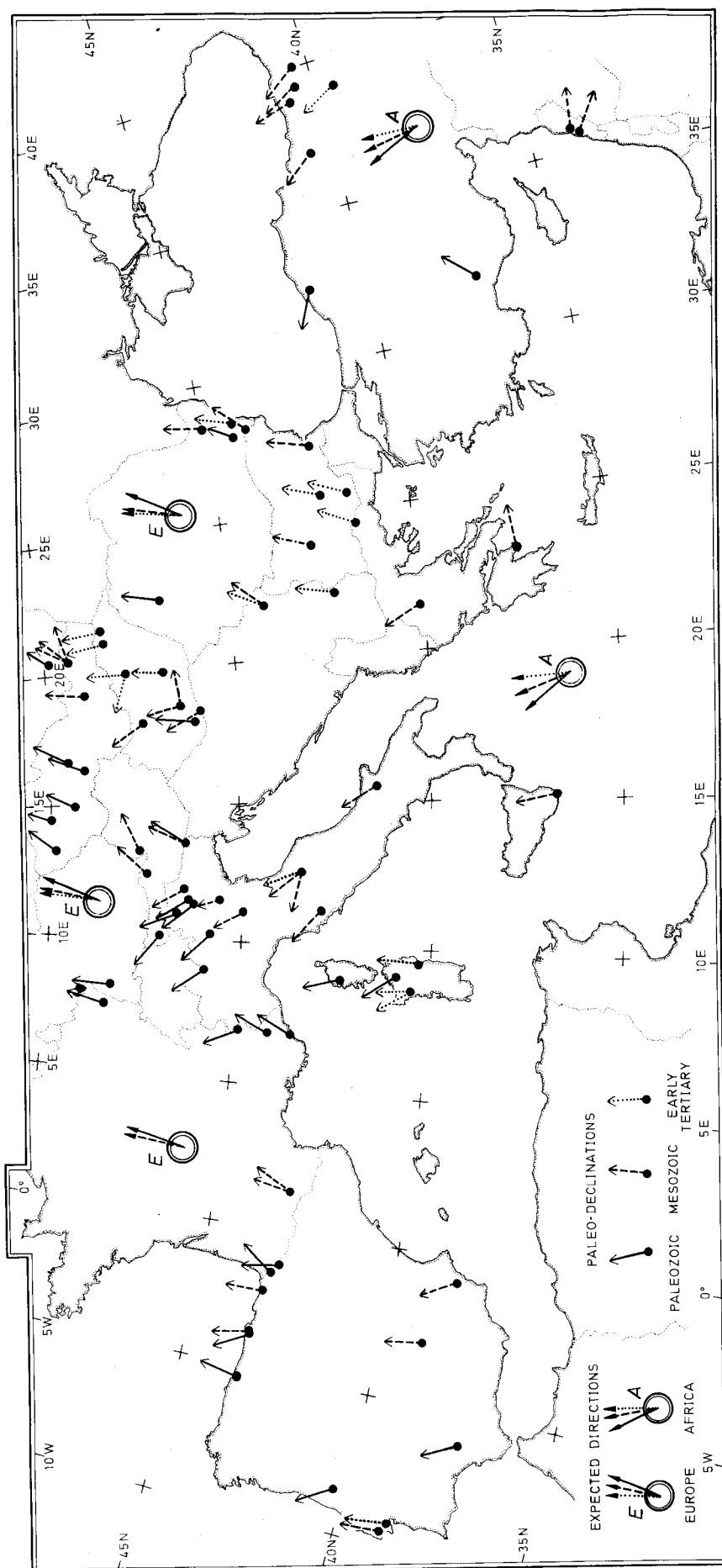
Figure 1.2. Map of the Mediterranean area with paleomagnetic declinations for sites on the Adriatic promontory and stable Europe, as well as declinations for Africa and Europe derived from their predicted pole positions in the Paleozoic, Mesozoic and Early Tertiary. (From Lowrie, 1980).

promontory was related to African plate motion (Van den Berg et al., 1978). Differences between virtual geomagnetic poles of Africa and the Adriatic promontory imply that parts of the promontory have been subsequently rotated relative to Africa during the Alpine orogeny (Lowrie, 1986).

There have been numerous paleomagnetic studies in the past fifteen years which have used paleomagnetic directions to account for rotations of small intra-continental blocks. Heller (1980) examined granites of the Lepontine area of the central Swiss Alps. These rocks were remagnetized by high grade regional metamorphism during the Alpine orogeny between the late Eocene and early Miocene. The stable characterisitic remanent magnetization (ChRM) directions for this area were found to be rotated by $27^{\circ} \pm 13^{\circ}$ anticlockwise from the predicted direction for stable Europe (Figure 1.3). The ChRM directions from the Aar massif to the north of the Lepontine area were close to the predicted European direction. Heller (1980) suggested that the Lepontine area, bounded by two major fault systems, one to the north and the other to the south, has undergone counterclockwise rotation due to dextral motion on these fault lines.

Geissman et al. (1980) used paleomagnetic directions to show that the regional rotation interpreted by structural geologists in the Butte Mining District of Montana was questionable. The Late Cretaceous Butte quartz monzonite was previously believed to have been tilted 40° to 60° towards the northwest, as suggested by field relations. However, ChRM directions of the Late Cretaceous units in the Butte district and from the quartz monzonite are found to correspond approximately to the predicted Late Cretaceous directions of North America. Therefore the paleomagnetic data indicate that there may be some local or regional tilting in the Butte district, but that it would be less than 15°, rather than 40° to 60° predicted by the structural geologists.

Paleomagnetism can be a very useful tool in determining the origin of curvature in mountain belts. If the ChRM directions predate the deformation of the fold belt, they can indicate if the curvature was primary or if the belt has been subsequently bent. Several authors have discussed the application of paleomagnetic data to curved mountain belts throughout the world (Van der Voo and Channell, 1980; Schwartz and Van der Voo, 1983; Eldredge et al., 1985). Many problems exist in doing paleomagnetism in deformed areas; an exact knowledge of the structural geologic setting, age of the rocks and age of the magnetization is essential before any conclusions about the curvature can be made (Lowrie and Hirt, 1986).
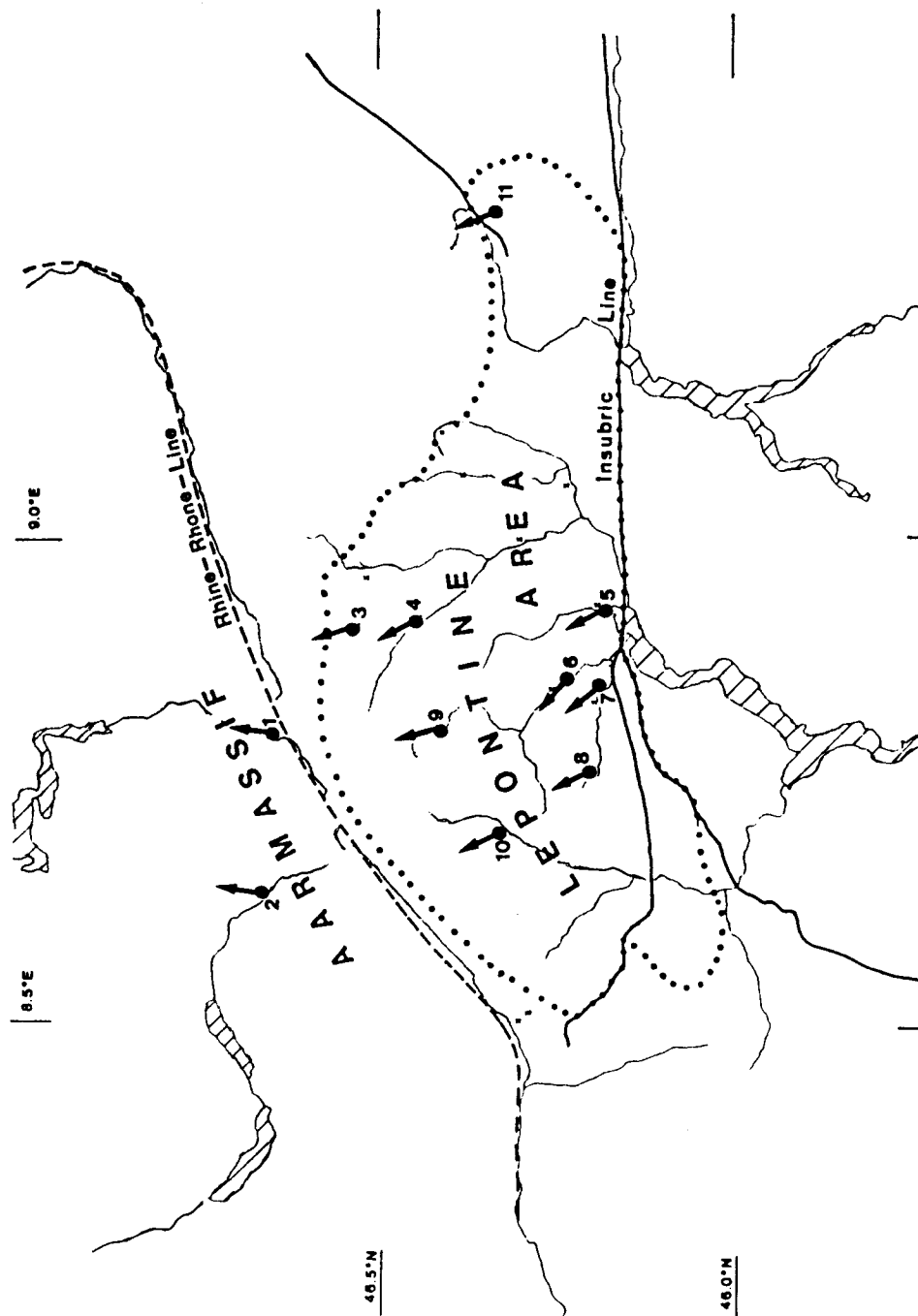
Figure 1.3. Paleomagnetic declinations in the Lepontine area and the Aar Massif, Switzerland. (From Heller, 1980).

It is also possible to study local tectonic problems using paleo-magnetism. Alvarez and Lowrie (1984) were able to show that slumped beds in the Furlo magnetostratigraphic section in the Umbria-Marches region of the northern Apennines possessed ChRM directions which were typical for a regional direction from the Umbria-Marches region. Coherent blocks between the slumped beds, however, had directions which were rotated approximately 60° counterclockwise from directions below the slumped area (Figure 1.4). The authors suggested that these blocks were coherent during the synsedimentary slumping and were rotated as a result of motion of the slumped beds.

1.2 Applications of Magnetic Susceptibility Anisotropy in Tectonic Problems

The anisotropy of magnetic susceptiblity (AMS) was first recognized as a tool to identify petrographic features. Balsley and Buddington (1960) found that the magnetic foliation and lineation in orthogneisses in the northwestern Adirondacks paralleled those seen in hand specimens. They also found that rocks which had no visible foliation or lineation also possessed a magnetic foliation, hence a preferential alignment of the magnetic minerals.

Fuller (1963) explored the contribution of pyrrhotite, hematite and magnetite to the magnetic fabric of Welsh slates. Pyrrhotite, in its pseudohexagonal habit, aligns its basal plane within the cleavage plane. The minimum susceptibility is normal to the basal plane, and the maximum and intermediate axes of susceptibility lie within the high-susceptibility basal plane with their orientations being dependent on the shape of the plane (Uyeda et al., 1963). Hematite platelets also align themselves within the cleavage plane, with the minimum axes of susceptibility normal to this plane. There is, however, no variation of the susceptibility within the basal plane. Magnetite is dominated by a shape anisotropy, such that the maximum and intermediate susceptibility axes lie within the cleavage plane of the slates and the minimum axes are normal to cleavage. Fuller (1964) later found that small-scale stress environments within a rock are the important controlling factor of the magnetic fabric.

Graham (1966) showed that AMS could be used as an indicator of finite strain. The principal axes of the susceptibility magnitude ellipsoid parallel the principal axes of the finite strain ellipsoid. The magnitude ellipsoid was found to change its shape and orientation with progressive deformation

Figure 1.4. Section of the Scaglia Bianca and Scaglia Rossa limestones along the Furlo Upper road which shows location of slumped beds and rotated paleomagnetic directions. (From Alvarez and Lowrie, 1984).

in sedimentary rocks from the Appalachians (Figure 1.5). Undeformed sediments originally possess an oblate ellipsoid, with the minimum axes of susceptibility (k_{min}) normal to the bedding plane as a result of compactional shortening. Applying uniform compression parallel to the bedding plane, the beds will shorten and the maximum axes of suscepti-bility (k_{max}) will orient themselves perpendicular to the direction of shortening. With further shortening the oblate ellipsoid will become pro-late as a result of the superposition of two flattenings subnormal to one another. The ellipsoid then proceeds to become oblate again, but now flattened normal to the direction of shortening. The k_{min} axes are normal to the cleavage plane and the k_{max} axes parallel the direction of elongation. Further studies examining the relationship between finite strain and magnetic fabrics include Kneen (1976) in shales and slates, Hrouda (1976) and Hrouda and Janák (1976) in metamorphosed sediments, and Kligfield et al. (1977) in volcanics and sediments of the Sudbury basin.

Wood et al. (1976) suggested that a quantitative relationship exists between the magnitudes of both the finite strain and the susceptibility principal axes. Further studies by Rathore (1979, 1980), Hrouda (1979), Rathore and Henry (1982) and Kligfield et al. (1982) confirmed this re-lationship for several different rock types. Kligfield et al. (1981, 1983) extended this quantitative relationship to red mudstones of the Maritime Alps, in which the finite strain and AMS magnitude ellipsoids change with progressive deformation, as predicted by Graham (1966) (Figure 1.6).

When a rock is deformed the minerals within the rock can be reoriented, including the ferromagnetic minerals. This in turn can modify the existing remanent magnetization of the rock. The orientation of the ferromagnetic minerals depends on the strain response model. Such models have been described by March (1932), Owens (1974), Willis (1977), Harvey and Laxton (1980) and Cogné and Gapais (1986). Owens (1974) provides a description of three common strain response models. The simplest is that of March (1932) in which the ferromagnetic grains do not change shape but rotate their positions and reorient themselves as passive linear or planar elements in a ductile matrix. The second model also assumes that the grains rotate without changing shape, but in a viscous fluid. A perfectly passive behavior would require the ferromagnetic grains to change not only their orientation but also their shapes. In this third model the grains would be passively deformed with their surrounding ma-trix. Further mathematical descriptions of the relationship between finite
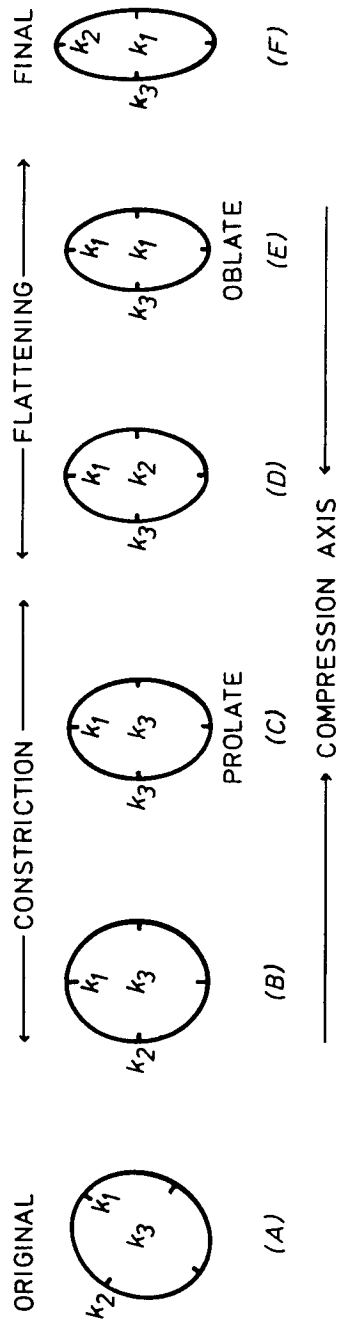
Figure 1.5. Change in the susceptibility magnitude ellipsoid with progressive deformation. The ellipsoid is originally flattened in the bedding plane, which is the plane of the figure. The center of the ellipsoid is the normal to the bedding plane. $k_1 = k_{max}$, $k_2 = k_{int}$ and $k_3 = k_{min}$. (After Graham, 1966).
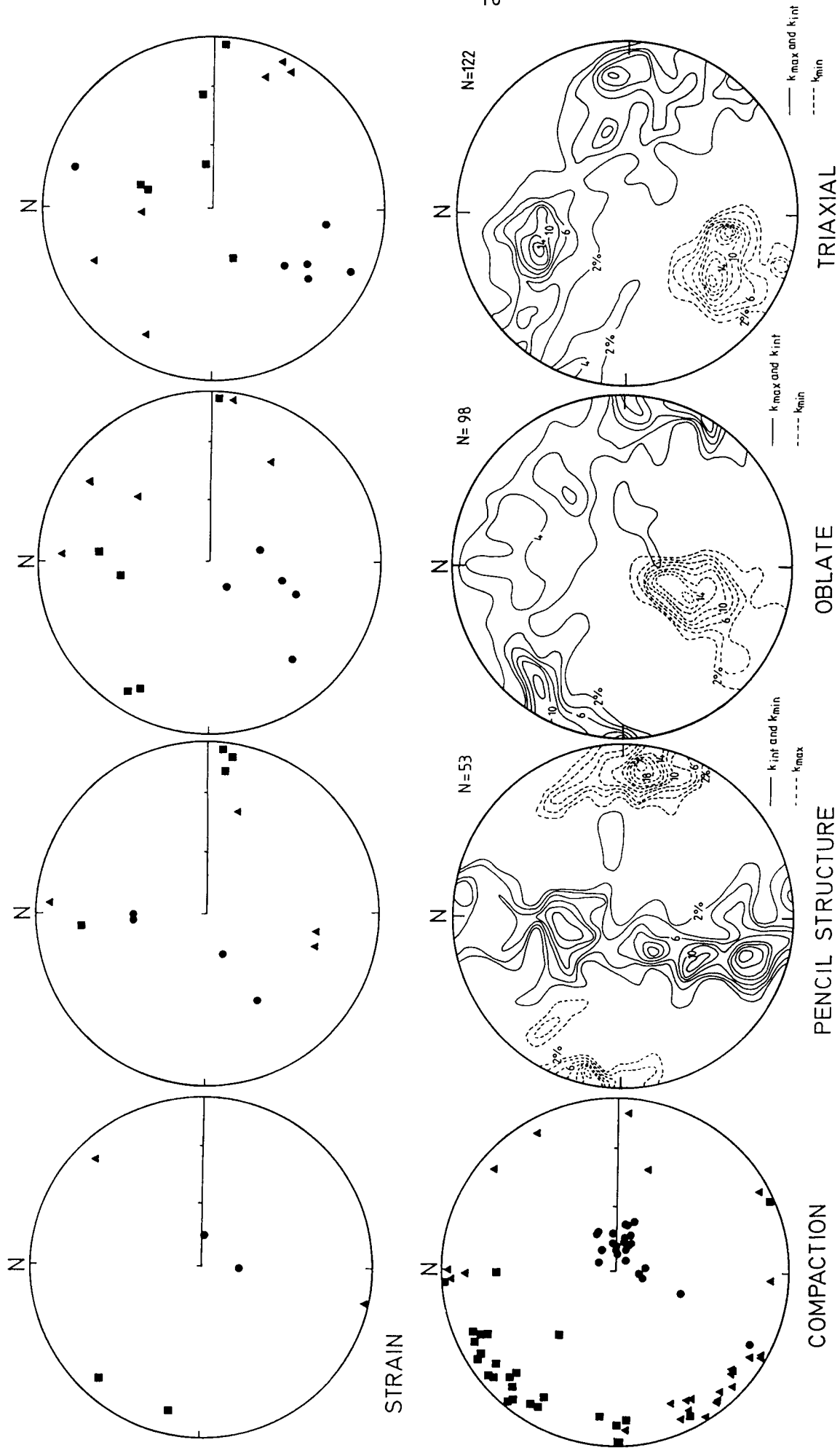
Figure 1.6. Comparison between the finite strain principal axes (X > Y > Z) and the principal axes of the susceptibility magnitude ellipsoid for four stages of progressive deformation. Squares represent X-axes of the strain and k_{max} axes of the susceptibility, triangles represent Y-axes and k_{int} axes, and circles represent Z-axes and k_{min} axes. (From Kligfield et al., 1983).

strain and the magnetic fabric have been given by Owens and Bamford (1976) and Hrouda (1976, 1979).

Attempts to correct remanent magnetization for the effect of strain in deformed rocks have been made by Kligfield et al. (1983) and Cogné and Perroud (1985), using the March model. Although the model appears to predict the behavior of ferromagnetic grains in model studies (Cogné and Gapais, 1986), it is not yet known how widespread this strain-correcting method is applicable (Lowrie et al., 1986).

1.3 Scope of Thesis

The purpose of this dissertation is to investigate structural problems with both paleomagnetic and AMS methods. The thesis contains two paleomagnetic studies. The first study uses paleomagnetism in a classical sense to determine regional-scale deformation in a curved mountain belt. The second study examines paleomagnetic directions to gain insight about how the remanent magnetization vectors were affected by deformation. The area was deformed predominantly from simple shear. In order to analyze the effect of this simple shear on the remanence, an estimation of the deformation was made at each paleomagnetic site. A finite strain - AMS correlation was established so that an equivalent finite strain could be defined at sites without strain markers.

Borradaile and Mothersill (1984) criticized a correlation between the principal axes of the finite strain and susceptibility magnitude ellipsoids in volcanic rocks from the Borrowdale volcanics (Rathore, 1980). They found no correlation between individual principal axes, i.e, k_{max} and maximum natural strain, k_{int} and intermediate natural strain, or k_{min} and minimum natural strain. Only a comparison of these three sets of data together yielded a well-defined linear regression (Figure 1.7). They argued that this regression is biased to be artificially significant since the data fall into three clusters. This problem is examined in the rocks which are investigated in this study, and alternative correlations are considered. The limitation of using a finite strain - AMS correlation at high strain values is discussed. A third study also examines the finite strain - AMS correlation in an area which has undergone compression due to possible plate motion.

The thesis is divided into eight chapters. In this first introductory chapter a short and selective historical overview has been given on how magnetic methods have been used in providing information about tectonic

problems. The second chapter provides a short summary of the magnetic properties of the minerals responsible for the remanent magnetization or the anisotropy of magnetic susceptibility in the succeeding investigations. The origin of remanent magnetization and AMS relevant to these studies, is briefly discussed. A description of the methodology in field sample collecting, measurement techniques and analysis of data is given in Chapter 3.
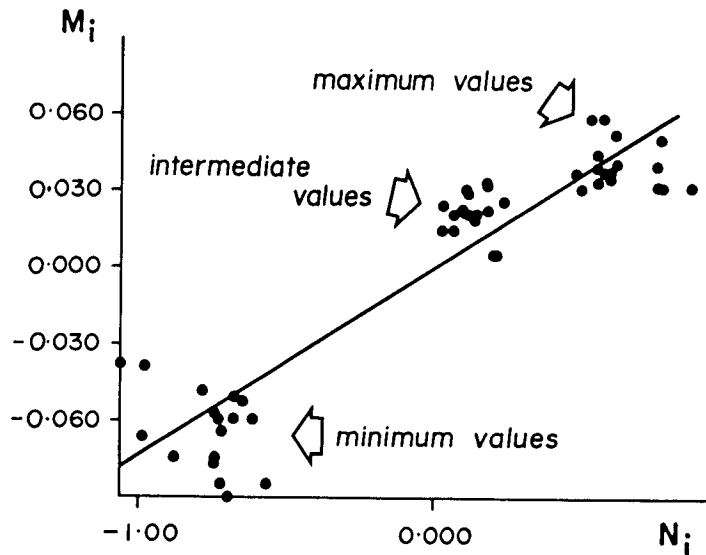
Figure 1.7. Comparison of natural strain values (N_i) with a corresponding magnetic parameter M_i defined by Rathore (1979). The regression line has a slope of 0.0739, an intercept of -0.0006 and a correlation coefficient of 0.926 which appears to be significant at the 97.5% confidence level. (From Borradaile and Mothersill, 1984).

Chapter 4 is concerned with paleomagnetic results in a curved mountain belt. Thirty-one sites are analyzed from the Lower Cretaceous Majolica formation of the Umbria-Marches region of Italy. The problem of oroclinal bending of the northern Apennines is adressed, as well as the relevance of the Umbria-Marches data to the Adriatic promontory.

In Chapter 5 the AMS and finite strain, derived from reduction spot strain markers, are compared at twenty-seven sites from the Lower Glarus Nappe complex. The directional and quantitative relationships of strain and anisotropy are discussed, and the AMS data are used to provide a more widespread picture of the strain undergone by the entire region.

A paleomagnetic study of red beds of the Lower Glarus Nappe complex in the Helvetic Alps of eastern Switzerland is described in Chapter 6. ChRM directions from fifteen sites in red sandstones and shales/slates of the Permian Verrucano and Triassic Quarten-schiefer formations are examined. The effect of simple shear deformation as a result of nappe emplacement is investigated.

Chapter 7 examines the relationship between finite strain and AMS in the Sudbury Basin, Ontario, Canada. Nineteen sites are located around the circumference of the basin in the Onaping formation and sixteen sites are located within the basin in the Chelmsford formation. A comparison of the AMS with whole-rock strain and microstrain in the Chelmsford formation is made. The main findings of this dissertation are summarized in Chapter 8.

Seite Leer /
Blank leaf

Chapter 2. THEORY

A brief summary is given of the rock magnetic theory for the magnetization of rocks and the origin of susceptibility anisotropy. General discussions on the physical theory of rock magnetism are given by McElhinney (1973) and Collinson (1983). More detailed discussions are found in Nagata (1961), Chikazumi (1964), Stacey and Banerjee (1974) and O'Reilly (1984). S.I. units are used throughout the dissertation. A description of the magnetic parameters, their units and conversion to c.g.s. units are given in Table 2.1.

2.1 Magnetization in Minerals

The magnetization of a rock consists of both an induced and a remanent part. A magnetic field applied to a rock will result in an induced magnetization, which, however, disappears when the field is removed. Any magnetization remaining after the field is removed is a remanent one. The magnetization (M) is defined as

$$M = kH ,$$ (2.1)

where H is the magnetic field and k is the magnetic susceptibility. Typical susceptibilities for ferrimagnetic minerals are $k \simeq 10^{-1}$ for magnetite, $k \simeq 10^{-3}$ for ilmenite and $k \simeq 10^{-5}$ for hematite. Other rock forming minerals, such as ferromagnesium amphiboles, pyroxenes and micas, have susceptibilities of 10^{-6} to 10^{-7} (Collinson, 1983).

For strongly magnetic minerals, M is affected by the shape of the grain. If a grain is magnetized in an applied field, then a discontinuity exists between the grain interior and exterior, where M = 0 (Figure 2.1). The discontinuity gives rise to magnetic poles at the surface of the grain, and the poles result in an internal magnetic field which is oriented in the opposing direction to the applied field. This internal field will reduce the effective total magnetization, and is therefore called the demagnetizing field, H_d; it is dependent on both the shape of the grain and on M, where

$$H_d = -NM .$$ (2.2)

N is known as the demagnetizing factor, and has been calculated for ellipsoid shapes by Stoner (1945). N can be broken down into its com-

Table 2.1. Definition and Units of Magnetic Parameters

Magnetic moment (m) - The vector associated with a magnetic grain which when placed in a uniform field, will experience a torque. This torque depends on the separation and concentration of the magnetic poles.

Magnetization (M) - Magnetic moment per unit volume of a magnetized material. It is a measure of how well the magnetic moments of the atoms of the material are aligned.

Magnetic field (H) - Space through which a magnet exerts a force or influence.

Susceptibility (k) - A measure of the ability of a material to be magnetized.

Magnetic permeability (μ) - The ratio of the magnetic induction, B, to the inducing field strength. μ_0 is the permeability of free space.

Magnetic Quantity	S.I.	c.g.s.
Magnetic moment (m)	Am^2	emu
Magnetization (M or J) $M = J/\mu_0$	M: A/m	J: emu
Magnetic field (H) (B)	A/m T	Oersted (Oe) Gauss (Gs)
Susceptibility (k or χ)	M = kH dimensionless	J = χH dimensionless
Magnetic permeability (μ)	$B = \mu_0 \mu H$ $= \mu_0(1+k)H$ $\mu_0 = 4\pi \times 10^{-7}$ Henry/m	B = H $= (1+4\pi\chi)H$ dimensionless
Magnetic Field Conversion	10^{-4}T	1 Gauss or Oe
Magnetization Conversion	1 A/m	10^{-3} emu

ponents: N_x, parallels the major axis of an ellipsoid; N_y, the intermediate axis; and N_z, the minimum axis, where $N_x + N_y + N_z = 1$. $N_x = N_y = N_z = 1/3$ for a sphere. If we have a prolate ellipsoid, H_d will be weakest along the long axis of the ellipsoid, since the pole concentration is the least and the distance between the poles is the greatest (Figure 2.1). Similarly H_d will be greatest when the magnetization parallels the short axis of the ellipsoid. Since M is constant in Equation (2.2) N must vary so that $N_x < N_y < N_z$. This shows that for an irregularly shaped grain of cubic crystallographic habit, it is easier to magnetize the grain along its long axis, because N_x is the smallest.

The energy associated with H_d is known as the magnetostatic energy. For the prolate ellipsoid ($N_x < N_y = N_z$) it can be written as

$$E_{ms} = (1/2)M_s^2 N_x + (1/2)(N_z - N_x)M_s^2 \sin^2(\theta) \qquad (2.3)$$

where M_s is the saturation magnetization and θ is the angle between M and the easy axis of the magnetization. The anisotropy energy of an uniaxial grain is

$$E_{an} = K\sin^2\theta . \qquad (2.4)$$

The second term in (2.3) has the same form as the anisotropy energy, so that the coefficient for the shape anisotorpy energy, K, can be expressed as

$$K = (1/2)(N_z - N_x)M_s^2 . \qquad (2.5)$$

K is known as the shape anisotropy constant, K_s.

In most magnetic minerals the magnetization is not governed by shape anisotropy but by magnetocrystalline anisotropy. Important minerals in this category include hematite and pyrrhotite which have hexagonal crystallographic structure. Their anisotropy results from the periodic arrangement of atoms or ions in the crystal. The electron clouds of the atoms interfere with one another as prescribed by their crystal structure, and this interference effects the magnetic properties of the mineral. The magnetocrystalline anisotropy energy of these minerals makes it easier to magnetize the mineral along certain crystallographic axes. For the hexagonal minerals, hematite and pyrrhotite, the easy axis of magnetization is in the basal planes rather than along the (0001) axes at room temper-
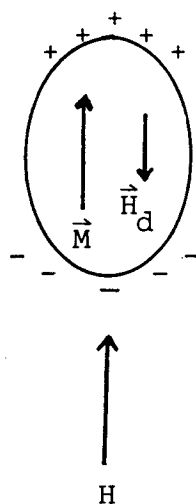
Figure 2.1. Demagnetizing field in an elliptical particle.
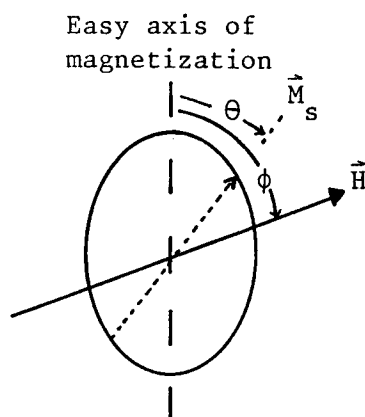
Figure 2.2. Geometry of the easy axis of magnetization, the magnetization direction (M) and the magnetic field (H).

atures. The coefficient of the anisotropy energy in Equation (2.4) is then the magnetocrystalline anisotropy constant, K_1.

2.2 Rock Magnetic Theory for Single Domain (SD) Grains

For simplicity the theory of rock magnetism is discussed for SD grains. For more details see Stacey and Banerjee (1974). If a magnetic field is applied at an angle ϕ to the easy axis of the grain, then M_s will deviate from the easy axis by an angle θ (Figure 2.2). For this case where H is not parallel to M_s, the grain has an extra energy. This energy results from the interaction of the magnetization of the grain and the external field and can be written as

$$E_{tot} = E_{an} + E_{ms}$$

$$= K\sin^2\theta - M_s H\cos(\phi-\theta) . \tag{2.6}$$

The system is in equilibrium when E_{tot} is at a minimum energy state, where

$$\frac{\partial E}{\partial \theta} = 0, \quad \text{and} \quad \frac{\partial^2 E}{\partial \theta^2} > 0 . \tag{2.7}$$

The anisotropy energy is at a minimum when M_s is parallel to the easy axis (i.e., $\theta = 0$ or π), and the magnetostatic energy is at a minimum when M_s and H have the same direction (i.e., $\phi = 0$). In the case where H is orthogonal to the easy axis, i.e., $\phi = \pi/2$, the total energy becomes

$$E_{tot} = K\sin^2\theta - M_s H\sin\theta$$

$$= \sin\theta(K\sin\theta - M_s H) . \tag{2.8}$$

Application of the conditions (2.7) to Equation (2.8) shows that the energy is at a minimum when

$$\theta = \pm\pi/2 \quad \text{and} \quad H > H_c \tag{2.9}$$

or

$$\sin\theta = \frac{M_s H}{2K} \quad \text{and} \quad H \leq H_c \qquad (2.10)$$

where

$$H_c = \frac{2K}{M_s} . \qquad (2.11)$$

H_c is the coercivity, i.e., the critical field necessary to permanently flip the direction of M_s.

For cubic minerals governed by shape anisotropy, we can substitute K from Equation (2.5) into Equation (2.11), whereby

$$H_c = (N_z - N_x)M_s . \qquad (2.12)$$

For minerals controlled by magnetocrystalline anisotropy

$$H_c = 2K_1/M_s . \qquad (2.13)$$

As seen from Equation (2.4), the magnetic energy of a uniaxial grain is only dependent on the orientation of the magnetic moment of the grain, and can be written

$$E = Kv\sin^2\theta , \qquad (2.14)$$

where v is the grain volume. In absence of a field the magnetic moment of the SD grain has a minimum energy at two orientations, $\theta = 0$ and $\theta = \pi$. The maximum energy acts as a barrier between these two positions and occurs at $\pm\pi/2$, and

$$E_r = vK . \qquad (2.15)$$

The thermal fluctuation energy, E_t, determines whether the magnetic moment can be moved from one energy minimum position to another. This is defined as

$$E_t = kT \ , \qquad\qquad (2.16)$$

where k is Boltzman's constant and T is the absolute temperature. If E_t > E_r, then the magnetic moment can spontaneously change positions.

The initial magnetization, M_o, for noninteracting, uniaxial SD grains decays exponentially by the relation

$$M_r = M_o exp(-t/\tau) \ , \qquad\qquad (2.17)$$

where M_r is the magnetization remaining after time t and τ is the relaxation time of the grains. This relaxation time is related to the energies E_r and E_t by

$$\tau = \tau_o exp(E_r/E_t)$$

$$= \tau_o exp(vK/kT) \ , \qquad\qquad (2.18)$$

where τ_o is the atomic reorganization time or the typical time between independent thermal impulses. It has been estimated to be 10^{-10} sec (Néel, 1955). The anisotropy constant is related to H_c as seen in Equation (2.11). Substituting H_c into Equation (2.18) gives

$$\tau = \tau_o exp(vH_cM_s/2kT) \ . \qquad\qquad (2.19)$$

Therefore M_s has a time-dependent behavior for the various types of magnetization. Equation (2.19) is also important in the principals behind alternating field and thermal demagnetization.

2.3 Types of Magnetization

The two paleomagnetic studies discussed in the thesis involve sedimentary rocks. Sediments have been used in numerous paleomagnetic studies, and in spite of their weak remanent magnetizations they are faithful recorders of the earth's magnetic field. The types of magnetizations which these rocks possess are discussed below.

During deposition of a deep sea sediment the ambient field exerts a torque on the magnetic moment of the ferromagnetic grains, aligning them with the field. Shortly after the deposition, physical processes cause the

grains to translate and rotate, and this alters the original DRM. Sediments deposited in water are often effected by bioturbation in the upper layers. The magnetic minerals are able to move in the pore spaces of the water-filled sediment under the influence of thermal (Brownian) agitation, and can realign themselves statistically with the ambient field. A remanent magnetization locked into the sediment during compaction-induced dewatering is known as a post detrital remanent magnetization (pDRM) and is an accurate record of the earth's field (Irving and Major, 1964; Kent, 1973). It is not effected by the flattening of inclination predicted by Johnson et al. (1948) and King (1955).

The red sediments of the Lower Glarus Nappe complex probably acquired their magnetization with chemical changes of previously deposited minerals. This type of magnetization is known as a chemical remanent magnetization (CRM), and can result from two processes. First, the mineral can form authigenically. The mineral grows from initial zero volume to a critical volume in which it acquires a magnetization as governed by Equation (2.19). Grains that grow above this critical volume retain a stable CRM. For SD hematite this transition occurs when the grains reach a diameter of 300Å (Banerjee, 1971).

In the second process pre-existing magnetic minerals are converted to other magnetic minerals through diagenetic alteration. Examples of these alterations include maghemitization, martitization and dehydration of goethite to hematite. A CRM is often formed in conditions of nonequilibrium, such as weathering or uplift, and can be different from the initial pDRM or diagenetic CRM.

2.4 Magnetic Minerals

The minerals responsible for the magnetization of the Majolica formation and the red beds of the Lower Glarus Nappe complex are part of the $FeO-TiO_2-Fe_2O_3$ ternary system. The properties of the magnetic minerals of this system are summarized in Figure 2.3 and Table 2.2.

The cubic minerals are part of the ulvöspinel (Fe_2TiO_4) - magnetite (Fe_3O_4) solid solution series, referred to as the titanomagnetite series. The Curie temperature, T_c, decreases linearly on a first-order approximation with the mole percent of ulvöspinel, and M_s decreases in a more complex manner (Merrill and McElhinney, 1983).

The rhombohedral minerals of the titanohematite series are not as magnetic as the titanomagnetite series. The end members are hematite

(α-Fe_2O_3) and ilmenite ($FeTiO_3$), and T_c also decreases with increasing ilmenite content. Maghemite (γ-Fe_2O_3) is metastable and reverts to hematite when heated above $300^\circ C$.

The pseudobrookite series are orthorhombic minerals which are paramagnetic above liquid oxygen temperatures. The end members are pseudobrookite (Fe_2TiO_5) and ferropseudobrookite ($FeTi_2O_5$).

There are two other common magnetic minerals which are not part of the ternary system. These are pyrrhotite ($Fe_{1-x}S$) and goethite ($FeOOH$) which degenerates to an oxide mineral between $100^\circ C$ and $300^\circ C$. The magnetic properties of pyrrhotite are discussed in detail in Schwarz and Vaughan (1972).
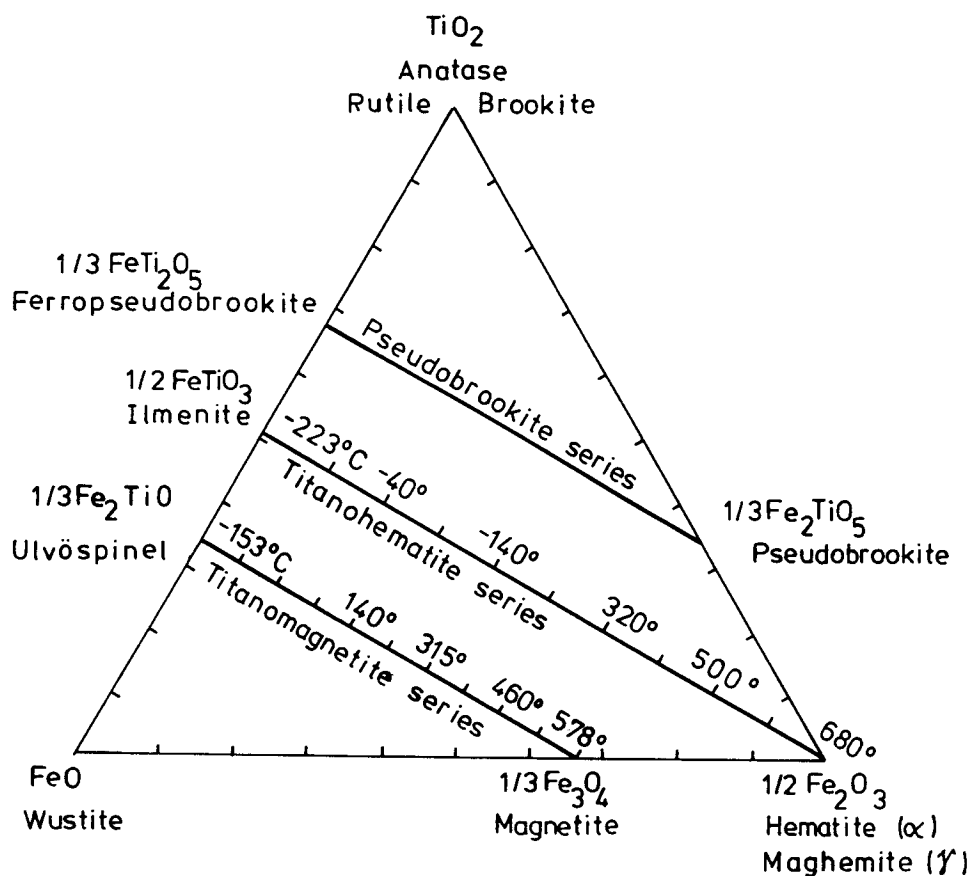
Figure 2.3. FeO-TiO_2-Fe_2O_3 ternary system. Approximate Curie (or Néel) temperatures are given for mole function x (after Merrill and McElhinney, 1983).

Table 2.2. Magnetic Properties of Common Minerals (after Merill and
McElhinney, 1983)

Mineral	Magnetic State	M_s	T_c (°C)
Magnetite Fe_3O_4	Ferrimagnetic	476	580
Ulvöspinel Fe_2TiO_4	Antiferromagnetic		-153
Hematite $\alpha\text{-}Fe_2O_3$ (Hexagonal)	Antiferromagnetic with parasitic ferromagnetism	≈2.2	680[1]
Maghemite $\gamma\text{-}Fe_2O_3$ (Cubic)	Ferrimagnetic	426	≈600
Ilmenite $FeTiO_3$	Antiferromagnetic		-233
Pyrrhotite $Fe_{1-x}S$ (0<x≤0.14)	Antiferromagnetic $0 < x \leq 0.09$ Ferrimagnetic $0.09 < x \leq 0.14$	90	≈320
Goethite FeOOH	Antiferromagnetic with parasitic ferromagnetism	≈2 (?)	≈120

M_s - saturation magentization in 10^{-3} A/m

T_c - Curie or Néel temperature

[1] - Estimates vary from 675°C to 725°C   (Fuller, 1970)

2.5 Anisotropy of Magnetic Susceptibility

If a magnetic field is applied along the x-axis of a prolate ellipsoid (Figure 2.4), the effective field will be reduced because of the influence of the demagnetizing field. The effective field, H_x is defined as

$$H_x = H - N_x M = H - kN_x H_x$$

$$= H/(1 + kN_x) .$$

and the magnetization is

$$M_x = kH_x$$

$$= kH/(1 + kN_x) .$$

Similarly, for a field applied along the y-axis

$$M_y = kH_y$$

$$= kH/(1 + kN_y) . \tag{2.20}$$

The difference between M_x and M_y is due to the different dimensions of the ellipsoid in the x and y directions. This can be expressed as a susceptibility difference since H is constant

$$\delta k_{xy} = k/(1 + kN_x) - k/(1 + kN_y)$$

$$= \frac{k^2(N_y - N_x)}{(1 + kN_y)(1 + kN_y)} . \tag{2.21}$$

The differences, δk_{yz} and δk_{zx} can be calculated similarly.

In an isotropic mineral M parallels the applied field, H. The magnetization along any direction of a selected coordinate system, is determined only by the field component along that direction. In an anisotropic mineral M is not parallel to the applied field in general. Each component of the magnetization must be determined from every component of the field. The magnetization in a weak field is therefore defined as
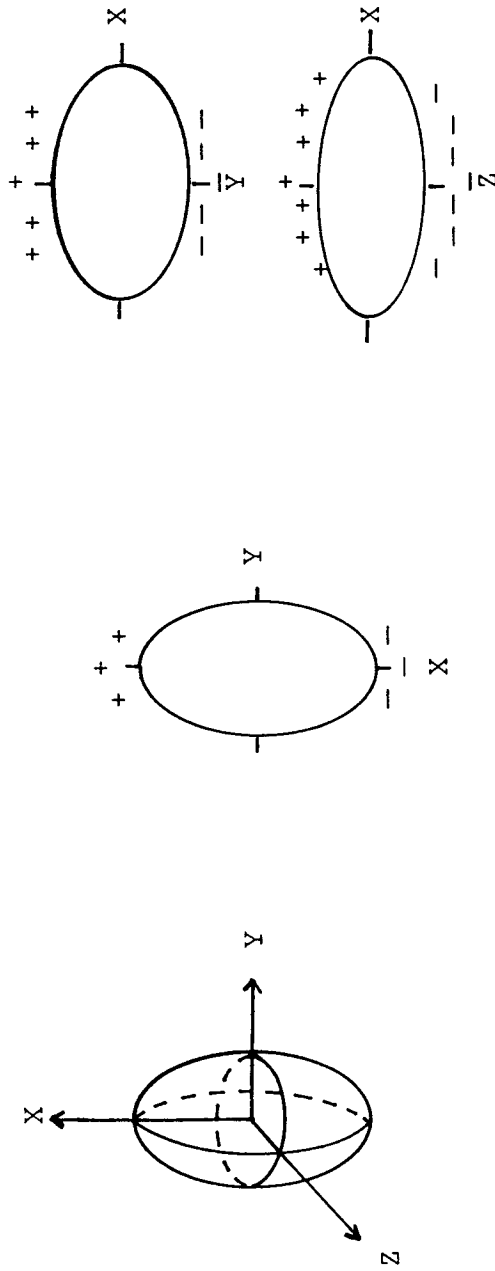
Figure 2.4. A prolate ellipsoid, with the demagnetizing fields along its three axes.

$$M_x = k_{xx}H_x + k_{xy}H_y + k_{xz}H_z$$

$$M_y = k_{yx}H_x + k_{yy}H_y + k_{yz}H_z \qquad (2.22)$$

$$M_z = k_{zx}H_x + k_{zy}H_y + k_{zz}H_z \; .$$

This can be written in tensor notation, with $i,j = x,y,z$, as

$$M_i = k_{ij}H_j \; ,$$

where $k_{ij} = k_{ji}$. The k_{ij} terms represent a tensor of second rank, known as the susceptibility tensor (Hrouda, 1982) . We can further rewrite Equation (2.20) in terms of the directional cosines of the magnetization (n_i) and the field (n_j) relative to the specimen axes so that

$$Mn_i = Hk_{ij}n_j \; . \qquad (2.23)$$

Multiplying both sides of Equation (2.23) by n_i gives

$$k' = M/H = k_{ij}n_in_j \; , \qquad (2.24)$$

where k' is the susceptibility of a specimen in a direction with direction cosines n_1, n_2 and n_3 relative to the specimen axes. This describes the equation of a triaxial susceptibility ellipsoid. The ratios of the principal axes are a measure of their elongations, and are therefore a degree of measure of the anisotropy of the susceptibility.

A description of the measurement of the susceptibility anisotropy on a spinner magnetometer is given in Appendix A.

2.6 Magnetic Anisotropy of Minerals

The ferromagnetic minerals magnetite, hematite and pyrrhotite will have the greatest contribution to the AMS in a rock. The ferromagnesium minerals, such as hornblende, augite and chlorite, are paramagnetic, and calcite is diamagnetic; both of these groups can also contribute to the AMS.

Magnetite is a cubic mineral and is therefore dominated by a shape anisotropy (Section 2.1). Although it has an easy axis of magnetization

along its (111) direction and a hard axis along its (100) direction, any irregularity in the grain shape causes the susceptibility to parallel the long axis of the grain.

Hematite is governed by a magnetocrystalline anisotropy. It is essentially isotropic in its basal plane, but the low field susceptibility is approximately two-orders of magnitude lower along the c-crystallographic axis (Uyeda et al., 1963; Daly, 1967). The basal plane is found to have a triaxial anisotropy in high fields (Porath and Raleigh, 1967).

Pyrrhotite is also governed by magnetocrystalline anisotropy. The low field susceptibility along the c-crystallographic axis is approximately three orders of magnitude lower than in the basal plane. Hexagonal crystals have no variation of susceptibility in their basal planes, but pseudohexagonal crystals are ferrimagnetic and are found to have a variation of susceptibility in the basal plane related to shape (Uyeda et al., 1963).

Experimental studies by Parry (1971) reported that hornblende had k_{max} directions parallel to the c-crystallographic axis. He also looked at single crystals of augite, in which k_{int} paralleled the b-crystallographic axis and k_{max} and k_{min} lie between the a- and c-crystallographic axes. Chlorite is a sheet silicate and is considered to be responsible for the anisotropy in the Borrowdale volcanics (Borradaile et al., 1986) and in Jurassic and late Triassic mudrocks in England (Hounslow, 1985). The k_{min} axes were found to be normal to the tabular habit of the grains and the k_{max} axes were found to generally parallel the long axis of the grains.

The anisotropy of calcite is described in Owens and Bamford (1976) as uniaxial diamagnetic. The anisotropy is prolate about the c-crystallographic axes, in which $k_{max} = -1.38 \times 10^{-5}$ and $k_{int} = k_{min} = -1.24 \times 10^{-5}$.

Chapter 3. METHODOLOGY

3.1 General

Samples for both paleomagnetic and magnetic anisotropy studies were collected in the field with a portable gasoline drill or as blocks and were oriented with a Brunton compass. The magnetization of the rocks sampled was weak enough so as not to effect the compass. Block samples were drilled out later in the laboratory. Cores of 2.5cm diameter were sliced to 2.2cm length to minimize any shape effect of the specimen during measurement of the anisotropy of magnetic susceptibility (Porath et al., 1966).

Bulk susceptibilities were measured for all samples on a Model KLY-1 bulk susceptibility bridge interfaced to a HP-1000 minicomputer. A sensitivity level of 4×10^{-8} (S.I.) is obtained. Thermally demagnetized specimens were measured after each heating step to monitor changes in the magnetic mineralogy.

3.2 Paleomagnetic Evaluation

Natural remanent magnetizations (NRM) of samples used for paleomagnetic evaluation were measured on a cryogenic magnetometer, described by Goree and Fuller (1976). The magnetometer is interfaced with a HP-1000 minicomputer. Three or six replicate measurements were made for each specimen, which overdefines the remanence vector. This can be used as a rejection criterion (Lowrie et al., 1980). The cryogenic system has an instrumental noise level of approximately 3×10^{-6} A/m.

Alternating field (AF) demagnetization was done using a Schonstedt Geophysical Demagnetizer, Model GSD-1 (Roy et al., 1975). A Schonstedt thermal demagnetizer with a rest field of 5nT was used for thermal demagnetization. Specimens were demagnetized using step-wise treatment, in which the demagnetization steps were chosen individually to suit the demagnetization behavior of the specimen.

Secondary and characteristic components of remanent magnetization were generally determined from vector diagrams (Zijderveld, 1967; Dunlop, 1979). Vectors were defined using a two-dimensional least-squares fit for linear segments. Stable end points were used only rarely when a sufficient decrease in the magnetization intensity did not occur during demagnetization, but when the direction remained constant. The use of

stable end points is less satisfactory since it assumes that the characteristic direction is not overprinted by secondary components of magnetization. On a vector diagram it is not uncommonon that a high coercivity or high blocking temperature component remains after demagnetization, such that a linear decay exactly to the origin of the plot does not occur (Figure 3.1a). Although the linear segments isolated between 10 and 30 mT on the vector diagram represent the ChRM direction of the specimen, a high coercivity component of magnetization remains. Examining directional behavior of the magnetization during demagnetization on an equal area plot, a stable end-point is defined between 40 and 80 mT (Figure 3.1b). This end point direction is not the characterisitc direction for the specimen, but represents a hard direction which has not been removed by the A.F. demagnetization.

3.3 Evaluation of the Anisotropy of Magnetic Susceptibility

The anisotropy of magnetic susceptibility was measured on a modified Digico Anisotropy Delineator spinner magnetometer, which measures the low-field susceptiblity in an effective applied field of 0.246mT at 10kHz (Schultz-Krutisch and Heller, 1985). The program used by Digico to calculate the susceptiblity differences has been corrected for the factor of two reported by Hrouda et al. (1983) and Veitch et al. (1983).

A mean susceptibility magnitude ellipsoid for a specific site was calculated using the program AVANI written by Dr. W. Owens and modified by Prof. W. Lowrie. In this program each axis of the AMS ellipsoid for a specimen is normalized and separated into the three components of the reference coordinate system. The individual components are added for all specimens and an average ellipsoid is then refitted. The mean ellipsoid calculated by this procedure is sensitive to single specimens with extreme-shapes (i.e. very oblate or very prolate ellipsoids). These specimens were therefore excluded using the following criterion. Flinn's k-value (Ramsay, 1967) was defined using the intensities of the principal axes of the AMS magnitude ellipsoid:

$$\frac{(k_{max}/k_{int}) - 1}{(k_{int}/k_{min}) - 1} = k_{mag} .$$

Number of
samples: 11

● normal
○ reversed

N

NRM

10

20

30

40
60
80mT
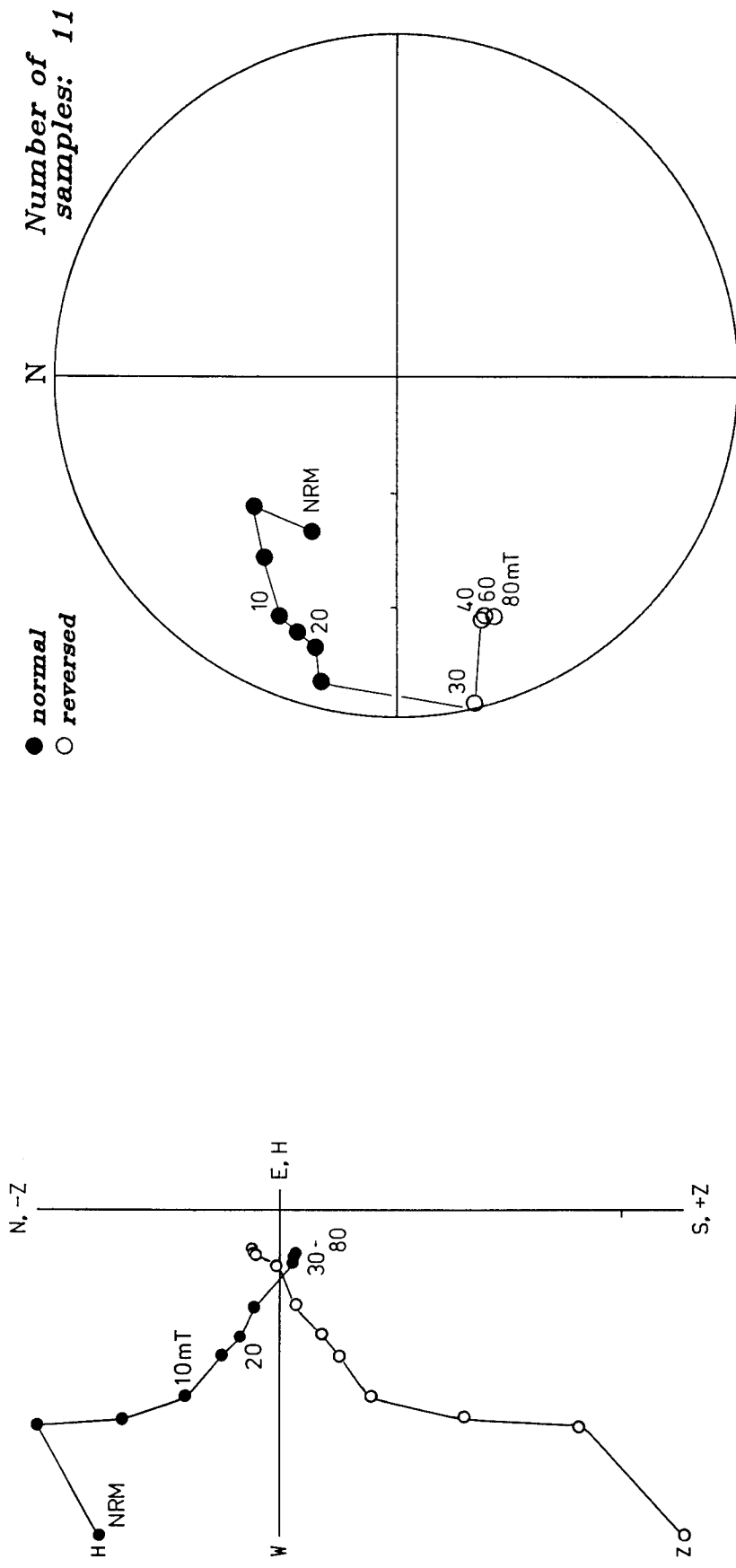
b) IN GEOGRAPHIC COORDINATES

Figure 3.1. Examples of two components of magnetization with overlapping coercivity spectra. a.) Vector decay proceeds passed the origin. b.) Equal area plot showing the demagnetization path and the stable end point. Filled (open) symbols are plotted on the lower (upper) hemisphere.

N, -Z

E, H

S, +Z

NRM

10mT

20

30
80

H

W

Z

$M_o = 1.61 \times 10^{-4}$ A/m

M/M_o

1.0

0.5

0.0

20

40

60

80

B [mT]

a)
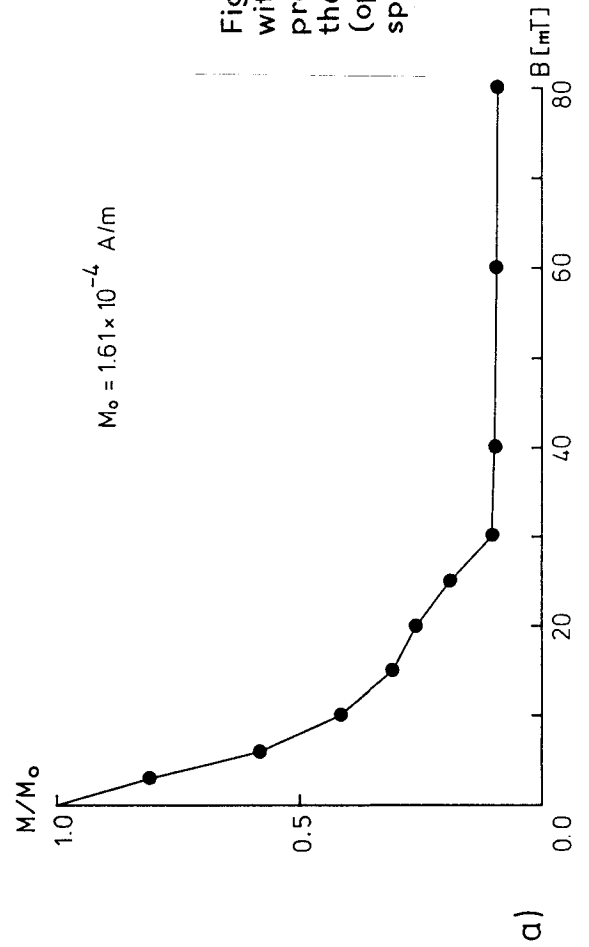
It was found empirically that k_{mag} values for individual specimens, which deviate by more than two standard deviations from a site mean, should be excluded. If two axes are similar in intensity, e.g., $k_{max} \simeq k_{int}$ for an oblate ellipsoid or $k_{int} \simeq k_{min}$ for a prolate ellipsoid, the directions of these individual axes will be indeterminate. They will lie, however, in the plane normal to the minimum axis or maximum axis, respectively.

3.4 Rock Magnetic Evaluation

The acquisition of isothermal remanent magnetization (IRM) was observed in a field up to 1.0T using an electromagnet or 3.5T using an Oxford cryogenic magnet. Acquisition curves, reverse field demagnetization and thermal demagnetization behavior of the IRM were used to help identify magnetic carriers.

A horizontal balance designed and built in the Zürich paleomagnetic laboratory (Lebel, 1985) was used to define the Curie temperature of the magnetic mineral in the Glarus red beds. Whole rock samples were used, with a sample holder containing between 0.15 to 0.20g of powder. Specimens were measured in fields between 0.2 and 0.4T and up to temperatures of $700^{\circ}C$. The heating and cooling rates were generally chosen to be $20^{\circ}C/min$.

3.5 Finite Strain Evaluation

To calculate finite strain, strain markers were measured on three or more non-perpendicular surfaces at a site where magnetic anisotropy samples were taken. Reduction spots were measured in the Permian Verrucano shales and Triassic Quarten shales of the Lower Glarus Nappe complex. Calcitic concretions were measured in the Chelmsford Formation of the Sudbury basin. The orientation of the surface, the length of the long and short axes of the strain marker and the orientation of the long axis of the strain marker relative to the strike of the surface were recorded for each surface at a site.

The finite strain ellipsoids for the Glarus red beds were defined using the program TRISEC (Milton 1980), which has been modified by Dr. O.A. Pfiffner and Prof. W. Lowrie. Using this method the strain ellipsoid can be reconstructed from two-dimensional strain markers on any three sections. Since incompatibilities may exist between the section ellipses due to observational and experimental errors or inhomogeneous strain

fields, an adjustment ellipse is defined and applied to the three sections. These sections are then considered compatible, so that a strain ellipsoid can be determined. Eigenvector analysis of the ellipsoid matrix is used to derive the principal axes of the ellipsoid.

Seite Leer /
Blank leaf

Chapter 4. PALEOMAGNETISM OF THE LOWER CRETACEOUS MAJOLICA FORMATION IN THE UMBRIA-MARCHES REGION, ITALY

4.1 Introduction

The tectonic history of the northern Apennine mountain belt derived from paleomagnetic data has been discussed by several authors over the past ten years (Lowrie and Alvarez, 1974, 1975; Channell and Tarling, 1975; Van den Berg and Wonders, 1976; Van den Berg et al., 1978; Channell et al., 1978; Van der Voo and Channell, 1980). Although these studies adressed the problem of autochthony of the Umbria-Marches region and the relevance of paleomagnetic directions to the Adriatic promontory, no definitive answer was found.

Earliest paleomagnetic studies in the Umbria-Marches region concentrated on the Upper Cretaceous to Lower Tertiary Scaglia formation in the northern Apennines (Lowrie and Alvarez, 1974, 1975). The authors considered the Umbria-Marches region to be autochthonous or para-autochthonous to the Italian peninsula. Their paleomagnetic results indicated that the Italian peninsula had rotated some 45° anticlockwise in the Campanian-Maastrichtian stages of the late Cretaceous, and a further 25° anticlockwise rotation in the middle Eocene, relative to Europe.

A study by Channell and Tarling (1975) of the Cretaceous Majolica and Scaglia formations found similar anticlockwise rotations in the Umbria-Marches stratigraphic sequence. However, they attributed these rotations to the allochthonous nature of the region. They felt that the sequence may have undergone rotation relative to the remainder of the Italian peninsula due to decoupling on the Triassic evaporites.

Van den Berg et al. (1978) sampled several stratigraphic levels in the Upper Cretaceous - Lower Tertiary Scaglia formation in northwestern Umbria. They concluded that the Italian peninsula moved with Africa during the Mesozoic. The African pattern of the apparent polar wander (APW) path for the Umbria-Marches region is rotated, however, $25\text{-}30^\circ$ anticlockwise with respect to the African APW path, which suggests a rotation of this amount in the Tertiary. This interpretation also assumes autochthony for the Umbria-Marches region with respect to the Italian peninsula (Van den Berg and Wonders, 1976).

A later regional study by Channell et al. (1978) of the Scaglia formation continued to maintain the allochthony of the Umbria-Marches sequence. The authors suggested that the Umbrian Apennines underwent oroclinal

bending, indicated by the curvature of the mountain belt and its fold axes from north to south and the gradual change in paleomagnetic declination from north to south. The northern part of the Umbria-Marches region consists of a series of anticlines striking 315° and the mean paleomagnetic declination for the Scaglia formation is 316°. The southern region has fold axes which trend 350° and the mean paleomagnetic declination is 338° (Channell et al., 1978). Magnetostratigraphic studies of the Scaglia formation in Gubbio by Lowrie and Alvarez (1977) showed an increasing trend towards more northerly declinations from the Aptian to the Eocene. Each site of the Channell et al. (1978) study was dated paleontologically to show that their results were not dependent on a bias of stratigraphic sampling level.

A review of paleomagnetism in orogenic belts by Van der Voo and Channell (1980) reexamined the data from Channell et al. (1978). They suggested that oroclinal bending was not the mechanism causing the dependence of paleomagnetic directions on the strike of the fold axes in the Umbrian arc. The authors proposed that the arcuate fold belt formed by differential horizontal transport changing gradually on a décollement surface along the fold belt.

Eldredge et al. (1985) made a more rigorous examination of the Channell et al. (1978) data-set to check for oroclinal bending. This study used a method described in Schwartz and Van der Voo (1983) to determine the relation between fold axes and declinations. It concluded that oroclinal bending had taken place in the Umbrian orogen; the trend of the originally straight belt was closer to the present trend of the northern part of the belt, relative to which the southern part subsequently underwent a clockwise rotation.

However, Eldredge et al. (1985) determined the fold axes strikes and the paleomagnetic declinations in the Umbria-Marches region from a map in the Channell et al. (1978) publication. These directions cannot be considered sufficiently accurate for a tectonic study. First, it should be noted that the fold axes orientations in this map are largely schematic. A recent tectonic map of the central Apennines (C.N.R., 1982) shows that the trends of the fold axes are more complicated than in the schematic map. Eldredge et al. (1985) also selected a single reference declination for the Scaglia formation. Since magnetostratigraphic studies show that the paleomagnetic declinations change progressively from the Aptian through to the Eocene (Channell et al., 1978), a single reference

declination cannot be used for sites whose ages cover this entire time span.

The demagnetization data of Channell et al. (1978) were generally evaluated using methods employed frequently in the early 1970's to define paleomagnetic directions. The ChRM direction at a site was defined by a minimum dispersion criterion at an optimum demagnetization step. This method does not describe a characteristic vector or a stable end-point, and often secondary components of magnetization have not been completely removed (see Figure 3.1). When the Scaglia demagnetization data were reevaluated using vector analysis, many site means were redefined. Only sites which had mean directions with $\alpha_{95} < 15^{\circ}$ were considered suitable for tectonic evaluation (Figure 4.1).

The present study was undertaken as a reevaluation of the paleomagnetism of the Umbria-Marches region, using more stringent laboratory techniques. The investigation was done on the Lower Cretaceous Majolica formation. Unlike the Scaglia formation, the Majolica formation does not show any consistent trends at a site level in the paleomagnetic declination or inclination throughout the stratigraphic column (Lowrie et al., 1980; Lowrie and Channell, 1983; Cirelli et al., 1984; Lowrie and Alvarez, 1984). Therefore the age of the Majolica at a site is not important in comparing declinations within the region.

4.2 Geology of the Umbrian Sequence

The Mesozoic sedimentary sequence of the Umbria-Marches region was deposited on the southern margin of the Tethys ocean. The basinal unit of the northern Apennine mountain chain is the late Triassic Burano formation, which consists of anhydrites, marls, dolomites and dolomitic limestones. Although the Burano formation is found outcropping only in Tuscany, it is known in the Umbria-Marches region from the Perugia-2 well (Ghelardoni, 1962). A period of uniform subsidence in the Jurassic led to fault-bounded basins separated by topographic highs, such that local differences in facies and thickness occurred (D'Argenio and Alvarez, 1980). There are three types of stratigraphic sequences found in the region: complete sequences, characteristic of basins; condensed sequences, characterisitc of fault-bounded topographic highs; and composite sequences (Colacicchi et al., 1970; Centamore et al. 1971; Koopman, 1983). The basinal sequences remain uniform in their stratigraphy throughout the northern Apennines. The topographic differences become less extreme
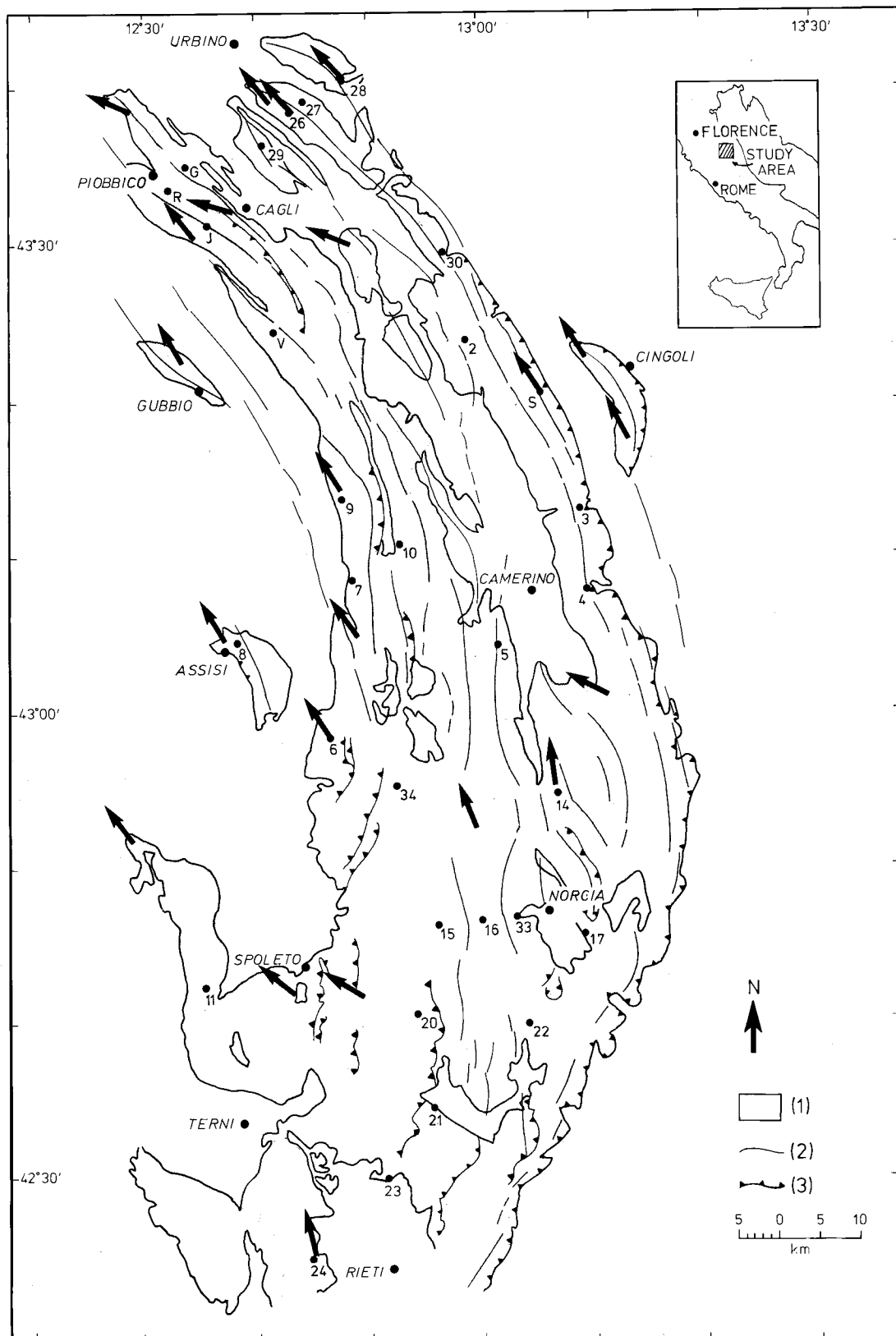
Figure 4.1. A schematic tectonic map of the study area. (1) Lower Jurassic to mid-Cretaceous Calcareous Supergroup; (2) anticlinal fold axes; (3) thrust faults. Arrows show paleodeclinations of site means for the Scaglia Rossa Formation and circles indicate the Majolica Formation sites.

by the late Jurassic with the start of deposition of the Majolica formation. The upper Majolica condensed and complete sequences become laterally continuous stratigraphically (Micarelli et al., 1977), indicating the inactivity of structural boundary faults in the early Cretaceous. Intercalated limestone turbidites and debris sheets are often found in the eastern and southeastern part of the Umbria-Marches region (Alvarez et al., 1985).

The Majolica limestone is a white- to grey-colored, well-bedded limestone with frequent interbedded grey- to black-colored chert beds or nodules. Its lower contact is gradational with the Tithonian Calcare diaspirini limestone, and its upper contact is gradational with the late Aptian Fucoid marls. The Majolica reaches thicknesses of 400 to 500 meters in the basinal sequences, but may be only 100 meters thick in the condensed-sequences (Micarelli et al., 1977). Slumping is found in the basinal sequences.

The general structure of the northern Apennine region is that of an arcuate mountain chain convex to the E-NE (Figure 4.1). The northwestern part of the chain consists of large, box-like fold structures trending NW-SE and facing northeast. Due to their box-like shape, it is difficult to define a single fold axis (Lavecchia, 1981). Folds plunge suddenly at either end with plunges of approximately 10°. The southern part of the fold belt consists of N-S anticlines which become spatially closer than in the north. These large anticlines are complex in their structure with reverse and thrust faults cutting their limbs (Giannini and Lazzarotta, 1975; C.N.R., 1982). Some folds in the southern region still trend NW-SE.

Tectonic deformation developed in the late Oligocene and continued through the Miocene and at least into the Pliocene (Reutter and Groscurth, 1978). The characteristic fold geometry suggests that the deformation is limited to the sedimentary cover (Giannini and Lazzarotta, 1975; Coli, 1981; Lavecchia, 1986, 1981; and Koopman, 1983). The large-scale thrust motion during the Tertiary often used preexisting Jurassic normal fault planes as ramps, which trend NW-SE or NNE-SSW (Koopman, 1983).

4.3 Sampling and Results

Approximately 800 specimens were collected at thirty-four sites for this paleomagnetic study throughout the Umbria- Marches region (Figure 4.1). Sites were not taken where the fold axes die out and the plunge can be appreciable, therefore corrections for plunging fold axes were not neces-

sary. A minimum of sixteen samples were drilled at each site using a portable gasoline drill. Five sites were block-sampled and later drilled out in the laboratory.

NRM intensities for the Majolica formation were weak, ranging from 3×10^{-3} to 3×10^{-6} A/m, but stable and repeatable. Thermal demagnetization was performed on at least two specimens from each site. Twenty-nine sites had the majority of their specimens demagnetized thermally, revealing a distributed blocking temperature spectrum. A low temperature component of spurious direction was removed by $300^{\circ}C$ and the characteristic remanent magnetization (ChRM) was defined between $300^{\circ}C$ to $500^{\circ}C$ (Figure 4.2).

AF demagnetization was also applied to at least two specimens from each site. Median destructive fields (MDF) were between 5 and 20mT for the majority of the specimens, although some MDF's reached 80mT. Ninety-five percent of the intensity was removed by fields of 20 to 80mT. Both AF and thermal methods isolated similar ChRM vectors for a site (Figure 4.3). Demagnetization vectors decay close to the origin, but not always directly to the origin. This indicates that a hard coercivity or high temperature component still remains, but accounts for less than five percent of the NRM intensity.

IRM acquisition reveals both a low coercivity and high coercivity component (Figure 4.4). The low coercivity component, shown by a kink in the IRM curve at 0.12T, is probably due to magnetite with a small amount of titanium impurity. The presence of magnetite is also indicated in thermal and AF demagnetization. The higher coercivity component could be resulting from hematite or goethite. Hematite is the more likely magnetic carrier since the curve appears to approach saturation by 3.5T. If goethite were present, the IRM would continue to increase in intensity even at these high fields (Lowrie and Heller, 1982).

Specimens given a 3.5T IRM along their vertical axis later had a 0.1T field applied along their X-axis. Thermal demagnetization of the saturation IRM shows that the 0.1T component does not disappear until the specimen has been heated to $580^{\circ}C$ (Figure 4.5a-c). This lower coercivity component is probably carried by a magnetite fraction. The 3.5T component is probably carried by hematite, since it exists until $680^{\circ}C$.

Monitoring the change of bulk susceptibility with heating shows that all the specimens are initially diamagnetic; between $450^{\circ}C$ and $500^{\circ}C$ the susceptibility becomes positive, indicating ferromagnetic material is being created in the heating process (Figure 4.5c). An initial decrease in the
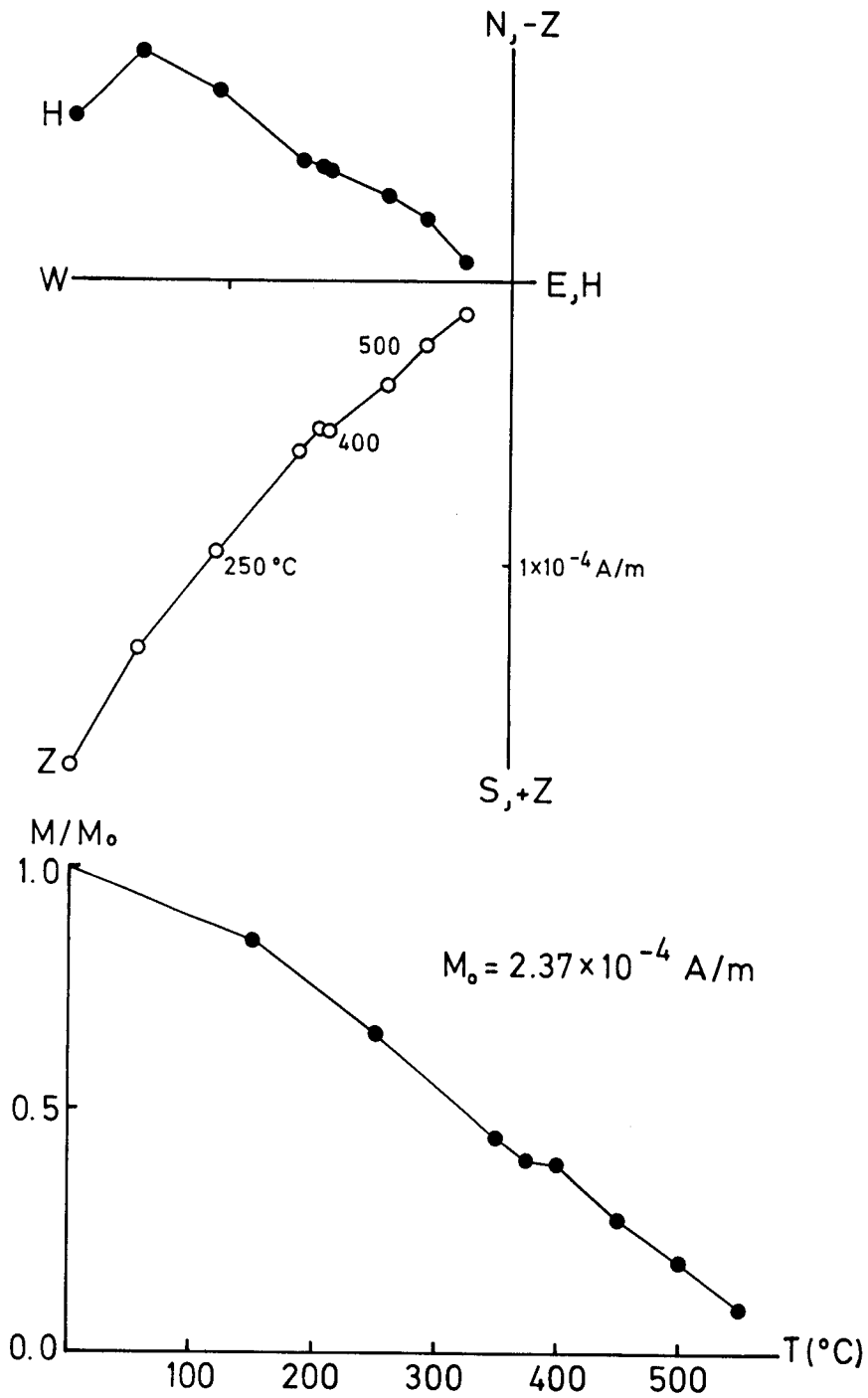
Figure 4.2. Representative vector diagram of a thermally demagnetized specimen which possesses a stable ChRM direction. Closed circles are used for the horizontal projection, open for the vertical projection in this and subsequent figures.
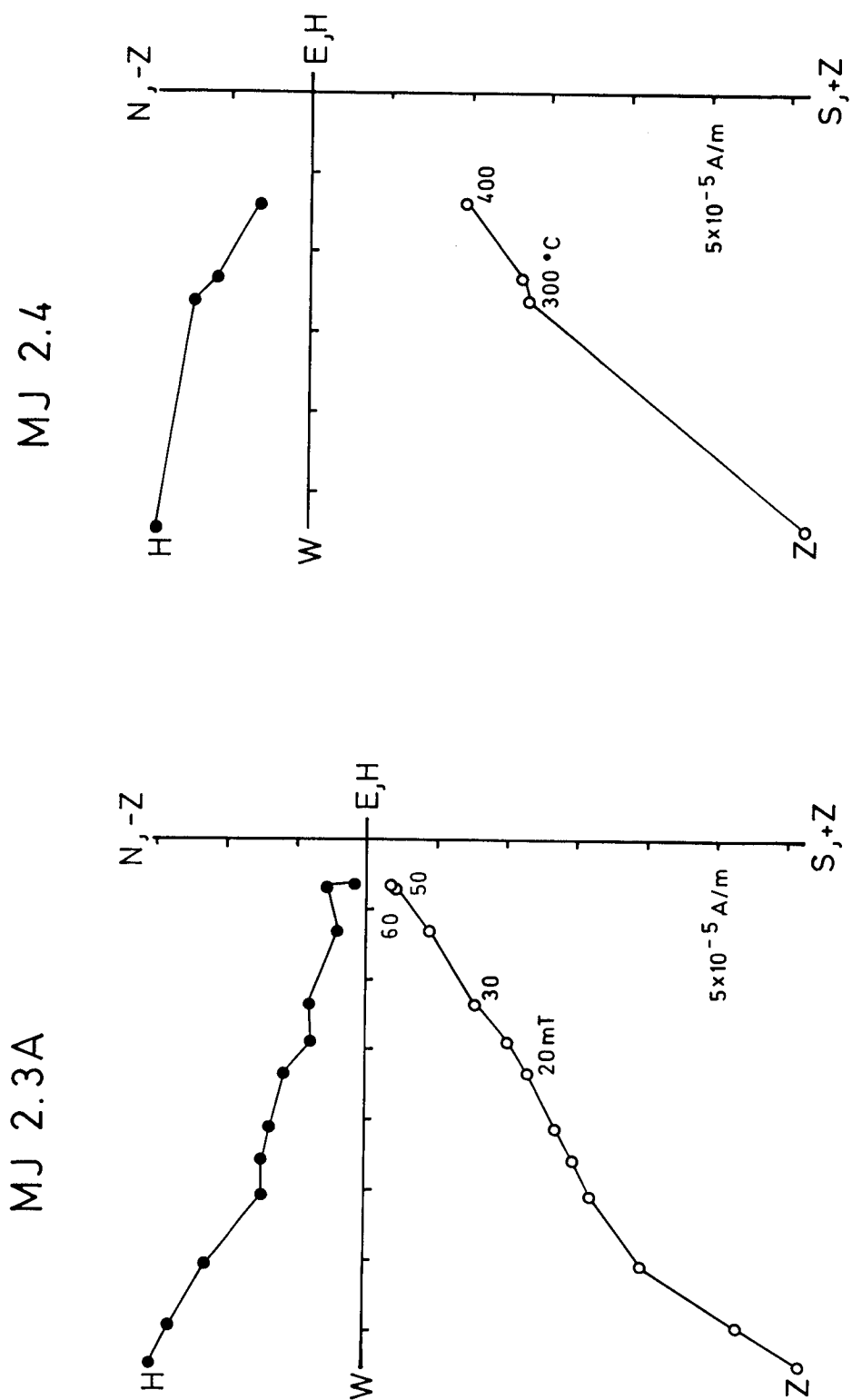
Figure 4.3. Vector diagrams show that similar vector components are defined with AF and thermal demagnetization.
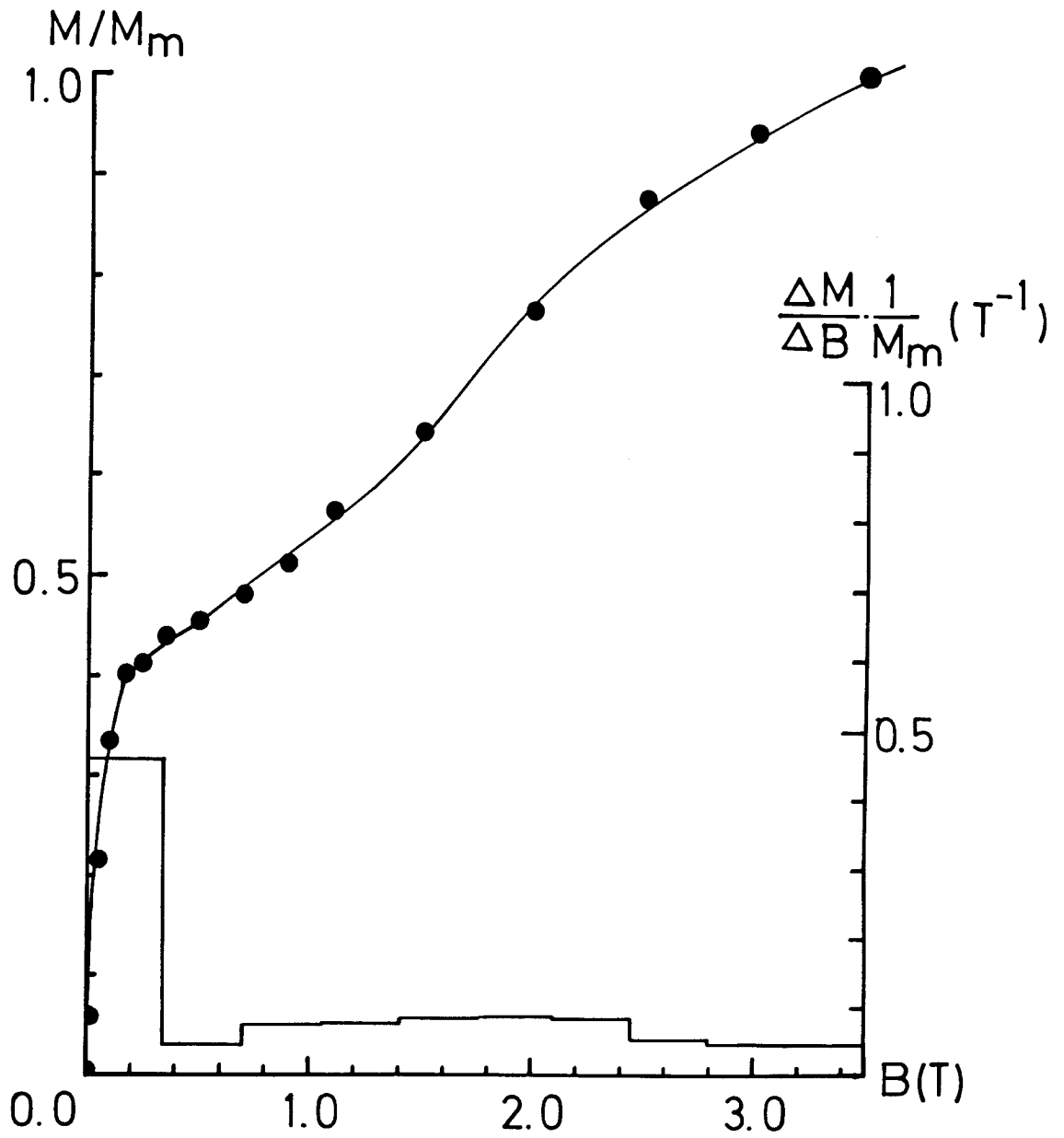
Figure 4.4. IRM acquisition curve for a representative sample of the Majolica formation.

susceptibility during the first heating step to 100°C may indicate a minor presence of goethite (Lowrie and Heller, 1982).

Figure 4.6 shows the ChRM directions defined for each site. Eight sites were discarded since there was a large within-site scatter of their directions ($\alpha_{95} > 15^\circ$) (Table 4.1). Newly defined site-mean directions for six magnetostratigraphic studies are included in Figure 4.6 and Table 4.1. The ChRM directions show a statistically significant improvement upon applying a simple tectonic tilt correction. The statistical significance follows from applying the F-test to the Fisher presision parameters (McElhinney, 1973); the F-ratio is 3.27 which is larger than the critical value of F for (60,60) degrees of freedom. However, it should be noted that the distribution of the site directions is not azimuthally uniform. Therefore strictly speaking Fisher statistics should not be applied to the data.

4.4 Discussion

Magnetostratigraphic studies of the Majolica formation by Lowrie and Alvarez (1984, Fig. 4) have shown that there are no significant trends of the declination or inclination at the 95% confidence level. The azimuths of the magnetic directions in magnetostratigraphic sections and the regional study are smeared. To test whether the declination dispersion in the magnetostratigraphic sections was comparable to that seen in our regional site means, the standard deviations of the declination distributions were computed.

Curray (1956) has discussed statistics of circular distributions. The preferred orientation of a $0-360^\circ$ distribution is equated with the vector mean, calculated in the usual manner by summing the components of the individual vectors. The mean of a $0-180^\circ$ distribution is found by doubling the angles and again finding the mean from the vector sum. The magnitude of the vector sum is a measure of the data dispersion, and gives a good correlation with the standard deviation about the vector direction.

Four sections at Gorgo a Cerbara (G), Bosso(J), Presale (R) and Frontale (S), were divided into subsites of twelve specimens, representing approximately eight meters of section. The standard deviations of the subsite declinations and inclinations are shown in Table 4.2. The difference between the standard deviations of the declination and inclination is not statistically significant at the 95% confidence level for sections J, R and S, and is only marginally significant for section G.
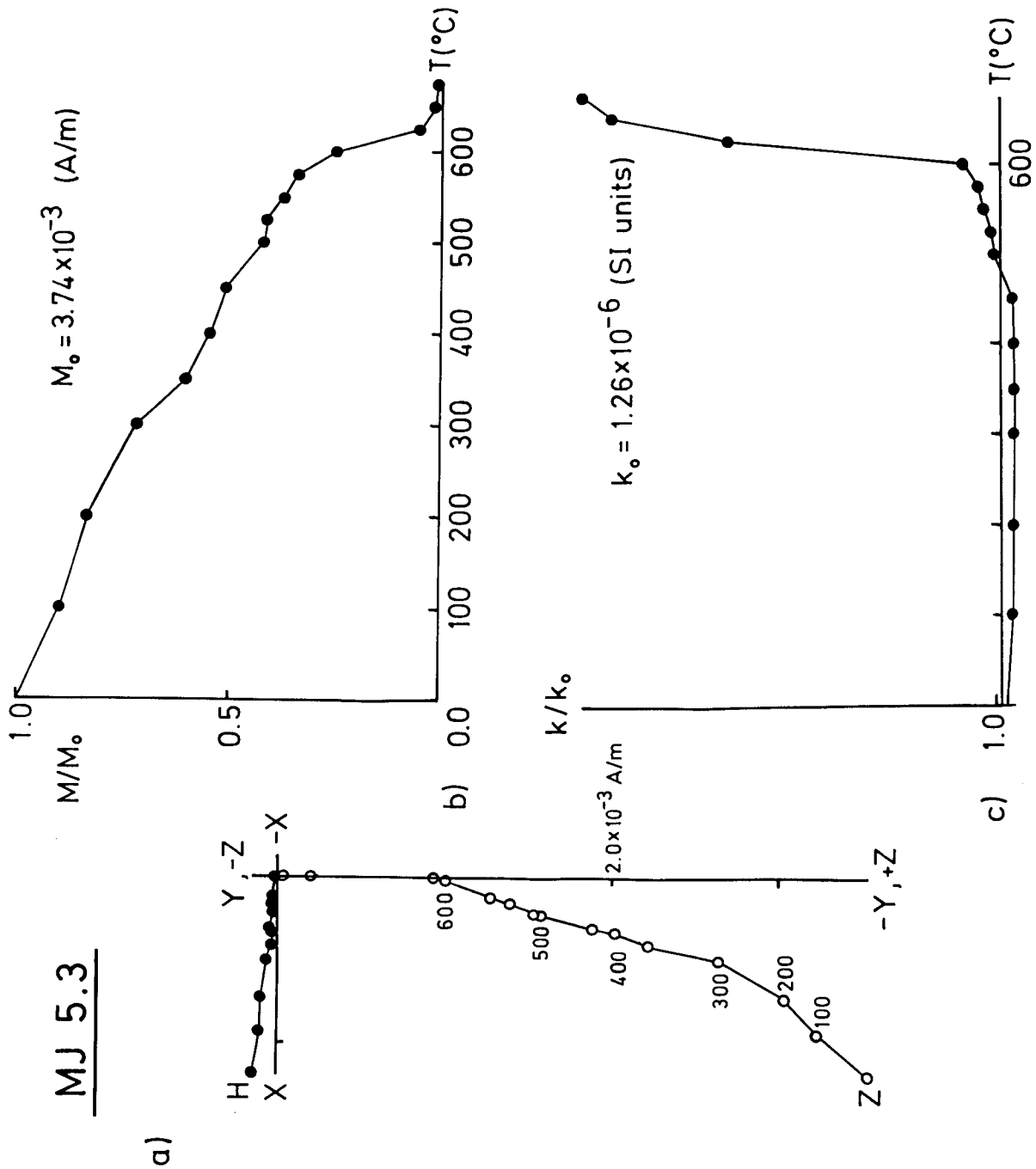
Figure 4.5.   a) Vector diagram which shows the thermal demagnetization behavior of the saturation IRM; b) normalized intensity plot which shows the change of magnetic intensity with thermal demagnetization; and c) change of the bulk susceptibility with thermal demagnetization.

BEFORE BEDDING CORRECTION
k = 8.27

AFTER BEDDING CORRECTION
k = 27.0
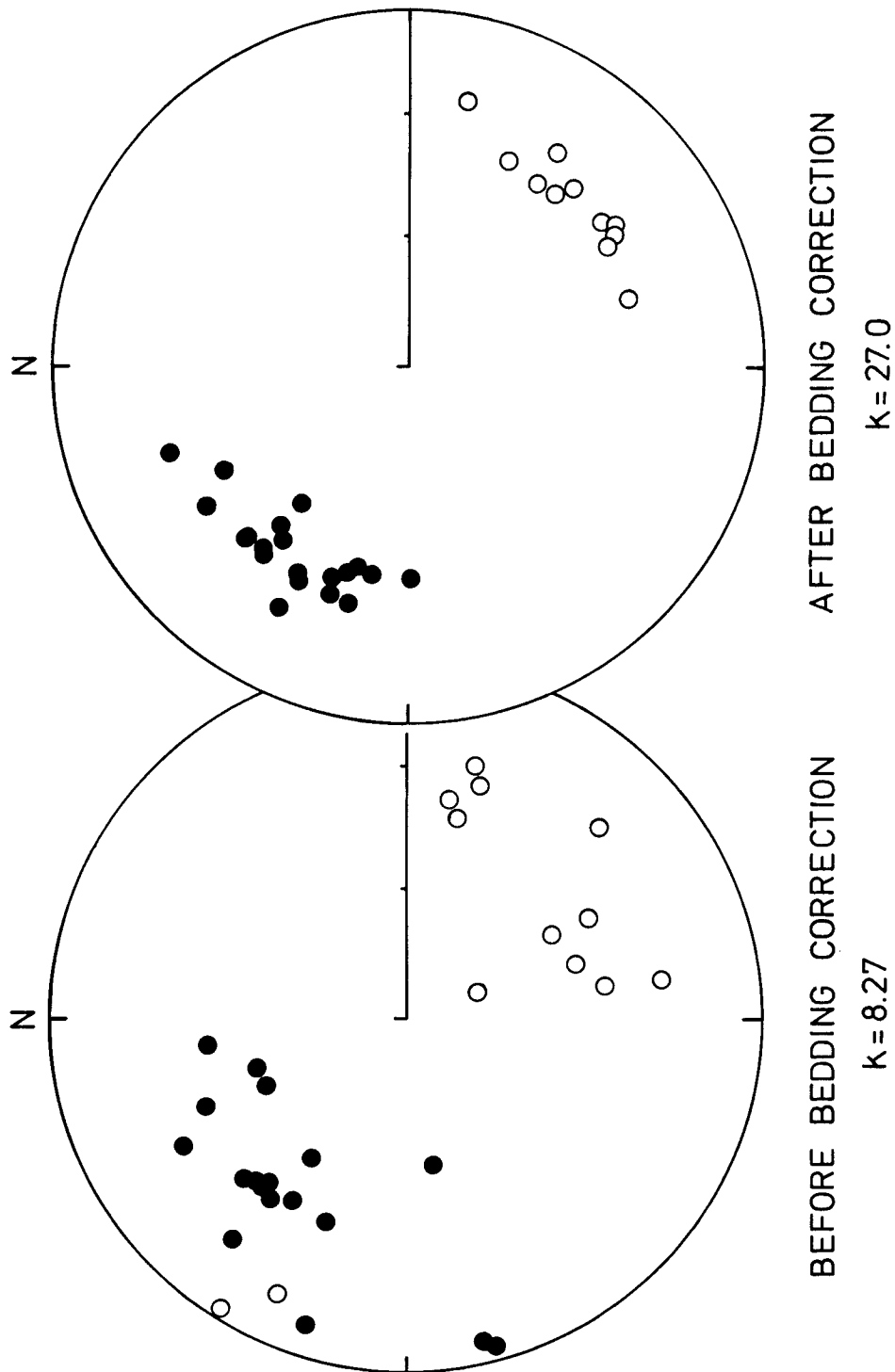
Figure 4.6. Equal area plot of ChRM directions for individual site means before and after tectonic tilt correction. Closed (open) symbols are plotted on the lower (upper) hemisphere for for this and subsequent figures.

Table 4.1 Paleomagnetic site means of the Majolica formation. Columns give the site number, strike of the fold axis (s) where it could be defined, number of specimens (n), declination (D) and inclination (I) of site means, k and circle of 95% confidence (α_{95}). Starred sites (*) were excluded from the calculation of the regional mean because they are poorly defined.

Site	$s(^{\circ})$	n	$D(^{\circ})$	$I(^{\circ})$	k	$\alpha_{95}(^{\circ})$
MJ2	338	14	290.2	37.8	47.4	5.8
MJ3	344	15	314.0	35.0	35.7	6.5
MJ4	342	11	325.7	32.2	48.3	6.6
MJ5	359	13	308.1	50.3	47.9	6.1
MJ6	316	14	142.3	-32.7	63.8	5.0
MJ7	358	15	286.8	40.5	84.1	4.2
MJ8	335	14	129.4	-36.5	51.7	5.6
MJ9	349	14	131.8	-32.5	37.9	6.5
MJ10	350	16	298.3	35.1	51.4	5.2
MJ11	-	15	146.4	-32.0	59.4	5.0
MJ12 *	341	5	318.2	37.0	6.8	31.6
MJ14	340	6	337.4	36.3	45.2	10.1
MJ15	012	16	314.0	34.4	39.6	5.9
MJ16	337	10	144.4	-30.3	67.4	5.9
MJ17	-	14	123.9	-27.5	31.6	7.2
MJ18 *	013	4	45.5	51.2	9.4	31.7
MJ20	320	16	331.1	40.9	50.3	5.3
MJ21 *	-	4	130.9	-27.3	13.4	26.1
MJ22	-	13	309.2	42.9	58.9	5.4
MJ23	-	7	280.2	41.2	49.2	8.7
MJ24	-	13	307.9	34.2	61.5	5.3
MJ26	308	8	309.2	35.5	18.6	13.2
MJ27	300	10	124.2	-37.0	32.1	8.7
MJ28	315	9	101.8	-24.3	40.0	8.2
MJ29	315	11	306.0	40.2	56.7	6.1
MJ30	326	13	114.9	-35.8	55.3	5.6
MJ32	321	10	148.1	-34.9	40.4	7.3
MJ33	337	5	298.4	25.0	56.1	10.3
MJ34	-	10	340.4	29.6	62.7	6.2
R	304	21	284.4	42.0	35.6	5.4
S	335	27	297.3	33.5	104.3	2.7
V	314	10	289.1	33.7	57.6	6.4
G	313	25	269.3	41.1	56.3	3.9
J	305	18	284.3	32.7	59.9	4.5
MEAN		31	306.4	36.7	27.0	5.1

The standard deviations of the declinations and inclinations of the Majolica formation have a statistically significant difference from each other. The standard deviation of inclinations is comparable to that seen in the stratigraphic sections, but the standard deviation of declinations is three times as large (Table 4.2). This suggests that the between-site declination scatter in the Majolica regional study must be due to uncompensated tectonic effects.

Table 4.2 Standard deviations of declination (D) and inclination (I). Columns give magnetostratigraphic section Gorgo a Cerbara (G), Bosso (J), Presale (R) and Frontale (S), mean direction of the Majolica Formation (MJ), mean direction for sites north of Assisi-Cingoli (MJn) and sites south of Assisi-Cingoli (MJs).

	G	J	R	S	MJ	MJn	MJs
Stan. dev. D($^{\circ}$)	10.2	5.1	6.1	3.1	18.2	12.2	16.0
Stan. dev. I($^{\circ}$)	5.7	5.4	5.1	5.3	5.4	4.4	6.3

Channell et al. (1978), Van der Voo and Channell (1980) and Eldredge et al. (1985) suggested that the ChRM directions of the Scaglia formation were related to the fold axes. Could the nonuniformity of the tectonically corrected ChRM directions of the Majolica formation also be due to their dependence on local fold axis orientation?

One method to examine the relationship between site mean directions and the local fold axes is to rotate all the fold axes strikes to correspond to a strike direction for the entire Umbria-Marches region. The same amount of rotation applied to the fold axis at each site in order to align the strike of the local axis with the reference strike is also applied to the ChRM declination. If the fold belt was bent after primary folding, then the grouping of ChRM directions should improve after rotating the fold axes with their accompanying remanent declinations. Figure 4.7 shows the distribution of directions after compensating for the deviation of the local fold axes from an arbitrary regional trend of 321°. This rotation was applied only at sites where a regional fold axis could be defined. The ChRM directions for the 25 sites show an increase in dispersion after unbending of the fold belt (D=294°, I=37°, k=20.4, and α_{95}=6.6°). A F-test of the Fisher precision parameters shows that this new mean direction is not significantly improved at the 95% confidence level. The

N

k = 20.4
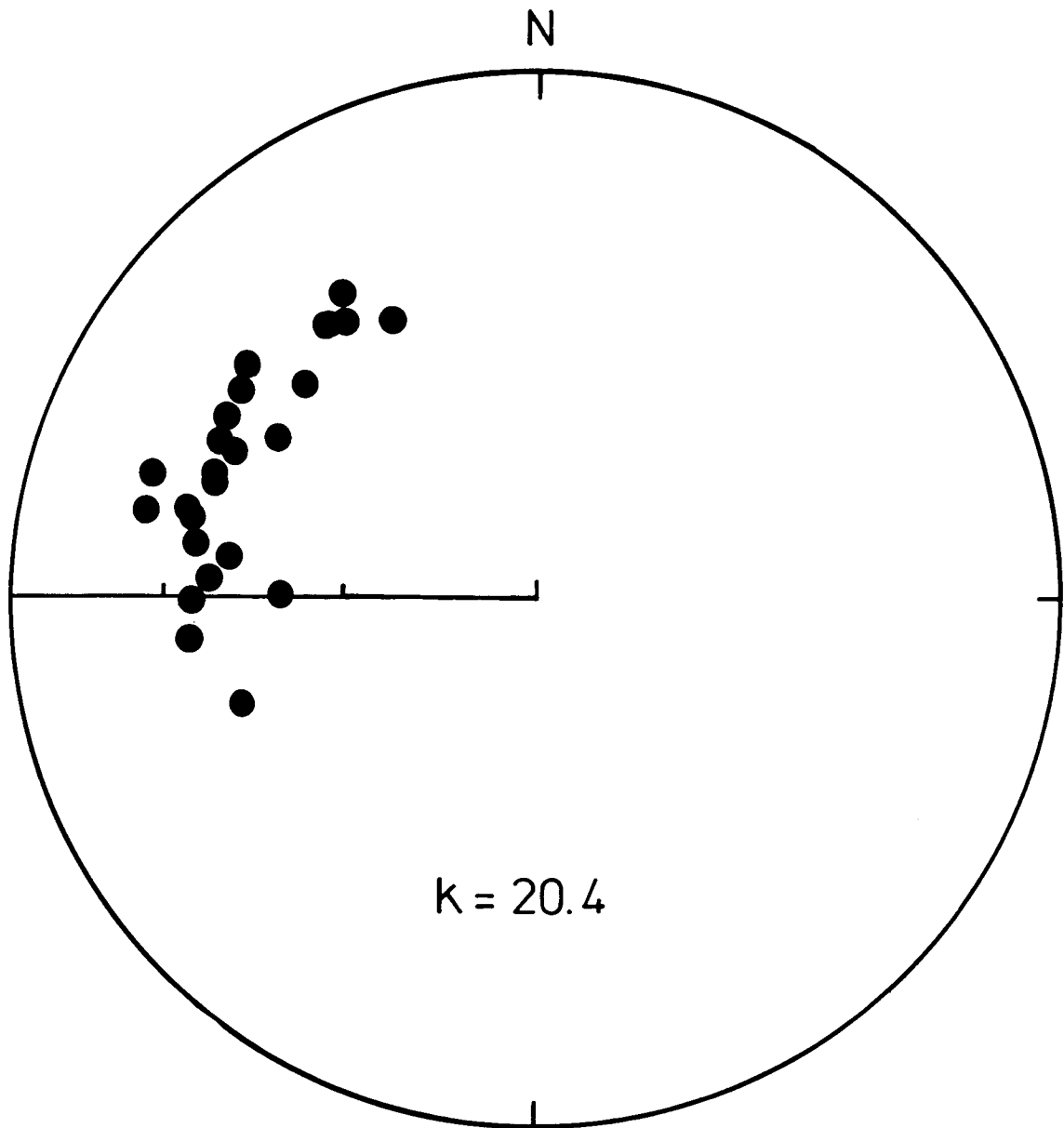
Umbrian Oroclinal Test

Figure 4.7. Equal area plot of ChRM directions of site means rotated to account for variation of the local fold axes from an arbitrary regional trend of 321°.

F-ratio of 1.32 is less than the critical value 1.57 for (48,60) degrees of freedom. The result does suggest that there were no systematic rotations about vertical axes.

The relative variations of paleomagnetic declinations and fold axes strikes about their respective means provide another method of testing their dependence (Lowrie and Hirt, 1986; Eldredge et al., 1985; Schwartz and Van der Voo, 1983). At any site the deviation of declination from its expected value shoud equal the deviation of the local fold axes from the regional trend. Plotting the declination deviations against the corresponding deviations of the local fold axis strike should yield a line of positive unit slope if the belt was bent after the ChRM directions were acquired. Figure 4.8a shows the declination deviations for each site plotted against deviations of the local fold axes from an arbitrary regional strike. The reference declination for the Majolica formation is the regional site mean for this study, $306°$. The reference strike of the fold axes was $330°$.

The slope of the regression line in Figure 4.8a is not significantly different from a zero slope at the 95% confidence level. A t-test of the regression slope shows that the t-statistic for the slope (1.29) is less than the critical t-statistic (2.07). Assuming that the folds are cylindrical on first approximation, we have also tried correlating the declination variation with that of the bedding strikes (Figure 4.8b), which is equivalent to comparing fold axes on a very local scale. This also leads to a slope which is not statistically different from a zero slope. For this case the t-statisitic 0.13 is much less than the critical t-value 2.06.

Although the ChRM directions are not simply related to the fold axes, regional differences can be found in the data. Sites north of a line from Assissi to Cingoli tend to have declinations more westerly than the mean declination of $306°$ (Figure 4.9). Sites south of this line have declinations which are more northerly. The separate means are D=$295°$, I=$37°$ (k=57, α_{95}=$5°$, N=15) for the northern group and D=$318°$, I=$36°$ (k=32, α_{95}=$7°$, N=16) for the southern group. The northern site directions are only marginally uniformly distributed about their means and the southern sites are not azimuthally uniform. Again both groups have a scatter of the declinations which exceeds that seen in the magnetostratigraphic sections (Table 4.2). This similar between-site scatter in both group site means suggests that the cause of this directional scatter is similar in both the northern and southern regions.
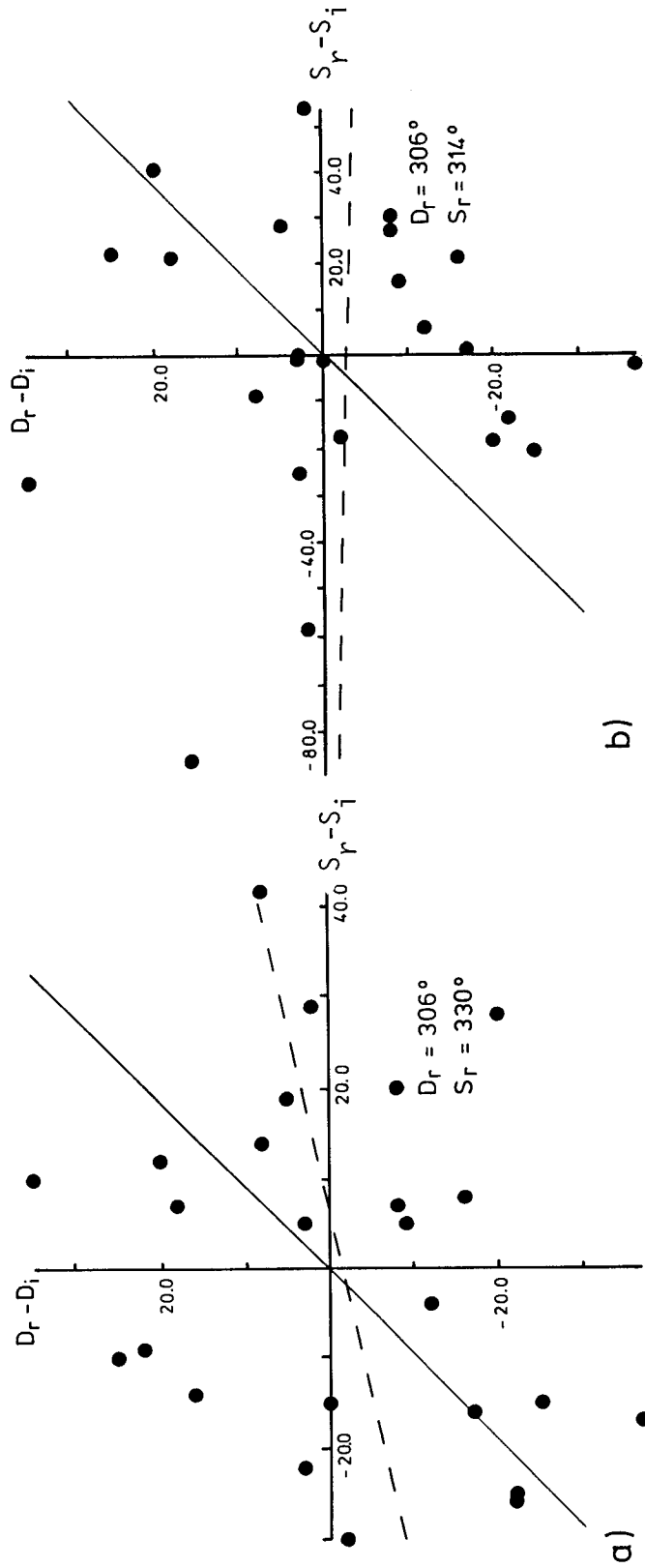
Figure 4.8.   Diagrams showing declination deviations relative to a) fold axis strike deviations and b) bedding deviations for the Umbria-Marches region. D_r is the reference declination and D_i is the observed declination at a site; S_r is the reference direction of the fold axes (a) or bedding strikes (b) for the region and S_i is the fold axis direction (a) or bedding strike direction (b) at a site. The solid line with unit slope represents oroclinal bending of an originally straight fold belt. The dashed line is a best fit line calculated by linear regression analysis.
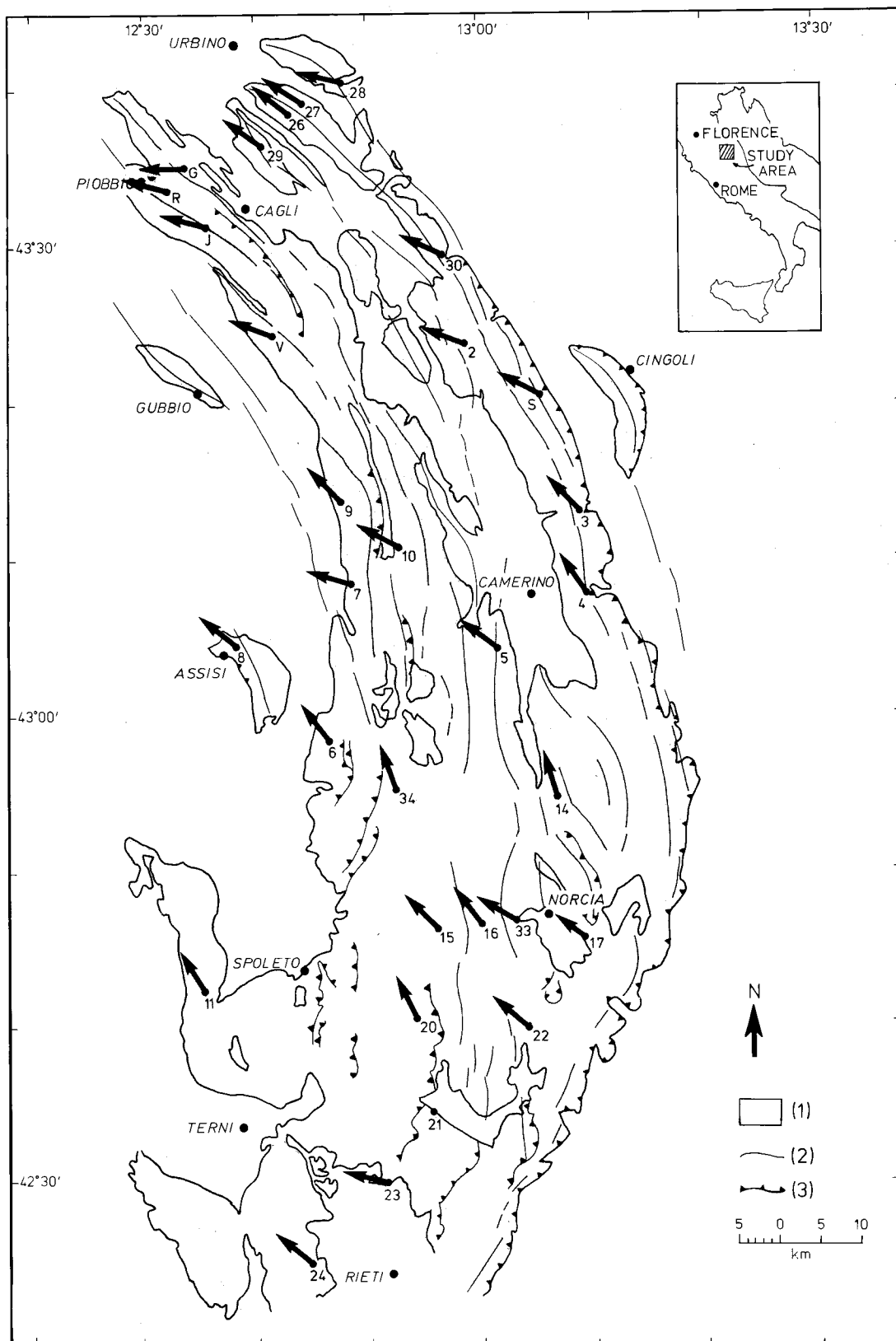
Figure 4.9. Paleodeclinations of the site means of the Majolica Formation. Symbols are the same as in Figure 4.1.

The N-S difference in the data may be due to the tectonic differences in these areas. Thrust faults cut through to the surface in the southern part of the fold belt, and the folds are also cut by normal faults. The folding and faulting are very complicated. In the northern part blind thrusting may occur (Koopman, 1983; Roeder, D., pers. comm.), and normal faulting is not as predominant. The scatter of the paleomagnetic declinations may result from these local tectonic variations, which can not be accounted for without more detailed structural analysis.

A possible explanation for the curvature of the mountain belt is that it results from ramp-thrust tectonics. Geologic field evidence indicates that the thrust direction throughout the Umbria-Marches region is towards the northeast (Koopman, 1983). Koopman (1983) has defined two trends for the underlying ramps, NW-SE and NNE-SSW, which reflect the Jurassic normal fault system. In Figure 4.10a an allochthonous sheet has a thrust direction towards the NE. When this sheet moves over a ramp trending NW-SE the resulting fold has a trend of NW-SE, since the thrust direction is normal to the trend of the ramp. If the trend of the ramp is oblique to the direction of overthrust, then there is a dextral strike-slip component of displacement (Figure 4.10b). The resulting fold is no longer related to the direction of overthrusting. The curvature of the belt results from the interference between overthrusting perpendicular and oblique to the underlying ramps and their resulting folds (Koopman, 1983).

The role of the Umbria-Marches region in interpreting the regional tectonic history has been diversely interpreted (Channell et al., 1979; Lowrie, 1980, 1986; Van den Berg and Zijderveld, 1982; Márton and Márton, 1983). Independent seismic and geologic field evidence indicate that the mountain belt is allochthonous (Lavecchia, 1986; Lavecchia et al., 1984; Roeder, D., pers. comm., 1984). Therefore paleomagnetic evidence from the northern Apennines should be excluded from any plate reconstructions. The Majolica site mean direction from the present study agrees well with other Lower Cretaceous data from the Adriatic promontory (Figure 4.11, Table 4.3). The studies which included only data from northwestern Umbria (Cirelli et al., 1984; Van den Berg et al., 1978) do not agree as well with the data from Gargano or the Istrian peninsula. This is due to the regional differences of declination seen in the Umbrian fold belt. The limited distribution of sites used in these studies implies that the data are not representative of the Umbria-Marches region.
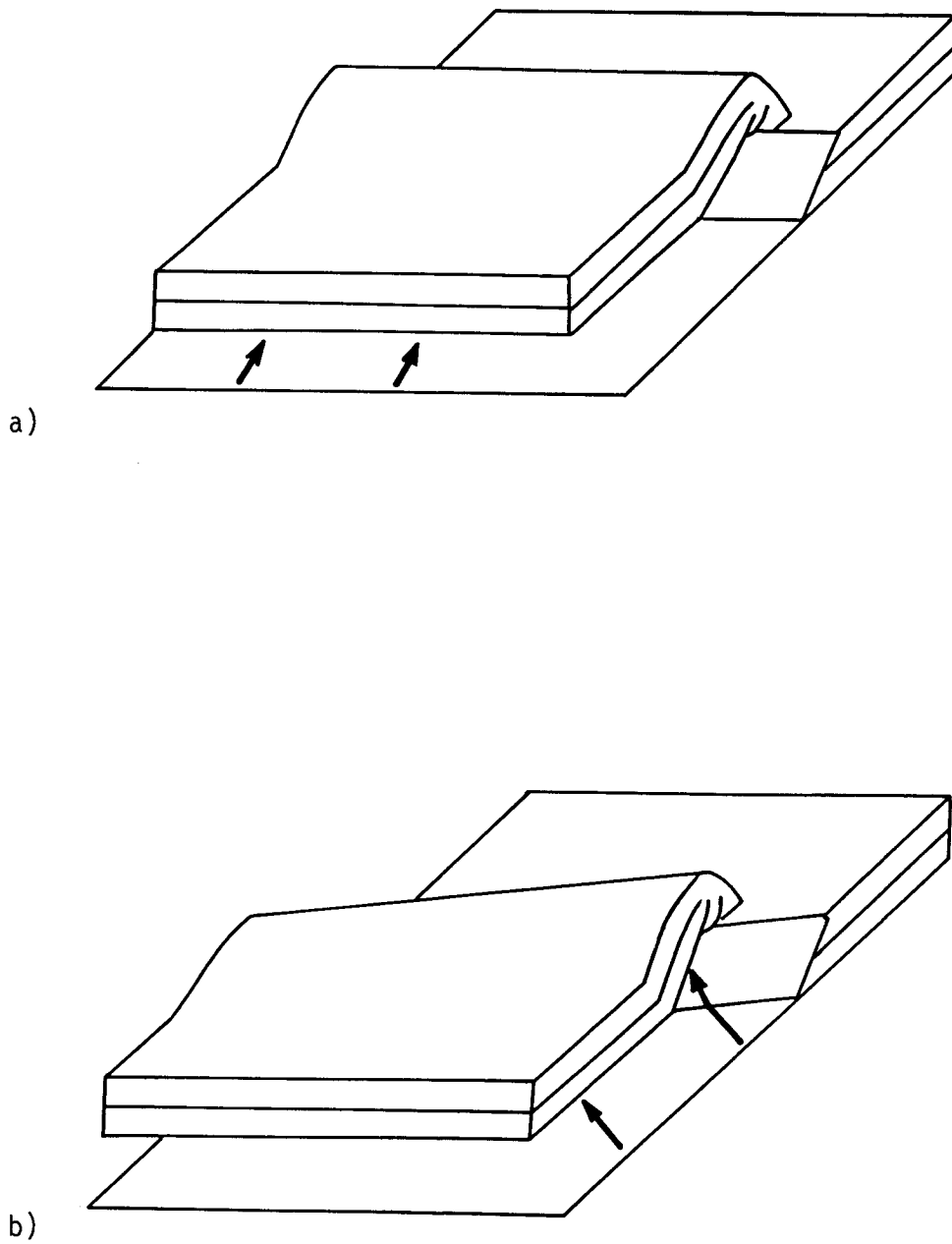
Figure 4.10. Model for ramp-thrust directional relationship and the re-
sulting fold orientation. The trend of the fold axis is related to the
underlying trend of the ramp. a) Thrust direction is normal to the trend
of the ramp; b) Thrust direction is oblique to the trend of the ramp.

N

UMBRIA MARCHES
● Present study-entire region
⊗ Van den Berg et al. (1978) ⎤ northern
⊕ Cirilli et al. (1984) ⎦ region

GARGANO
■ Horner (unpublished data)
⊠ Van den Berg (1983)

ISTRIA
▲ Márton and Veljovic (1983)
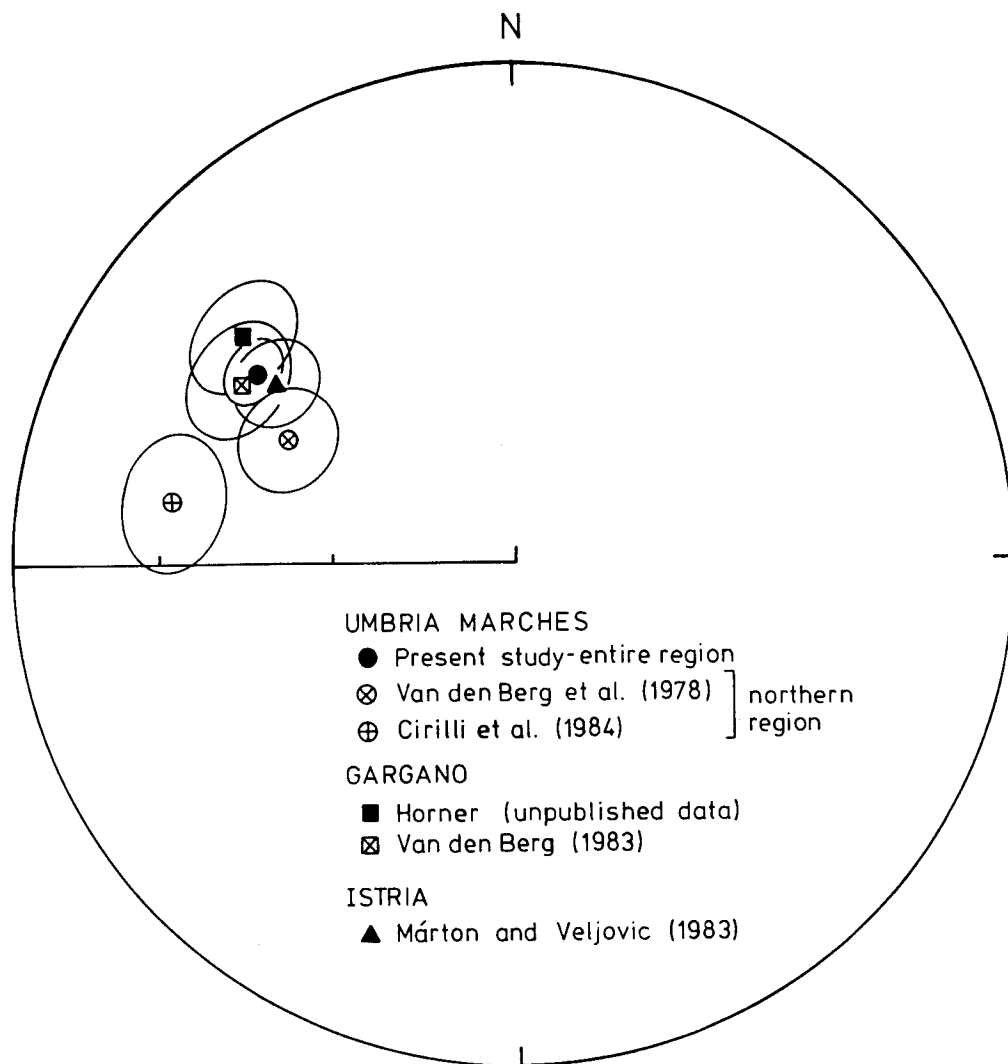
Figure 4.11. Equal area plot of regional paleomagnetic site means of Lower Cretaceous age with circles at 95% confidence for autochthonous areas of the Adriatic promontory.

4.5 Conclusions

Paleomagnetic data from the Umbria-Marches region do not support the interpretation of oroclinal bending. The curvature of the northern Apennines is more likely due to the ramp-thrust tectonics characteristic to the region. However, the results do suggest that there is a regional N-S difference in the data, but that the mechanism responsible for the between-site scatter of the declinations, is in operation throughout the entire fold belt.

The mean paleomagnetic direction for all the Majolica sites is in good agreement with the directions of known autochthonous areas of the Adriatic promontory. This agreement suggests that the Umbria-Marches allochthon has undergone only a simple translation without major rotation relative to the basement.

Table 4.3 Paleomagnetic directions for Lower Cretaceous rocks from the Adriatic promontory. Number of sites (N), remaining columns as in Table 4.1.

	N	D(^{o})	I(^{o})	k	α_{95}(^{o})
UMBRIA-MARCHES REGION					
This study	31	306.4	36.7	27.0	5.1
Van den Berg et al. (1978)	10	298.6	47.6	-	8.0
Cirelli et al. (1984)	3	280.5	31.3	158.3	9.8
GARGANO					
Van den Berg (1983)	8	303.1	35.1	-	8.7
Horner (Unpublished)	3	309.9	30.5	198.9	8.8
ISTRIA					
Márton and Veljovic (1983)	29	307.2	40.5	-	6.9

Chapter 5. THE ANISOTROPY OF MAGNETIC SUSCEPTIBILITY AS A STRAIN INDICATOR IN RED BEDS OF THE LOWER GLARUS NAPPE COMPLEX, EASTERN SWITZERLAND

5.1 Introduction

Kligfield et al. (1983) showed that the finite strain and the AMS could be correlated in red beds of the Maritime Alps. Siddans et al. (1984) later converted the AMS data from the region to equivalent strain values where strain markers were not available or where the strain could not be determined on a small scale. He used these strain data to evaluate the structural and deformational history of the Maritime Alps.

Reduction spots provide good strain markers in red shales and slates of the Lower Glarus Nappe complex. Early studies described the deformation of the reduction spots in two-dimensions in parts of the complex (Huber, 1964; Ryf, 1965; Kühn, 1966, Markus, 1967; Richter, 1968). Advances in strain analysis techniques made three-dimensional analysis of the finite strain possible in the Lower Glarus Nappe complex (Siddans, 1979; Pfiffner, 1981). Since the finite strain is well-defined and consistent in large areas, the complex is ideal to compare different correlations of the finite strain and the AMS. Borradaile and Mothersill (1984) have suggested that direct comparisons of the lengths of the principal axes of strain or strain ratios with lengths of the principal axes of the susceptibility anisotropy or anisotropy ratios should be possible.

5.2 General Geology of the Lower Glarus Nappe Complex

Red bed sediments of the Permian Verrucano and Triassic Quartenschiefer Formations are found in the Lower Glarus Nappe complex of the Helvetic zone. Four major stages of deformation, occurring from 40 Ma to 5 Ma, can be identified in the Helvetic zone of eastern Switzerland (Milnes and Pfiffner, 1977, 1980; Pfiffner, 1977, 1978, 1981). These include: the Pizol phase, a period of tectonic burial with the emplacement of exotic flysch strips; the Cavistrau and Calanda phases, characterized by the formation of the fold and thrust structures and development of axial planar, thrust-parallel cleavage; and the Ruchi phase, with the formation of crenulation cleavage and with further displacement on the Glarus overthrust which leads to an inversion of metamorphic zonation (Frey et al., 1974). Only low grade metamorphism was reached during the time

of main deformation in the study area (Frey et al., 1974; Siddans, 1979; Groshung et al., 1984).

Green reduction spots found in the shale-slate members of the Verrucano and Quartenschiefer formations show flattening in the cleavage plane. They also show a north-south extension in the gently south-dipping penetrative cleavage. The finite strain ellipsoids derived from these spots have been described by several authors (Ryf, 1965; Kühn, 1966; Siddans, 1979; Pfiffner, 1981). Most of these analyses were limited to two-dimensions (Figure 5.1a). The intensity of deformation is heterogeneous, but an average intensity can be estimated from the spot measurements. Typical ratios of the strain principal axes (X > Y > Z) are between 1.65 and 3.53 (mean for sixteen sites, 2.36) for X/Y, and between 2.9 and 12.7 (mean 6.9) for X/Z. Fabric analysis on thin sections has been done by Siddans (1979), who showed that platelets of illites, chlorites and hematites are preferentially aligned in the slatey cleavage plane.

The fold axis orientation at the Malm level of stratigraphy in the Glarus area shows a consistent trend of N60°E. At the Triassic level the fold axes trend east-west along the Walensee and north-south in the extreme southeast, where sites 8 and 9 are located. The fold axes of the central area are scattered due to strain accomodation at fault terminations.

5.3 Sampling and Magnetic Mineralogy

A total of twenty-seven sites were collected in the Lower Glarus Nappe complex, mainly from the Spitzmeilen and Murgtal areas (Figure 5.1b). Reduction spots were measured by the author at nine sites on at least three, non-perpendicular surfaces. Between ten to fifty spots were measured for each surface. The shape ratio and orientation of the spots were extremely consistent for each surface, so that an average spot ratio and orientation could be derived accurately from as little as ten spots on a surface. The finite strain was derived using the program TRISEC, a method described by Milton (1980, see Chapter 3.5). Strain data for four additional sites were provided by Dr. O. A. Pfiffner of the Université de Neuchâtel.

The shape of the IRM acquisition curve is concave upwards below 0.2T, suggesting the absence of a low coercivity component (Figure 5.2). The IRM then increases rapidly until 2.0T where the curve starts to flatten. Total saturation is not reached by 3.5T. Thermal demagnetization of the saturation magnetization shows that over 60% of the saturation
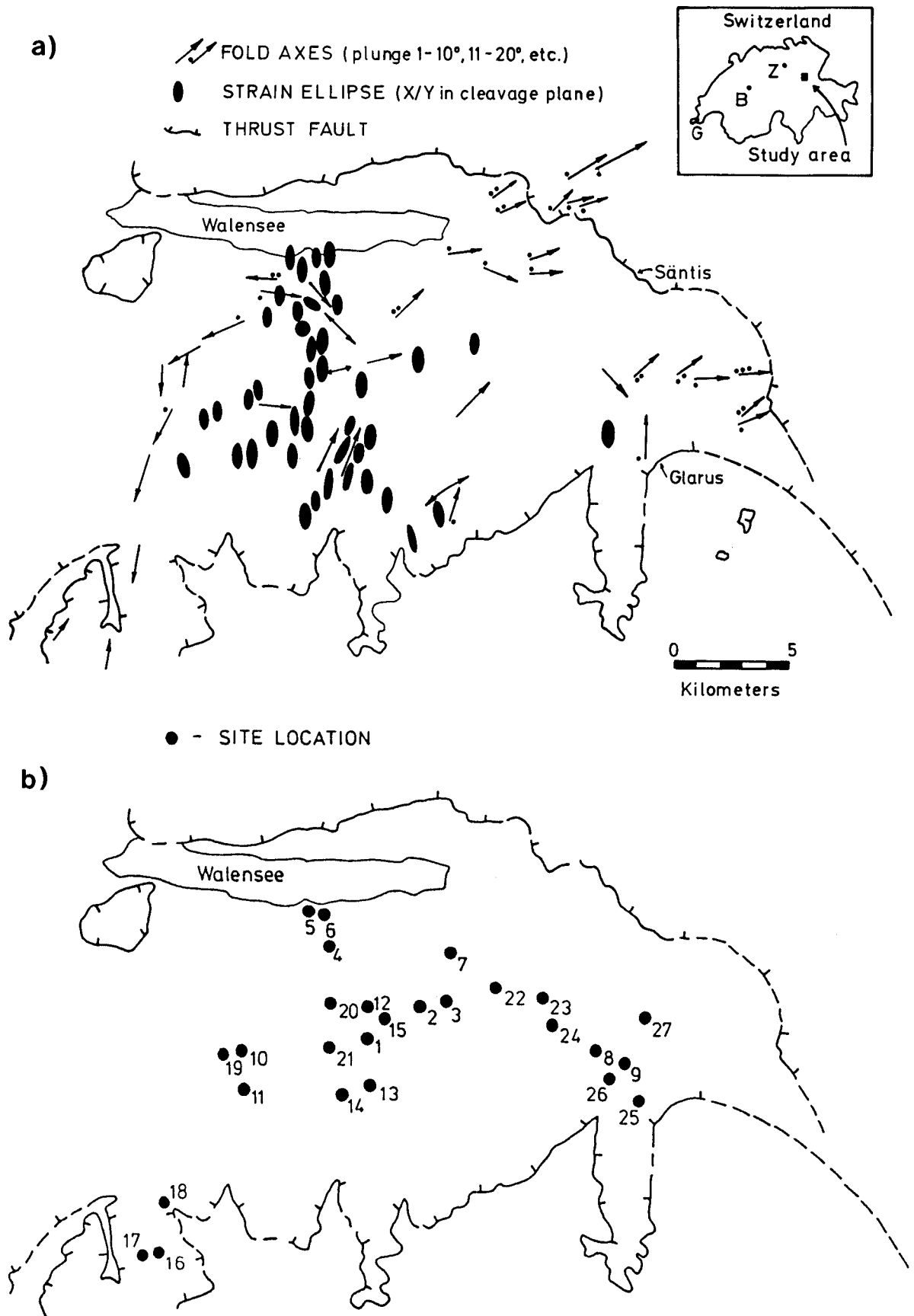
Figure 5.1. Generalized map of the study area. a) Structural data after Pfiffner (1981); including results from Huber (1964),Schielly (1964), Ryf (1965), Kühn (1966), Markus (1967), Richter (1968) and Pfiffner (1981). b) Paleomagnetic site locations.
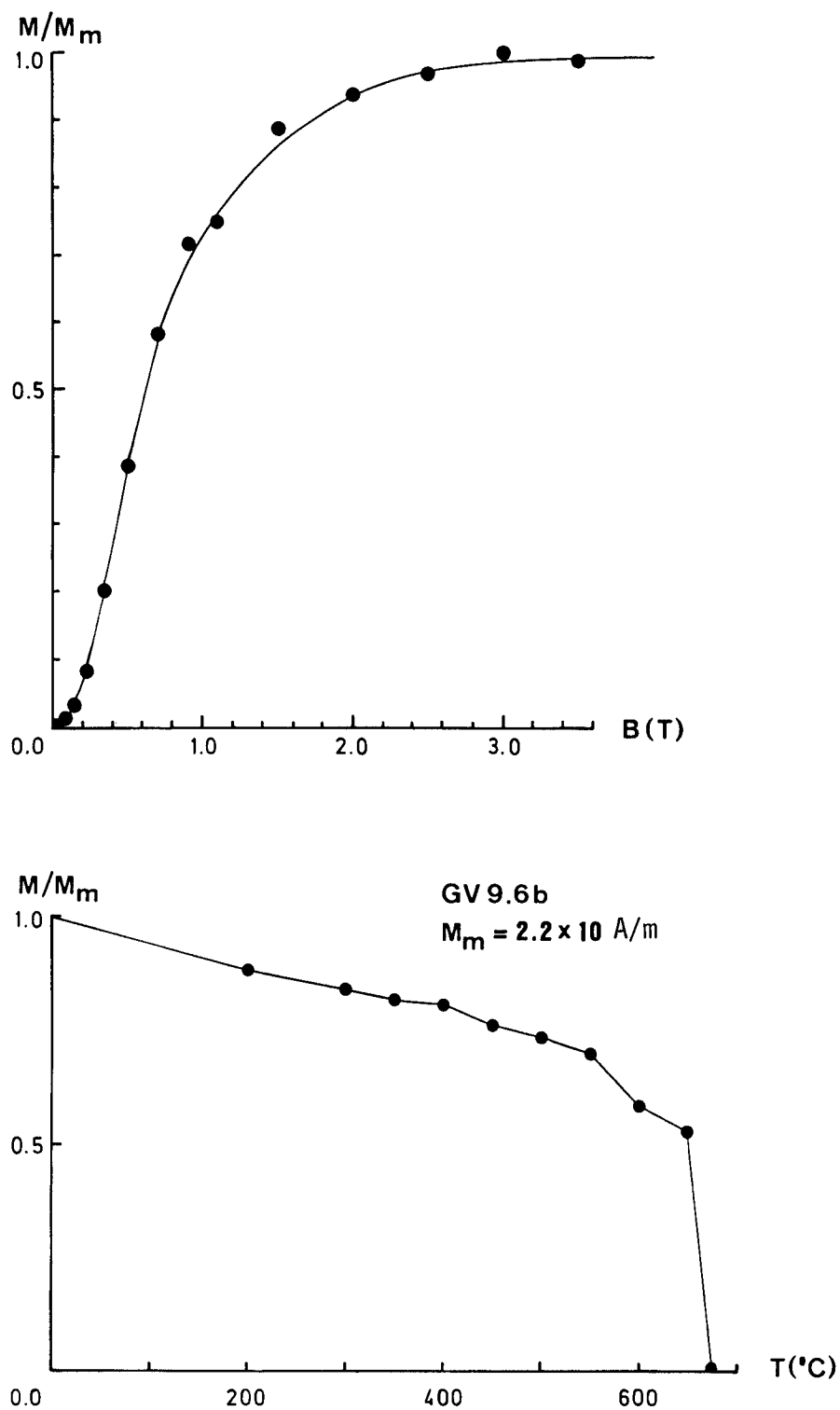
Figure 5.2.   Isothermal remanent magnetization (IRM) and thermal demagnetization of the saturation IRM for a representative specimen.

magnetization is still present by 600°C. The higher temperature, ChRM component is probably carried by a narrow range of single domain hematite grain sizes.

Curie temperature analysis also indicates that hematite is the sole ferromagnetic mineral in these rocks (Figure 5.3). A large paramagnetic contribution is found and Curie temperatures are defined between 680°C and 690°C. The intensity of the saturation magnetization is less during cooling. This implies a mineralogical change produced by the heating process. The magnetization of hematite is due to two components related to (a) spin canting and (b) defects in the lattice structure (Stacey and Banerjee, 1974). Heating the specimens above 700°C could cause the defects to heal so that the magnetization upon cooling will be effectively less.

Very fine-grained hematite is probably responsible for the ferromagnetic contribution to the AMS; however, the paramagnetic clay minerals may also contribute to the anisotropy in the red beds. Separation of the hematite and paramagnetic components of the AMS could not be done using a high-field torquemeter since neither component could be saturated in the 1.0T field available. For both fractions the anisotropy arises from the alignment of crystallographic axes of the grains.

M_S/M_o

1.0

T (°C)

200   400   600
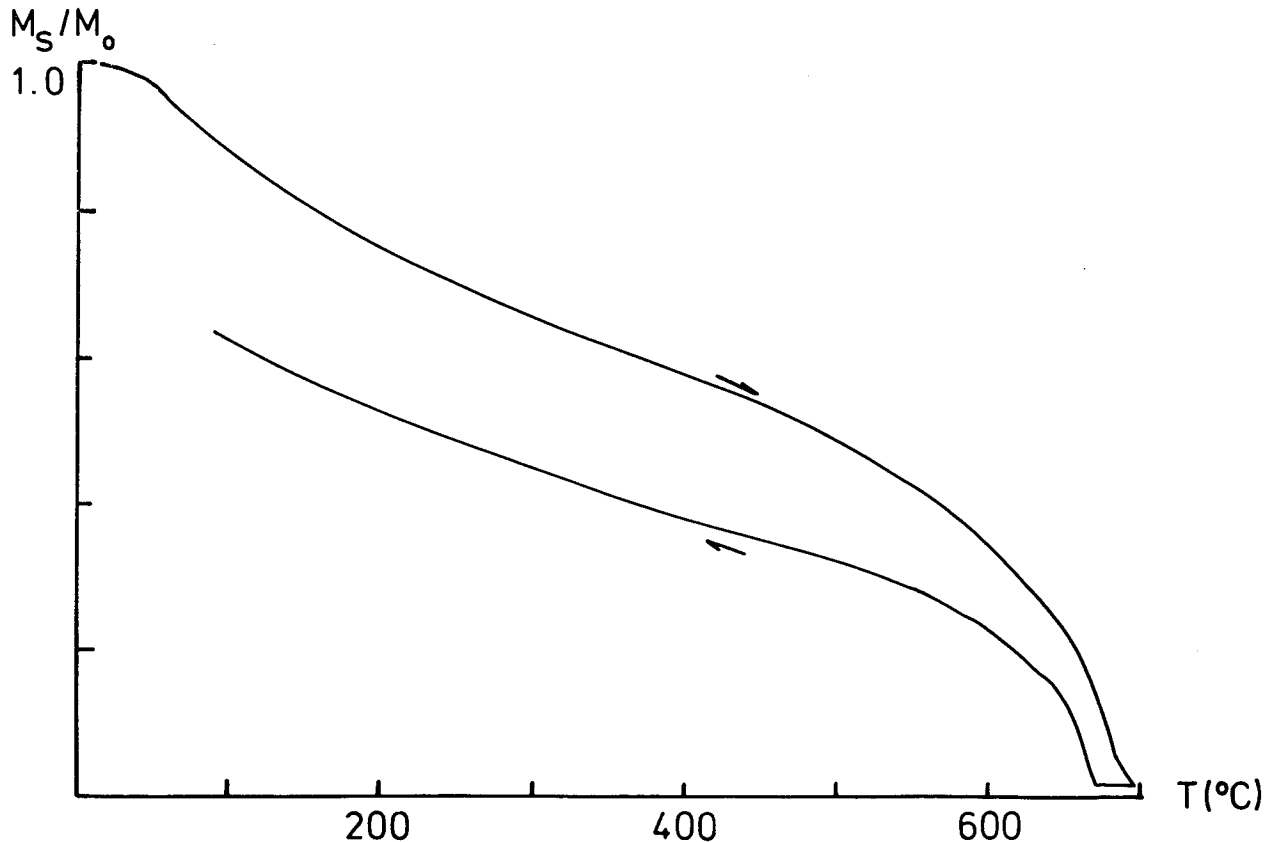
Figure 5.3. Curie temperature anlysis in 0.4T field showing distinct heating and cooling curve for red slates.

5.4 Results

The AMS was measured for six to twenty-eight specimens at each site. The magnetic fabric showed oblate to triaxial ellipsoids, in which the k_{min} axes were always found to be subnormal to the cleavage plane (Figure 5.4 a-d). According to the model of ductile deformation, the hematite grains would have been rotated so that their basal planes statistically align within the cleavage plane. Siddans (1979) has confirmed this realignment of hematite grains in thin section analysis.

An average ellipsoid was calculated for each site using AVANI, described in Chapter 3.2. Within a site single specimens sometimes display interchanged susceptibility axes. Some of the susceptibility magnitude ellipsoids are nearly completely oblate in shape and the k_{max} axes may be interchanged with the k_{int} axes, as in Figure 5.4a. This interchange can result from two mechanisms. The first is a result of machine noise while measuring the anisotropy. The Digico measures susceptibility differences, and when these differences are small the variable background noise may be comparable to that of the measured signal. Therefore it is possible that the noise added to the signal causes the true intermediate axis to appear larger than the true maximum axis. A second explanation, which may be valid when all the specimens of a core show this interchange of axes, is that the core reflects a local strain phenomenon. The strain derived from the reduction spots indicate the strain over the area of the outcrop. The strain of the specimens of a core could reflect the strain that a small localized area has undergone. Fuller (1964) found that sediments are more sensitive to the small-scale stress environment within the rock than to the large scale stresses.

Site means for the AMS magnitude ellipsoids are shown in Figure 5.5 (Appendix B, Table B.1). The k_{min} axes are subnormal to the cleavage plane and there is a north-south lineation. Figure 5.6a shows the predominant north-south stretching lineation of the strain ellipsoid (Appendix B, Table B.2). The shortening is subnormal to the cleavage plane, and the individual directions of the principal axes of the AMS and strain ellipsoids are in good agreement (Figure 5.6b), so that the finite strain and AMS magnitude ellipsoids can be considered to be coaxial.

The lengths of the principal axes of the two ellipsoids can be correlated in several ways. These include:

a)

SITE GV7
IN GEOGRAPHIC COORDINATES

b)

IN CLEAVAGE COORDINATES
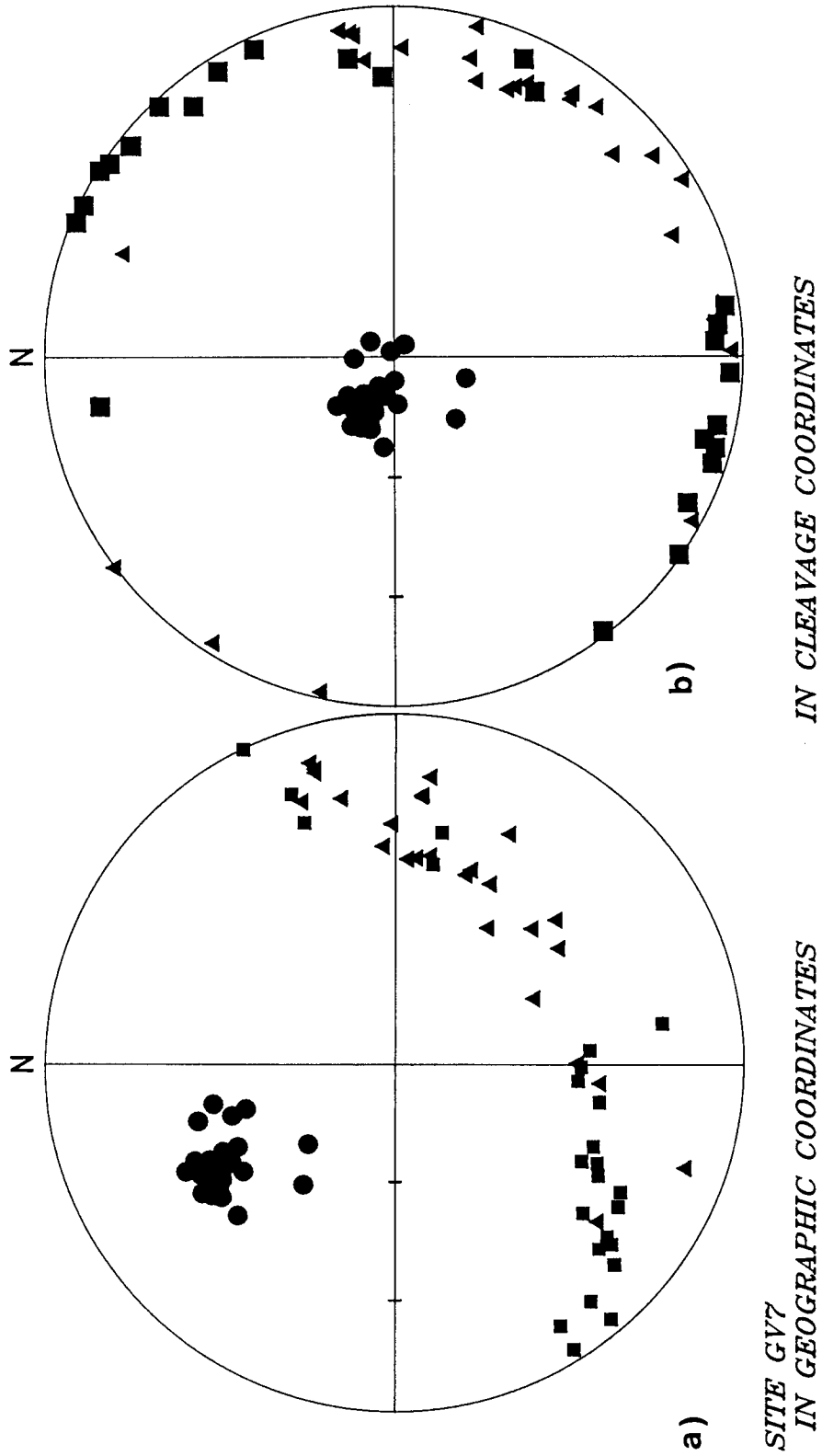
Figure 5.4. Equal area plots of the principal axes of the susceptibility magnitude ellipsoid for two representative site. Symbols: squares, k_{max} axes; triangles, k_{int} axes; and circles, k_{min} axes for this and subsequent figures.

c)

SITE GV13
IN GEOGRAPHIC COORDINATES

d)

IN CLEAVAGE COORDINATES
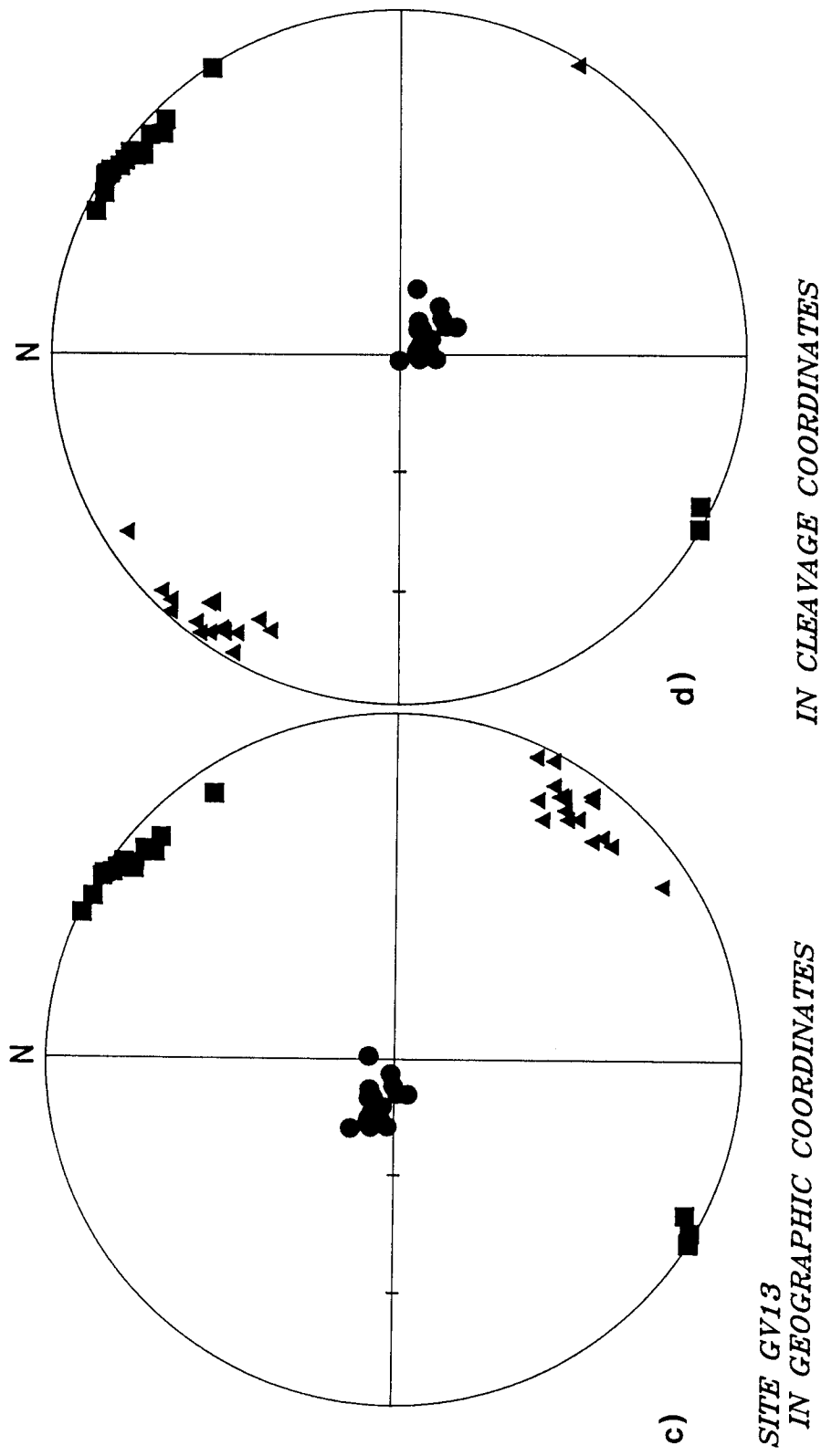
Figure 5.4. (continued)
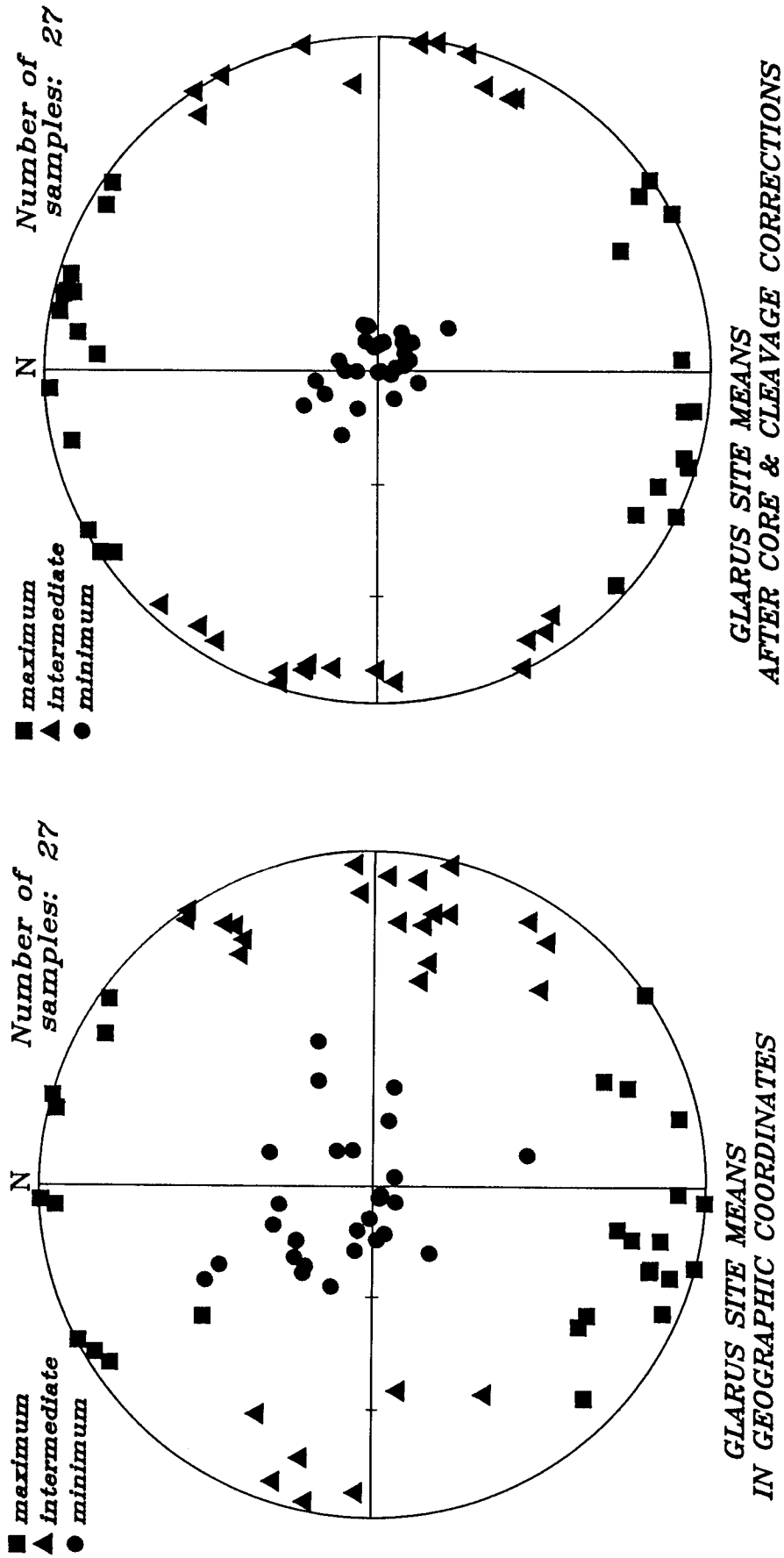
Figure 5.5. Principal axes of the susceptibility magnitude ellipsoid for each site in geographic and cleavage coordinates.
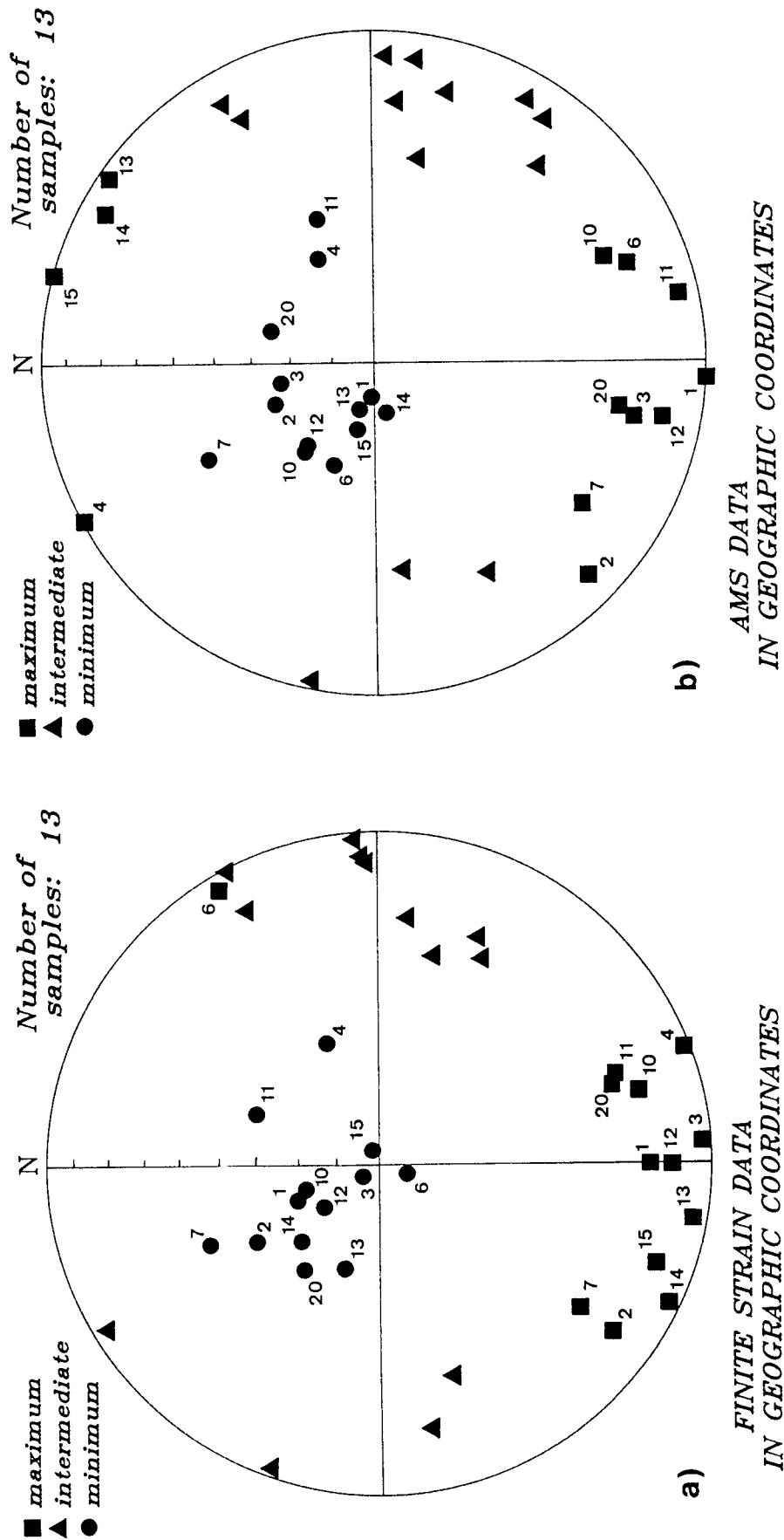
Figure 5.6. a) Principal axes of the finite strain ellipsoid. Symbols: squares, X-axes; triangles, Y-axes; and circles, Z-axes. b) Principal axes of the magnetic susceptibility for sites in which the finite strain was computed.

(1) a direct correlation of the normalized principal axes of the strain and susceptibility magnitude ellipsoids, e.g., $X_1/\bar{X}$ with $k_{max}/\bar{k}$, etc., where $\bar{X} = (X_1 X_2 X_3)^{1/3}$ and $\bar{k} = (k_1 k_2 k_3)^{1/3}$;

(2) a comparison of the ratios of the principal axes, e.g., X/Y correlated with k_{max}/k_{int}, etc.;

(3) the separate correlation for each set of axes of the natural strain, ε_i', with the magnetic parameter, M_i, where $\varepsilon_i' = \ln(X_i/\bar{X})$ and $M_i = (k_i - \bar{k})/\bar{k}$, e.g., ε_1' with M_1, etc.;

(4) a global correlation of all ε_i' with all M_i as done in Kligfield et al. (1981, 1982, 1983); and

(5) a comparison of the shape parameters of the strain and AMS magnitude ellipsoids, where Flinn's k-parameter or Ramsay's K-parameter are correlated against an equivalent magnetic k-parameter (Chapter 3.2).

These five correlation methods will be referred to as Methods 1 to 5 for the remainder of the dissertation.

In order to compare the lengths of the finite strain and susceptibility magnitude ellipsoids on a common plane, the anisotropy ellipsoid was sliced along the principal planes of the finite strain ellipsoid. If the orientations of the two ellipsoids are similar, then the lengths of the principal axes of the AMS ellipsoid will not differ greatly from the lengths of the axes of the elliptical sections of the original magnitude ellipsoid. However, if the orientations of the two ellipsoids differ greatly from one another, then slicing the susceptibility magnitude ellipsoid will yield three axes whose lengths differ significantly from the original ellipsoid, because they are no longer its principal axes. In the above case when the principal axes of the susceptibility magnitude ellipsoid were within $30°$ of the principal axes of the finite strain ellipsoid, the lengths of the axes of the cut ellipsoid were not changed by more than one percent. The orientations of the magnitude ellipsoids for the majority of the Glarus sites were within $15°$ of the orientations of the strain ellipsoids, therefore no sites were rejected on this criterion.

A linear fit was found for each comparison using a first-order regression with bi-square weighting (Wonnacott and Wonnacott, 1985,

p.327). Site GV3 was excluded from the linear fits, because the lengths of the principal axes of the anisotropy ellipsoid were found to be abnormally high. Site GV15 was also excluded from computing the correlation for the ratios (method 2) for similar reasons. The first four correlation methods yield a significant correlation for the maximum and minimum principal axes and the results are given in Table 5.1 (Figure 5.7a-c).

The fifth method, comparing the shape parameters, did not yield a significant correlation. In general, a comparison of the shape parameter for the strain and AMS magnitude ellipsoids will be weak, since the shape of the magnitude ellipsoid is limited whereas the strain is, in principle, unlimited. The AMS can be considered to be a measure of the alignment of the magnetic grains within the rock, when the magnetic fabric arises from crystallographic sources. Even when the crystallographic axes are perfectly aligned, the AMS can not exceed the susceptibility difference between the crystallographic axes. Although strain can continue to increase with tectonic deformation, the degree of anisotropy of the magnitude ellipsoid cannot increase indefinitely, but will approach a limiting value (Hrouda, 1982, Figure 2). Therefore at extremely high strain values the AMS could possibly underestimate the total finite strain undergone by the rocks. The finite strain ellipsoids are flattened in the cleavage plane and show an additional north-south stretching lineation within the cleavage. The grains in the rocks are flattened in the cleavage and aligned subparallel to the lineation and this is reflected in the anisotropy. With continued extension the strain ellipsoid changes from an oblate ellipsoid back to a prolate ellipsoid. However, once the grains are aligned, continued extension along with the flattening will not change the magnetic fabric. The susceptibility magnitude ellipsoid remains oblate (Figure 5.8).

5.5 Discussion

Orientation of the susceptibility magnitude and finite strain ellipsoids

A comparison of the directions of the principal axes of the finite strain and susceptibility magnitude ellipsoids reveals a good overall agreement. The susceptibility magnitude ellipsoid can be considered to be coaxial with the finite strain ellipsoid, and therefore an accurate indicator for the direction of shortening and extension at a site.

Table 5.1. Correlation of the finite strain with the AMS. N is the number of sites used in computing the regression. The correlation coefficients are significant at the 95% confidence level, except for those indicated by a star.

Direct comparison of principal axes (Method 1). N = 12 (GV3 excluded)	Comparison of ratios of the principal axes (Method 2). N = 11 (GV3 and 15 excluded)	Separate comparison of ε_i' and M_i (Method 3). N = 12 (GV3 excluded)	Global correlation of ε_i' and M_i (Method 4). N = 36 (GV3 excluded)
$X = 65.08\, k_{max} - 64.02$ $r = 0.90$	$\dfrac{X}{Y} = 63.43\, \dfrac{k_{max}}{k_{int}} - 61.95$ $r = 0.65$	$\varepsilon_1' = 29.41 M_1 + 0.24$ $r = 0.85$	$\varepsilon_i' = 32.61 M_i$ $r = 0.97$
$Y = 17.12\, k_{int} - 16.26$ $r = 0.49^*$	$\dfrac{Y}{Z} = 61.38\, \dfrac{k_{int}}{k_{min}} - 60.79$ $r = 0.67$	$\varepsilon_2' = 15.12 M_2 - 0.01$ $r = 0.48^*$	
$Z = 9.12\, k_{min} - 8.45$ $r = 0.88$	$\dfrac{X}{Z} = 151.6\, \dfrac{k_{max}}{k_{min}} - 152.9$ $r = 0.85$	$\varepsilon_3' = 22.47 M_3 - 0.22$ $r = 0.83$	
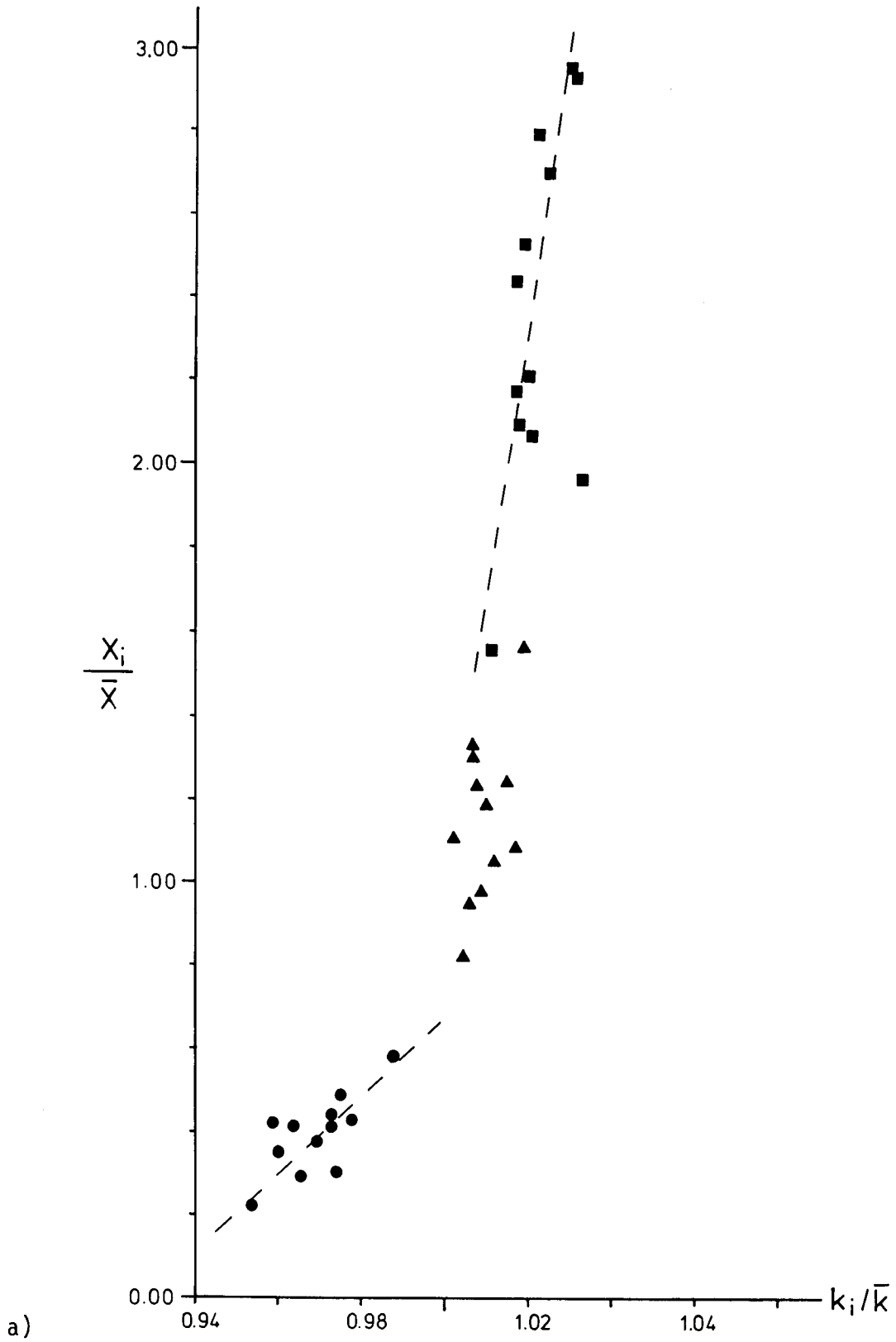
Figure 5.7. Finite strain - AMS correlations for the four correlation methods. a) Method 1; b) Method (2); and c) Method (3) and (4), where the dashed line gives the regression of the individual axes and the solid line the regression of all three groups together. Regression lines are plotted when the correlation is significant at the 95% confidence level.
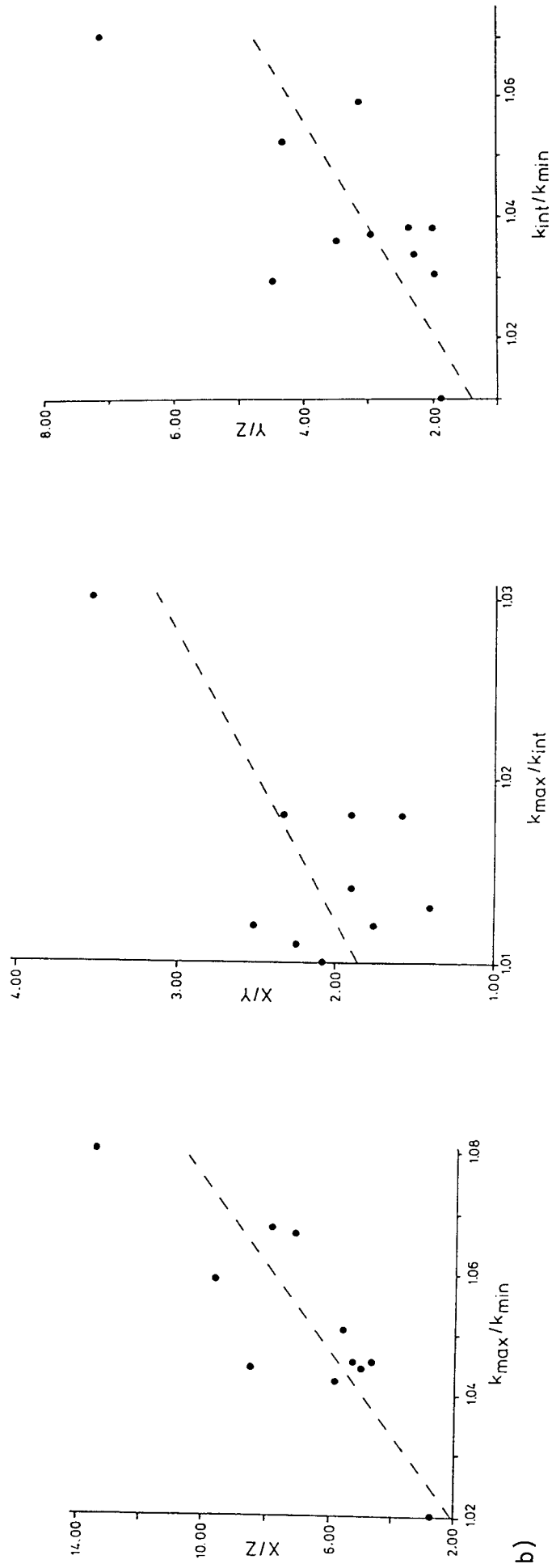
Figure 5.7. (continued)
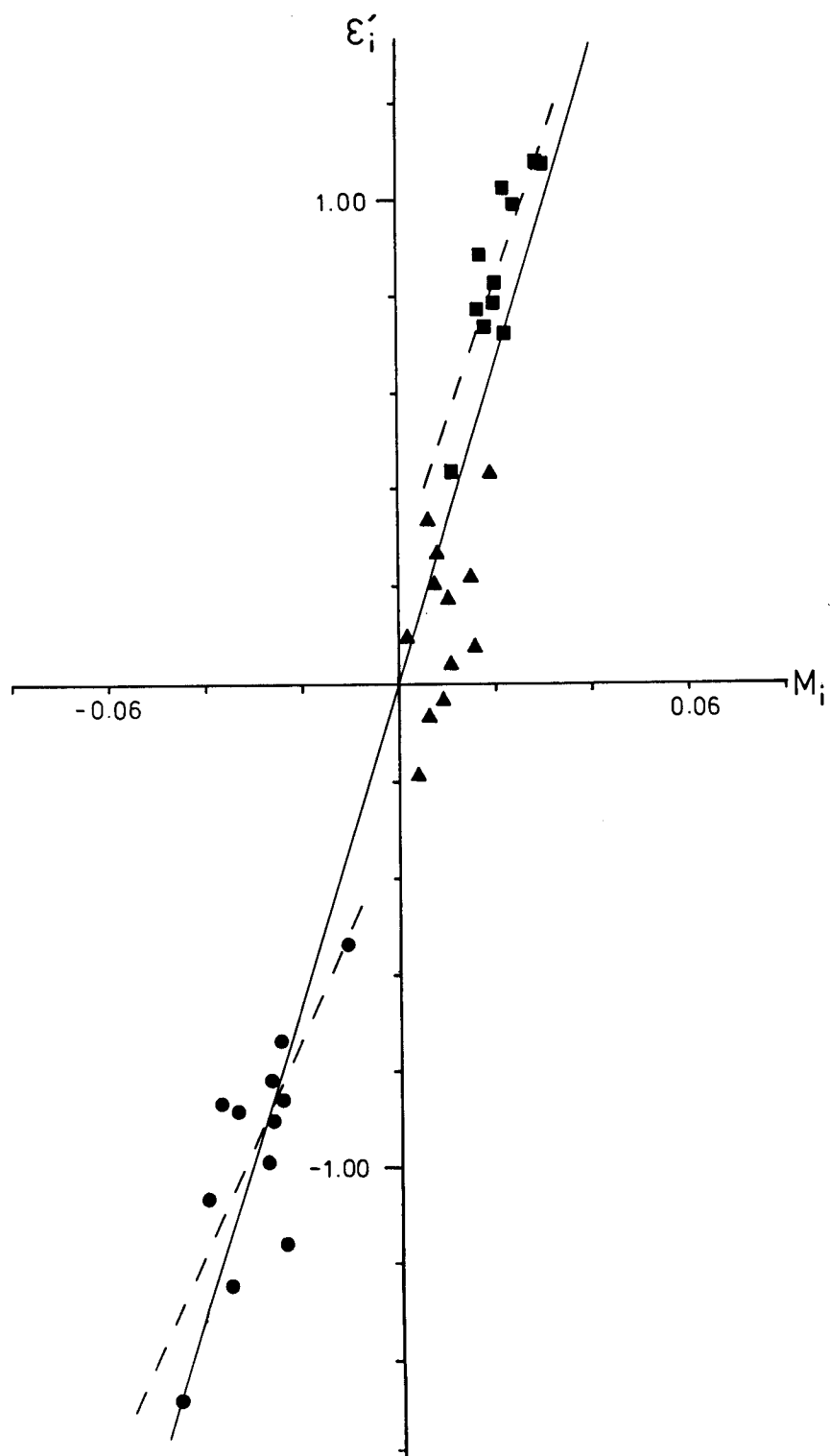
c)

Figure 5.7. (continued)

Shape of the susceptibility magnitude and finite strain ellipsoids

With four methods to correlate the finite strain with the anisotropy, four different values for each of the maximum, intermediate and minimum finite strains will be defined. It is important to determine which value approximates most closely the true strain. TRISEC does not give the absolute lengths of the principal axes of the strain ellipsoid, but the lengths relative to one another. For this reason it is more accurate to compare the ratios of the axes derived from the four methods rather than their absolute lengths. Most important are the flattening within the cleavage or X/Z ratio, and the amount of extension within the cleavage, the X/Y ratio.

The degree of flattening can be calculated from the four correlation methods. Methods 1, 3 and 4 require that equivalent values for X and Z be defined, from which the X/Z ratio is then calculated. Method 2 compares this ratio directly. Table 5.2 lists the derived X/Z values for the twenty-seven sites using the four correlations. All four methods yield a mean value of strain (5.89, s.d. 2.94 to 6.63, s.d. 2.68, n=11) for the Lower Glarus Nappe complex which is comparable to the mean of the actual measured strain values 6.82, s.d. 2.97, n=11). Methods 1, 2 and 3 yield very similar results for the twenty seven sites, whereas the strains derived from the "global correlation" (Method 4) tend to be lower than those derived from the other methods. The ratio correlation (3) also tends to yield lower strains in the least deformed rocks and slightly higher strains in the most deformed rocks. In general, however, all four methods lead to a reasonable approximation of the strain. Individual site values can vary, particularly where the deformation is weak, but the overall mean for the nappe complex is approximately the same.

To compare the degree of extension within the cleavage plane, the X/Y ratio must be derived. Methods 1 and 3 do not yield a significant correlation on the 95% confidence level for the intermediate axes, therefore methods 2 and 4 are the only two correlation methods which can be employed. Table 5.3 lists the results for these two methods. The ratio correlation (Method 2) can either correlate k_{max}/k_{int} directly with the measured X/Y values or X/Y can be calculated from the derived strains Y/Z and X/Z, using X/Y = (X/Z)(Z/Y). The strain ratios derived from the ratio and global correlations are significantly different. The ratio correlation results in mean values (2.08, s.d. 0.39, 2.20, s.d. 0.36, n=11) similar to the actual strain values (2.16, s.d. 0.58, n=11). The
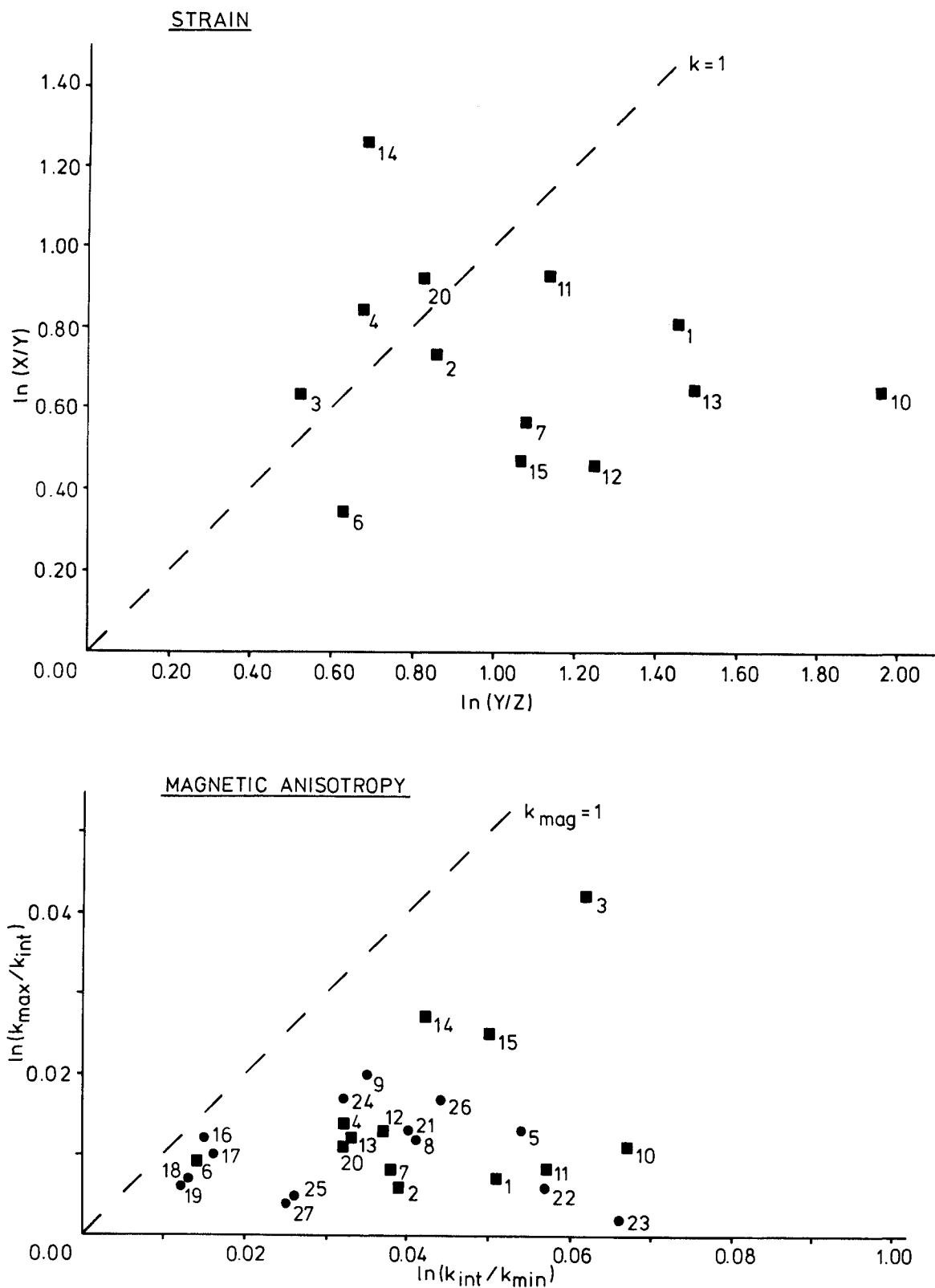
Figure 5.8. Logarithmic plots for the finite strain and the susceptibility magnitude ellipsoids.

Table 5.2. Comparison of the X/Z ratio for the derived finite strain and directly measured finite strain values. GV3 and GV15 were excluded from calculation of the means.

Site	Method 1	Method 2	Method 3	Method 4	Strain from reduction spots
GV1	7.188	7.768	7.031	6.416	9.633
GV2	5.144	4.737	5.071	4.199	4.902
GV3	24.135	15.044	24.552	29.709	3.160
GV4	5.320	4.737	5.295	4.338	4.973
GV5	9.149	8.526	9.114	8.889	
GV6	3.132	2.160	3.035	2.117	2.629
GV7	5.254	5.798	5.223	4.338	5.173
GV8	6.428	7.011	6.427	5.631	
GV9	6.697	7.162	6.711	5.818	
GV10	12.660	11.730	11.650	12.317	13.490
GV11	8.774	8.981	8.593	8.328	7.826
GV12	5.930	6.404	5.966	5.106	5.495
GV13	5.282	5.646	5.259	4.338	8.474
GV14	9.292	9.436	9.650	9.184	7.060
GV15	11.082	10.497	11.451	11.538	4.631
GV16	3.464	3.221	3.366	2.412	
GV17	3.355	2.615	3.269	2.335	
GV18	2.819	1.705	2.798	1.920	
GV19	2.655	1.402	2.656	1.798	
GV20	4.934	5.343	4.993	4.064	5.751
GV21	6.284	6.859	6.284	5.450	
GV22	8.134	8.526	7.922	7.551	
GV23	8.899	8.981	8.475	8.327	
GV24	5.756	6.253	5.744	4.784	
GV25	3.637	3.524	3.657	2.748	
GV26	7.573	8.072	7.733	7.074	
GV27	3.417	3.070	3.473	2.574	

Mean	N=11	N=11	N=11	N=11	N=11
	X/Z=6.63	X/Z=6.43	X/Z=6.52	X/Z=5.89	X/Z=6.82
	s.d. 2.68	s.d. 2.92	s.d. 2.50	s.d. 2.94	s.d. 2.97
	N=25	N=25	N=25	N=25	
	X/Z=6.24	X/Z=6.16	X/Z=6.19	X/Z=5.52	
	s.d. 2.63	s.d. 2.81	s.d. 2.57	s.d. 2.92	

Table 5.3. Comparison of the X/Y ratio. GV3 was excluded from the calculation of the means.

Site	Method 2 X/Y Direct	Method 2 X/Y=(X/Z)(Z/Y)	Method 4	Strain from reduction spots
GV1	1.916	2.045	1.256	2.242
GV2	1.855	1.568	1.216	2.077
GV3	4.187	3.343	4.064	1.881
GV4	2.361	1.858	1.579	2.325
GV5	2.292	2.125	1.528	
GV6	2.080	1.504	1.386	1.404
GV7	1.981	1.976	1.298	1.758
GV8	2.232	2.199	1.479	
GV9	2.741	2.583	1.920	
GV10	2.163	2.424	1.431	1.900
GV11	1.978	2.131	1.298	2.516
GV12	2.297	2.201	1.528	1.580
GV13	2.234	2.114	1.479	1.900
GV14	3.183	2.935	2.412	3.530
GV15	3.115	2.827	2.335	1.593
GV16	2.239	2.130	1.479	
GV17	2.112	1.648	1.386	
GV18	1.922	1.254	1.256	
GV19	1.858	1.065	1.216	
GV20	2.171	2.071	1.431	2.513
GV21	2.296	2.219	1.528	
GV22	1.853	2.036	1.216	
GV23	1.603	1.935	1.067	
GV24	2.552	2.420	1.741	
GV25	1.794	1.589	1.177	
GV26	2.547	2.429	1.741	
GV27	1.731	1.443	1.139	
Mean	N=11 X/Y=2.20 s.d. 0.36	N=11 X/Y=2.08 s.d. 0.39	N=11 X/Y=1.48 s.d. 0.33	N=11 X/Y=2.16 s.d. 0.58
	N=26 X/Y=2.20 s.d. 0.39	N=26 X/Y=2.03 s.d. 0.45	N=26 X/Y=1.48 s.d. 0.33	

global correlation gives consistently lower strain values (1.48, s.d. 0.33, n=11). It should be noted that individual strain values derived from the three correlation methods can vary considerably from the strain directly measured at a site.

Pfiffner (1981) collected and reported the results defined in the earlier studies (Huber, 1964; Ryf, 1965; Kühn, 1966, Markus, 1967; Richter, 1968) of the Lower Glarus nappe complex. The results are shown in Figure 5.9a, where the oriented ellipses (sections through the strain ellipsoid) with axial ratios X/Y in the cleavage plane are plotted on the map surfaces. Plotting the ellipses derived in a similar fashion by the correlation of the finite strain with the susceptibility magnitude ellipsoid using the direct ratio and the "global" methods (Method 2 and 4, respectively), one can visually compare the results with those of the real strain measurements (Figure 5.9b, c). It can be seen clearly that the global correlation produces strain ellipsoids which are more oblate than the actual strains measured. In this case the ratio-derived strains are in closer agreement to the actual strain values.

Analysis of the influence of grain size

Since the rocks under investigation ranged in grain size from very fine claystones to conglomerates, it would be interesting to note if the magnetic or anisotropy parameters vary with grain size. The grain sizes at each site were broadly grouped in three classes: fine-grained mudstones, fine-grained sandstones or coarse-grained sandstones to conglomerates.

No consistent relation is found between grain size and the bulk susceptibility or between grain size and the lengths of the principal axes of the anisotropy ellipsoids. There is only a rough relationship between the grain size and the degree of anisotropy (P_1), which is defined as k_{max}/k_{min}. The fine-grained mudstones and sandstones had an average P_1 value of 1.054 (s.d. 0.015, n=20) and the coarser-grained sediments had an average P_1 value of 1.032 (s.d. 0.017, n=7). Fine-grained hematite was the main magnetic mineral in all the rocks, regardless of their grain size. This may explain why there is little dependence between the magnetic or anisotropy parameters and the grain size of the rock.
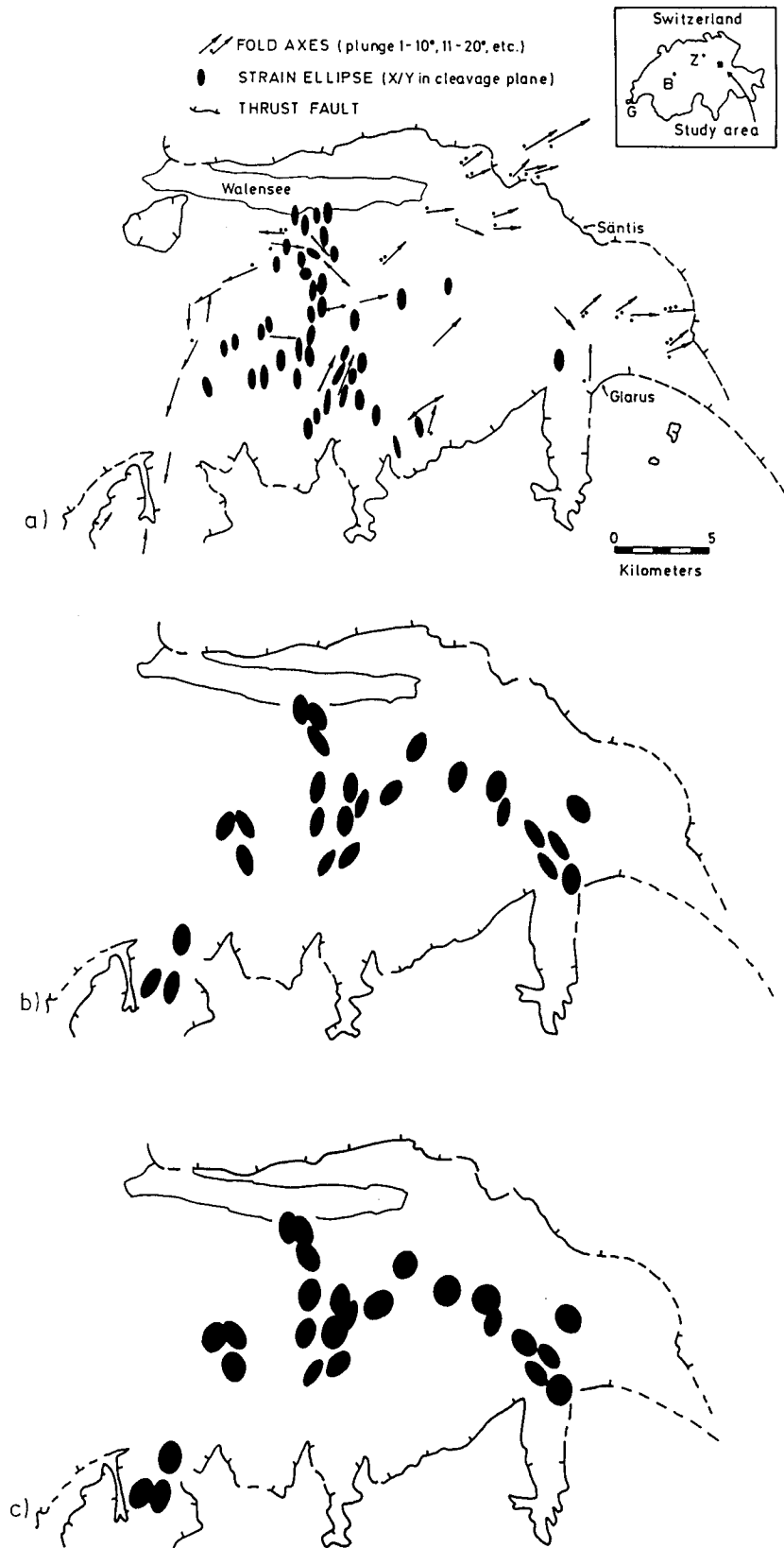
Figure 5.9. a) Generalized map of the study area with strain ellipsoid results from Huber (1964), Schielly (1964), Ryf (1965), Kühn (1966), Markus (1967), Richter (1968) and Pfiffner (1981) (After Pfiffner, 1981). b) Strain ellipsoids calculated from the global correlation (Method 4). c) Strain ellipsoids calculated from the direct ratio correlation (Method 2).

5.6 Conclusions

A very good directional relationship can be found between the finite strain and the AMS. There is also a good agreement between the degree of shortening (X/Z) derived from the AMS and the measured finite strain. The derivation of the lineation within the cleavage plane is more sensitive to the correlation method which is employed. The global correlation method used by Kligfield et al. (1981, 1982, 1983) appears to be inadequate for calculating the equivalent strain in these rocks. The other correlation methods investigated, particularly those which compare individual axes, yield a more accurate representation of the finite strain ellipsoid. Some of these methods of correlation are not always possible, since the intermediate axes are passively defined for the AMS magnitude ellipsoid and tend to be close to the average value of the principal axes of the respective ellipsoids. Methods 1, 3 and 4 are particularly handicapped in this respect since neither the intermediate strain nor the k_{int} values vary greatly throughout the area.

Seite Leer /
Blank leaf

Chapter 6. PALEOMAGNETIC STUDY OF TECTONICALLY DEFORMED RED BEDS OF THE LOWER GLARUS NAPPE COMPLEX

6.1 Introduction

Paleomagnetic studies of red beds in the Maritime Alps illustrated the effects of progressive deformation on remanent magnetization (Kligfield et al., 1983; Cogné and Perroud, 1985). R. Graham (1978) defined four major stages of progressive deformation in the Maritime Alps similar to those defined by J. Graham (1966) in the Appalachians. The least deformed rocks show flattening of the finite strain and the AMS magnitude ellipsoids within the bedding plane due to compaction. The superposition of a tectonic flattening on the compactional loading leads to the formation of pencil structure or a prolate strain and magnitude ellipsoid. The long axis of the ellipsoids are oriented subparallel to the regional fold axes. Slatey cleavage begins to develop with the further application of tectonic flattening. The ellipsoids become oblate and are now flattened in the cleavage plane. If the deformation continues, the oblate ellipsoids become extended down dip in the cleavage plane, resulting in a triaxial ellipsoid (see Figure 1.6).

The triaxial stage of deformation is not completely reached in the Maritime Alps, although the hematite grains are clearly realigned within the cleavage plane. The remanence directions are affected by distortional strains and deviate from the Permian directions (Kligfield et al., 1983; Lowrie et al., 1986).

Permian and Triassic shales and slates from the Helvetic Nappes in eastern Switzerland provide an excellent example of rocks that have undergone triaxial stage deformation. There have been many studies analyzing the deformation, strain and metamorphic grade of these rocks (Oberholzer, 1933; Fisch, 1961; Schielly, 1964; Huber, 1964; Ryf, 1965; Kühn, 1966; Markus, 1967; Richter, 1968; Frey et al., 1974; Pfiffner, 1977, 1978, 1981; Milnes and Pfiffner, 1977, 1980; Siddans, 1979; Groshung et al., 1984; Chapter 5). The remanent magnetization of these red beds has been evaluated to observe the effects that these extreme strains have on the remanence.

6.2 Sampling and Magnetic Properties

The geology of the Lower Glarus Nappe complex is described in Chapter 5.2. Fifteen of the twenty-seven sites (315 samples) collected in the Lower Glarus Nappe complex were used in this paleomagnetic study (Figure 6.1). Since the overall structure of the study area is one of an upright sequence, overturned sequences occur only locally (see Pfiffner, 1981, Figure 2). Overturned bedding can be excluded for all sites with the possible exception of site 14.

The NRM of the samples had intensities ranging from 10^{-4} to 3×10^{-2} A/m. AF demagnetization indicated that there is practically no low coercivity component to the remanent magnetization. Over 80% of the NRM intensity remained after using peak fields of 100 mT. Samples were thermally demagnetized progressively and secondary components of magnetization were isolated, in general, between $300^{\circ}C$ and $600^{\circ}C$. The ChRM directions were isolated between $600^{\circ}C$ and $690^{\circ}C$ (Figure 6.2).

● - SITE LOCATION
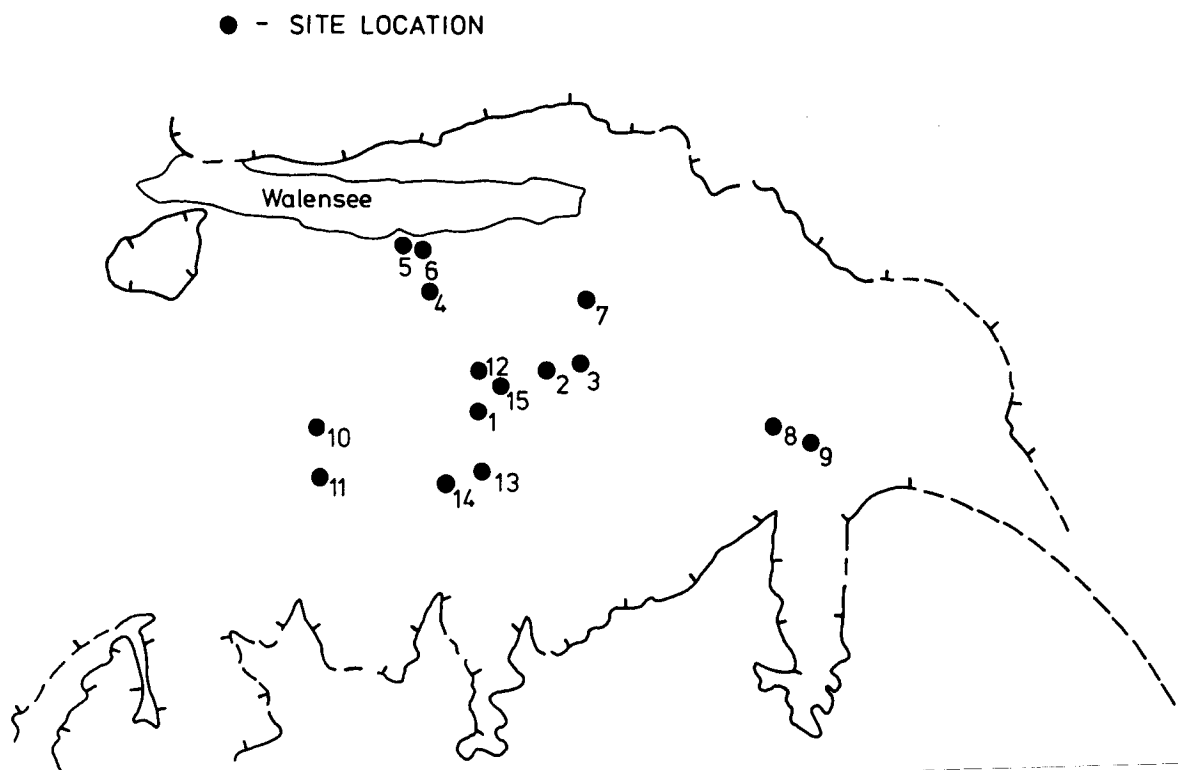

Figure 6.1. Site location map of sites used in the paleomagnetic study of the Lower Glarus Nappe complex.
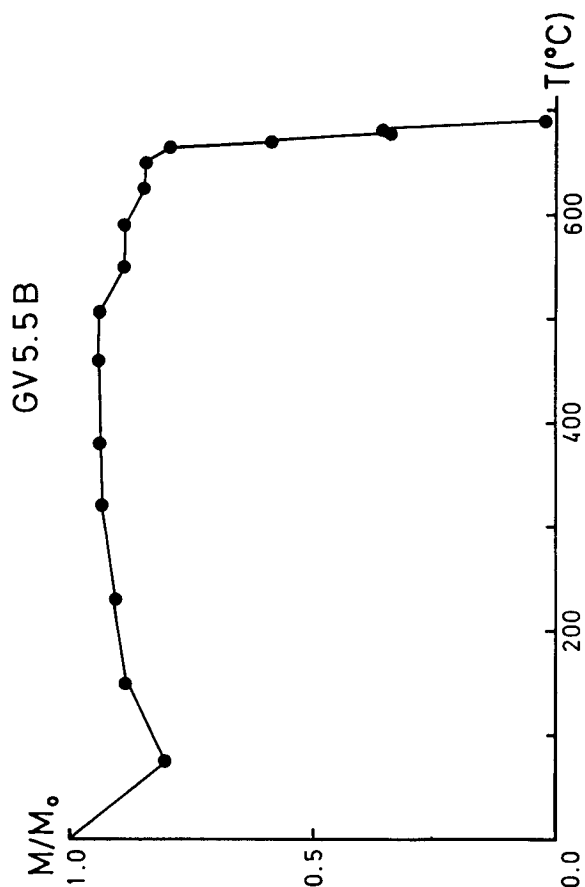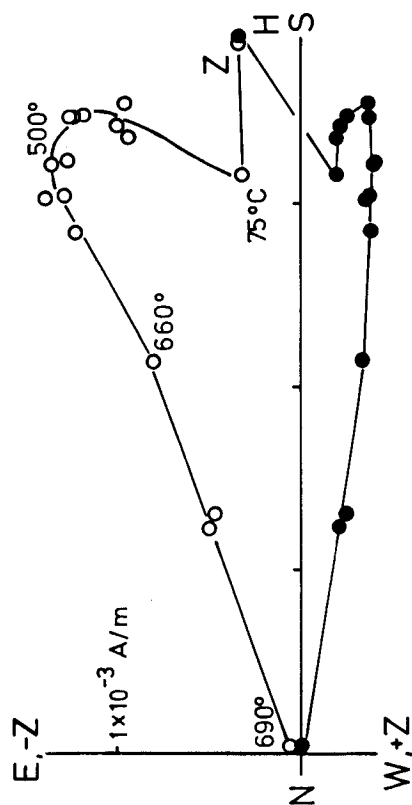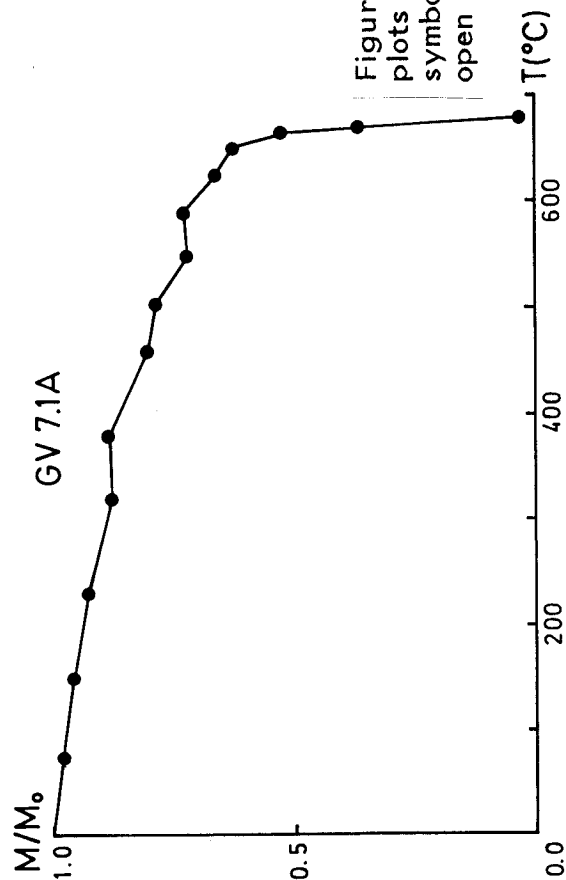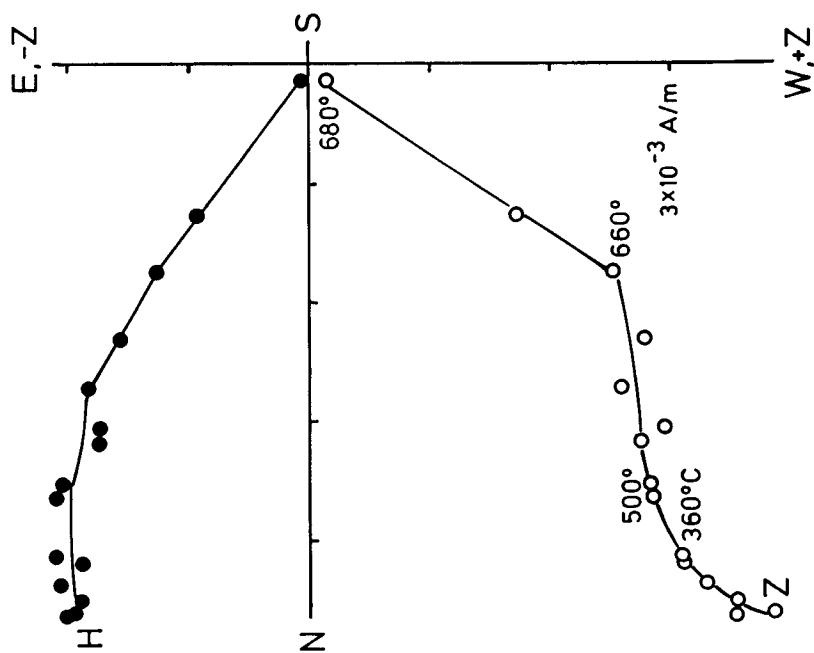
Figure 6.2. Vector diagrams showing directional behavior and normalized plots showing intensity variation during thermal demagnetization. Closed symbols represent vector end-points projected on the horizontal plane; open symbols are projections on the vertical N-S plane.

Thermal demagnetization, the acquisition of IRM and thermal demagnetization of the IRM (Figure 5.2), and Curie temperature analysis (Figure 5.3) all indicate that hematite is the sole magnetic mineral in these red beds.

6.3 Results

Analysis of secondary magnetization

Secondary directions that had a good within-site grouping ($\alpha_{95} < 15°$) could only be isolated at five of the fifteen sites; less well-defined secondary directions ($\alpha_{95} > 20°$) were found at another three sites; at the remaining seven sites the secondary directions could not be defined. One of the eight usable site directions (GV 11) lay more than two standard deviations from the regional mean and was excluded from further analysis (Table 6.1). The mean direction before tectonic tilt correction for the remaining seven sites (D = $14°$, I = $53°$, k = 18, α_{95} = $15°$) is not statistically different from the present field direction of the study area (Figure 6.3). However, this direction lies close to the directions derived from the polar wander path for Europe (1977) for ages less than 100 Ma. Therefore the secondary magnetization could be related to the Tertiary deformation.

Table 6.1. Site mean values of the secondary magnetization directions in the Verrucano and Quartenschiefer formations without tectonic tilt correction. Columns give the site number, number of specimens (n), declination (D) and inclination (I) of site means, k and radius of 95% confidence circle (α_{95}). Starred sites (*) were excluded from the calculation of the mean.

Site	n	D($°$)	I($°$)	k	$\alpha_{95}($°$)$
GV3	3	2.1	57.4	31.0	22.5
GV5	9	31.1	65.4	70.1	6.2
GV6	11	326.6	64.4	40.5	7.3
GV7	12	26.7	44.7	17.3	10.8
GV8	6	37.5	33.8	22.8	14.3
GV10	5	202.4	-48.3	7.9	29.0
GV11*	5	326.7	-9.1	65.8	9.5
GV14*	3	351.1	38.7	13.9	34.4
MEAN		18.8	54.3	18.9	15.8
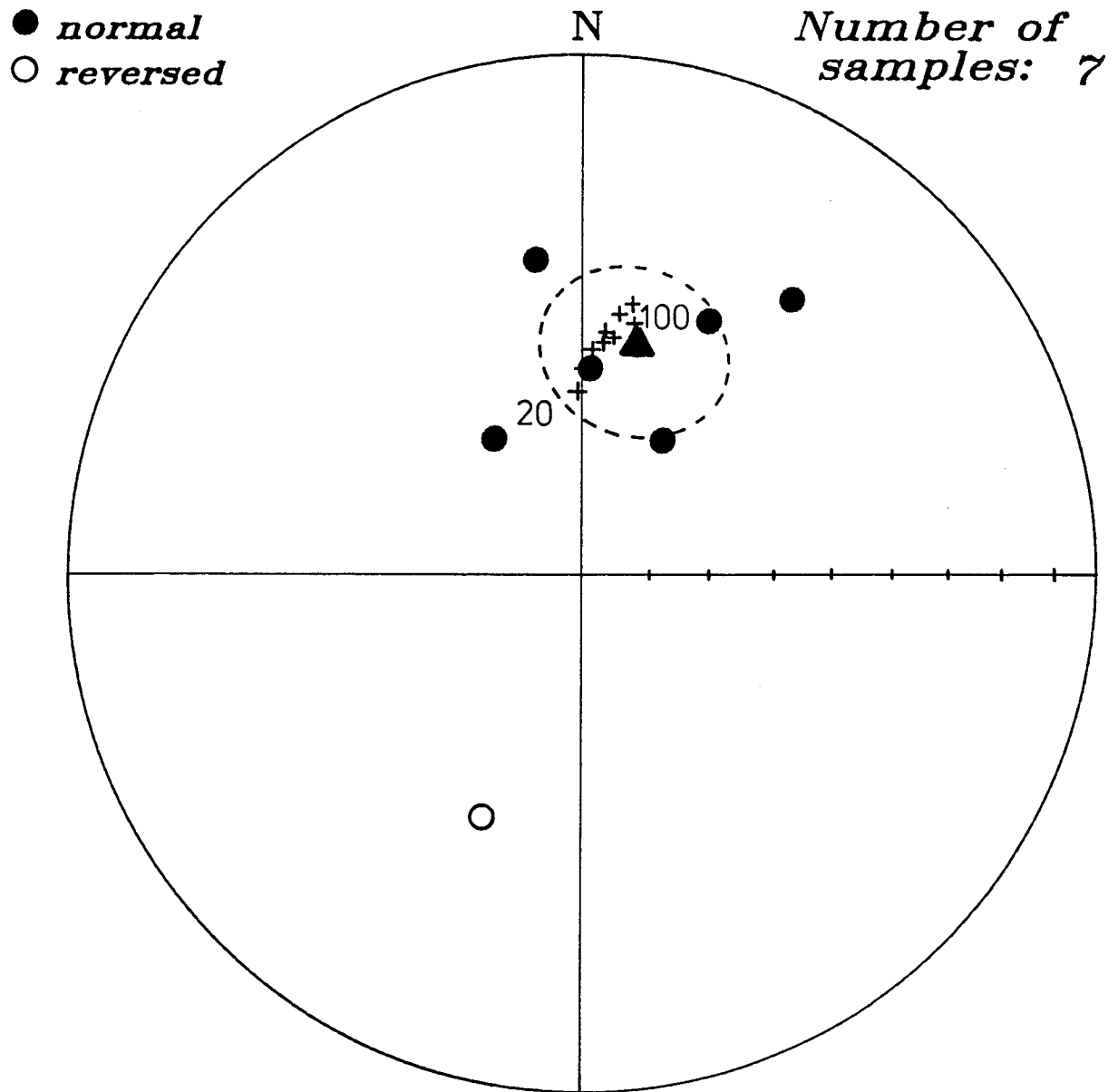
GLARUS SECONDARY DIRECTIONS
IN GEOGRAPHIC COORDINATES

Figure 6.3. Equal area plot showing site means of secondary directions with their circle of confidence. Small crosses represent directions derived from the apparent poles for Eurasia from 100 Ma to present (Irving, 1977). The triangle is the mean direction for the seven site means.

Analysis of characteristic magnetization

The ChRM directions at thirteen of the fifteen sites are well-defined (within-site $\alpha_{95} < 13°$). Due to the intensity of deformation, bedding could not always be measured directly. The local bedding was used for the conventional tilt correction where measureable; otherwise the regional bedding was used, provided that the structure was simple. Within-site scatter is not changed by this correction. There is a large between-site scatter which is not altered appreciably by applying the regional tectonic tilt correction, because bedding was generally flat (Figure 6.4). The distribution of directions is Fisherian and gives a mean direction (tilt-corrected) for the thirteen sites of D = 74°, I = 47° (k = 5.0, $\alpha_{95} = 21°$) (Table 6.2).

In Chapter 5 the magnetic fabric of the red beds indicated that the hematite grains have had their basal planes aligned within the cleavage. This has also been reported by Siddans (1979) in thin section analysis. If the hematite grains have been reoriented according to the model for ductile deformation, we can expect that the characteristic remanence vector also will have its orientation affected.

Table 6.2 Paleomagnetic site means directions of the Verrucano and Quartenschiefer formations corrected for tectonic tilt. Col-umns give the site number, number of specimens (n), decli-nation (D) and inclination (I) of site means, k and radius of 95% confidence circles (α_{95}). Starred sites (*) were exclud-ed from calculation of the mean.

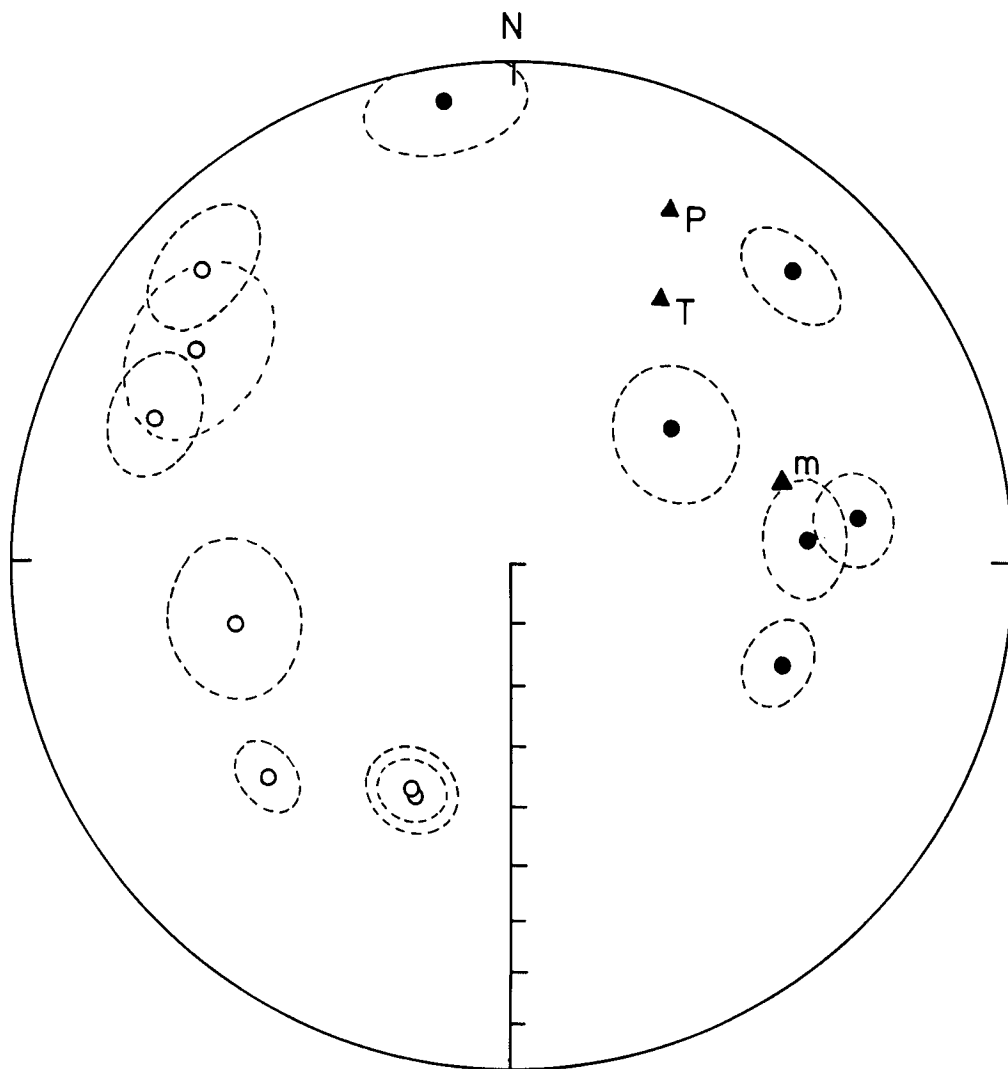| Site	n	D(°)	I(°)	k	α_{95}(°)
GV1	12	203.0	-50.0	65.8	5.4
GV2	4	49.5	56.0	83.6	10.1
GV3	5	85.5	40.5	76.5	8.8
GV5	12	202.5	-49.0	38.6	7.1
GV6	7	258.0	-44.5	23.5	12.7
GV7	14	110.5	42.0	38.3	6.5
GV8	8	82.5	31.0	38.4	9.1
GV9	10	352.0	9.0	23.6	10.2
GV10	12	229.0	-36.5	66.9	5.3
GV11	10	313.7	-16.7	30.2	8.9
GV12	8	304.6	-24.9	20.1	12.7
GV13	11	292.0	-25.0	25.5	9.2
GV14*	7	328.0	23.0	3.3	39.8
GV15	10	44.5	20.5	40.2	7.7
MEAN		73.8	47.3	5.0	20.6

Figure 6.4. ChRM directions after tectonic tilt correction plotted with their circles of confidence. ▲m is the mean ChRM direction, ▲P is the predicted Permian direction, and ▲T is the predicted Triassic direction for stable Europe (Van der Voo and French, 1974).

6.4 Discussion

Hargraves Model for the Acquisition of the ChRM Directions

Hargraves (1959) suggested that ore samples in which the remanent magnetization is carried by hematite could have their magnetization deflected from the ambient field towards the plane of the magnetic foliation. This implies that an anisotropy must exist in the sample before the remanent magnetization is acquired. The true direction of magnetization would therefore have to lie on a great circle between the observed direction and the pole to the magnetic foliation or k_{min} axis. The great circles for all specimens at a site should intersect at the true remanent direction.

If the characteristic directions were magnetized during the Alpine deformation, then the scatter seen in their distribution may be due to the anisotropic acquisition of the magnetization. The greatest density of the intersection points of the great circles lies close to the earth's present field direction (Figure 6.5). This would suggest that the red beds have been remagnetized during or since the Tertiary deformation in at least two polarity intervals. Although this interpretation is possible, the method of intersecting circles contains its own biases.

First, the method only states that the remanence is deflected along a great circle but not the amount of deflection. Two great circles for two samples must intersect, but this intersection need not have a physical meaning. Second, by increasing the number of observations, the number of common hemisphere intersections increases rapidly, N great circles yield $N(N-1)/2$ intersections (Ramsay, 1967) so that for N > 3, the number of intersections outnumbers the number of observations. Third, if there is an extreme case where the k_{min} axes are so well-grouped as to define one point and the remanences are scattered, then the great circles will have to intersect at the k_{min} axes. This intersection does not reflect the ancient field direction, but in the present case the direction of maximum shortening. This suggests that for the two groups of data being plotted, remanence and the k_{min} directions, the highest concentration of intersections would lie closer to the group with the least dispersion. Therefore, the position of the maximum density of intersections may have no physical meaning.

For the Glarus data the k_{min} axes are better grouped than the remanence directions, so that we would expect the intersections to lie
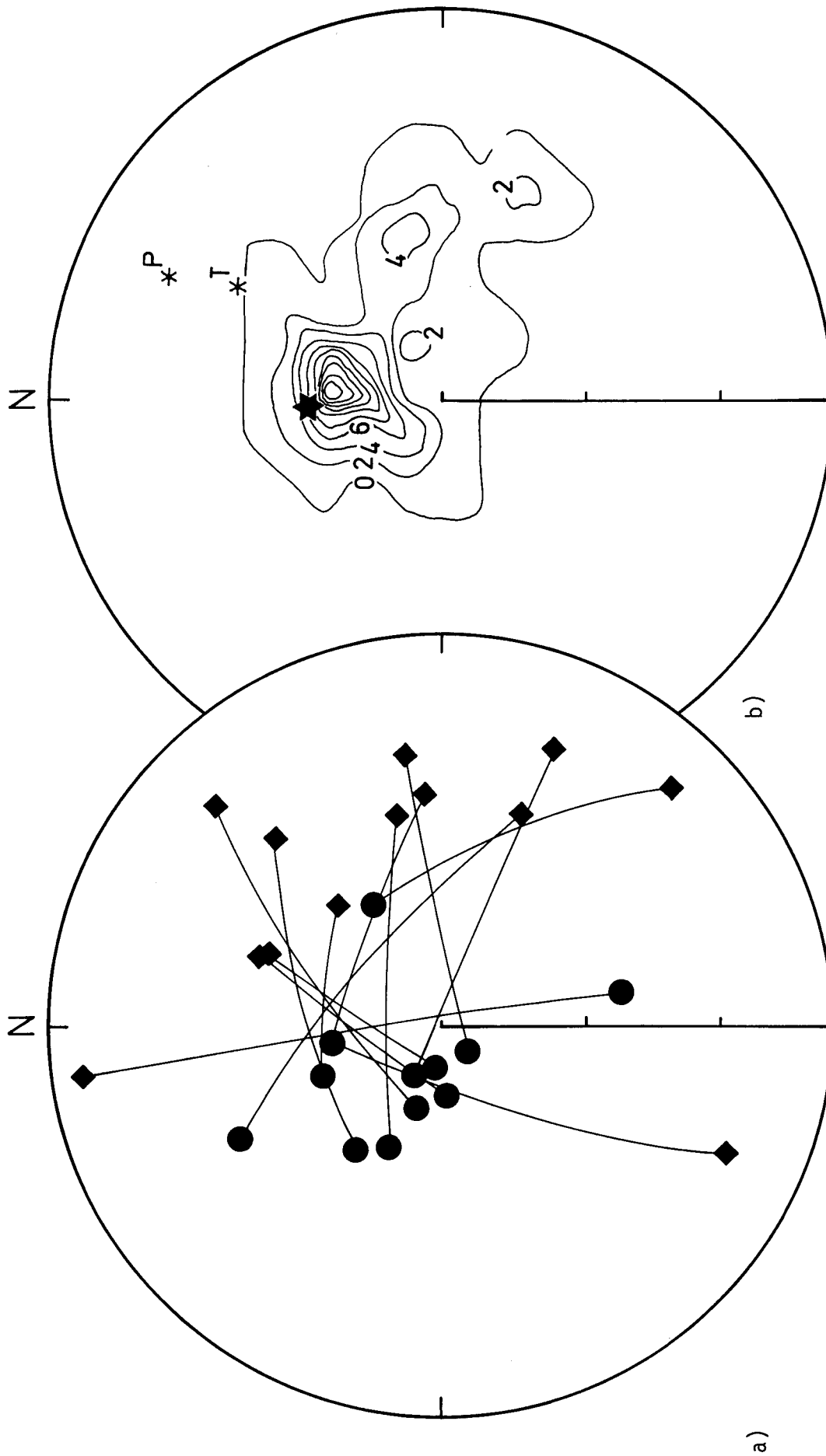
Figure 6.5. a) Directions of the ChRM (diamonds), minimum susceptibility axes (circles) and the corresponding great circles for the Lower Glarus Nappe complex. b) Equal area density plot of the great circle inter- sections. The star shows the earth's field direction and the asteriks show the predicted Permian (P) and Triassic (T) directions in the field area.

closer to the k_{min} axis directions (Figure 6.5). These directions lie co-incidentally near to the present and Tertiary field direction for the area.

Simple Shear Model for the Acquisition of ChRM Directions

The Maritime Alps studies (Kligfield et al., 1983; Cogné and Perroud, 1985; Lowrie et al., 1986) showed that as a result of increasing distortional strain in a rock, the scatter of the ChRM directions increases. The paleomagnetic vectors diverge from the expected direction to form a partial girdle about the trend of the regional fold axes. A similar phenomenon is observed in the Glarus red beds of the present study (Figure 6.4). The spread of the directional data cannot be explained by dispersion on small circles corresponding to rigid body rotation about local or regional fold axes which would arise from buckle folds. The resulting small circles shown in Figure 6.6 do not coincide with the dispersion of the paleomagnetic vectors.

A simple model to approximate the overall internal deformation in the study area is one of heterogeneous, horizontal simple shear. Northward motion on the Glarus overthrust during the Calanda phase of deformation develops asymmetric folds with flattening within the gentle south-dipping cleavage (Pfiffner, 1981). Figure 6.7a illustrates the paleomagnetic vector (DB) in an undeformed state; for this study it is a typical Permo-Triassic direction ($D = 26°$, $I = 31°$). DC is the horizontal projection of DB. If the block is deformed by simple shear on a horizontal shear plane with motion D to E, the point D will be displaced to D' while the point B remains fixed (Figure 6.7b). The remanence vector, if acting as a passive line element, has a new orientation defined by D'B. D'C is the new horizontal projection of D'B. Both α and ϕ will increase until $\alpha = 90°$. The angle ϕ has now reached a maximum value, and starts to decrease in value with further shear ($\alpha > 90°$).

Figure 6.7c illustrates that the same properties governing the behavior of α and ϕ during simple shear can also be shown on a great circle. The declination, α, increases with northward horizontal simple shear, and the inclination, ϕ, increases to a maximum value before decreasing. The great circle defines the path of increasing shear strain.

The model assumes a heterogeneous, horizontal simple shear and is only a crude approximation for the complexity of the deformation in the Lower Glarus Nappe complex. It also assumes that the hematite grains reorient in such a way that the remanence vectors rotate as passive line markers.
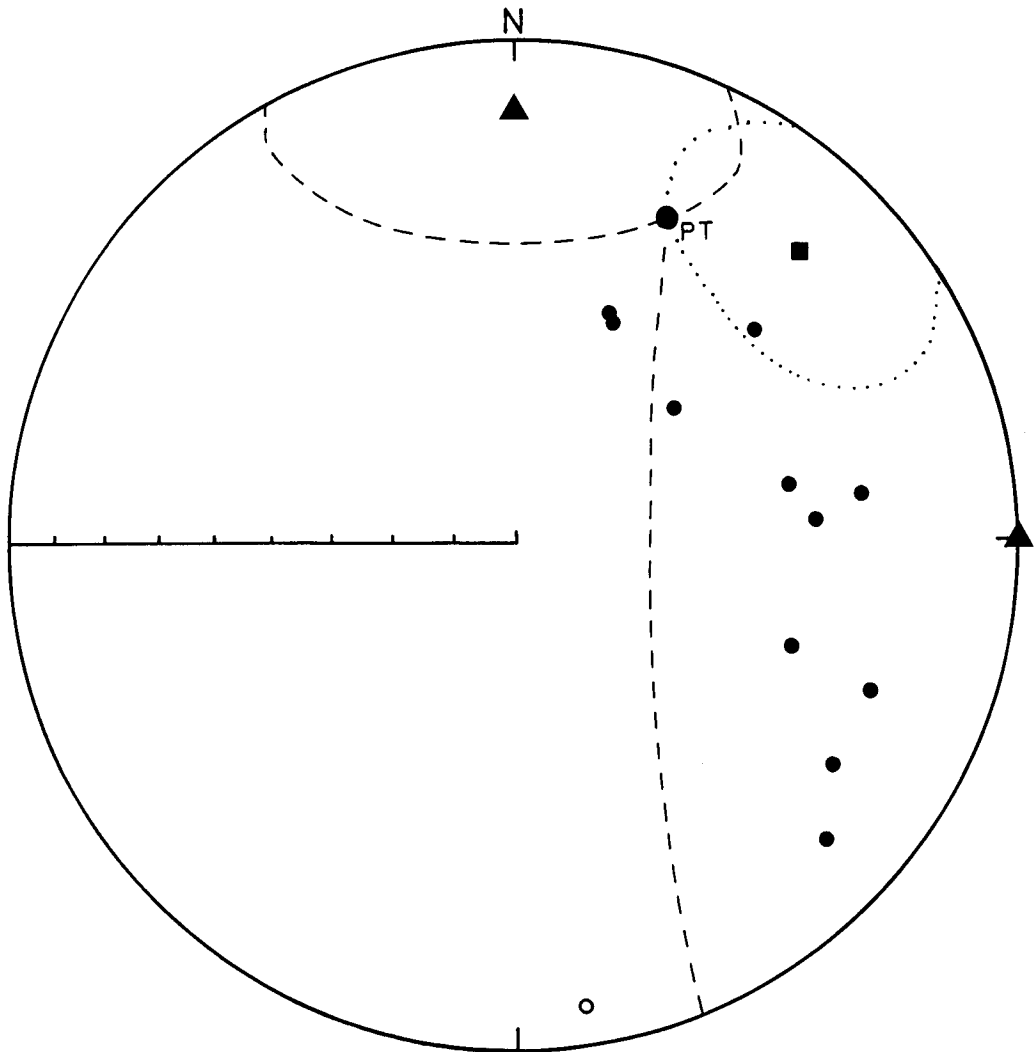
Figure 6.6. Small circle rotations about site fold axes which indicate the predicted dispersion of the ChRM directions if buckle folds were responsible. The triangles represent the poles to the main fold structures in the Lower Glarus Nappe complex, and the square represents the pole to the overall fold structure of the Helvetic Nappe pile.
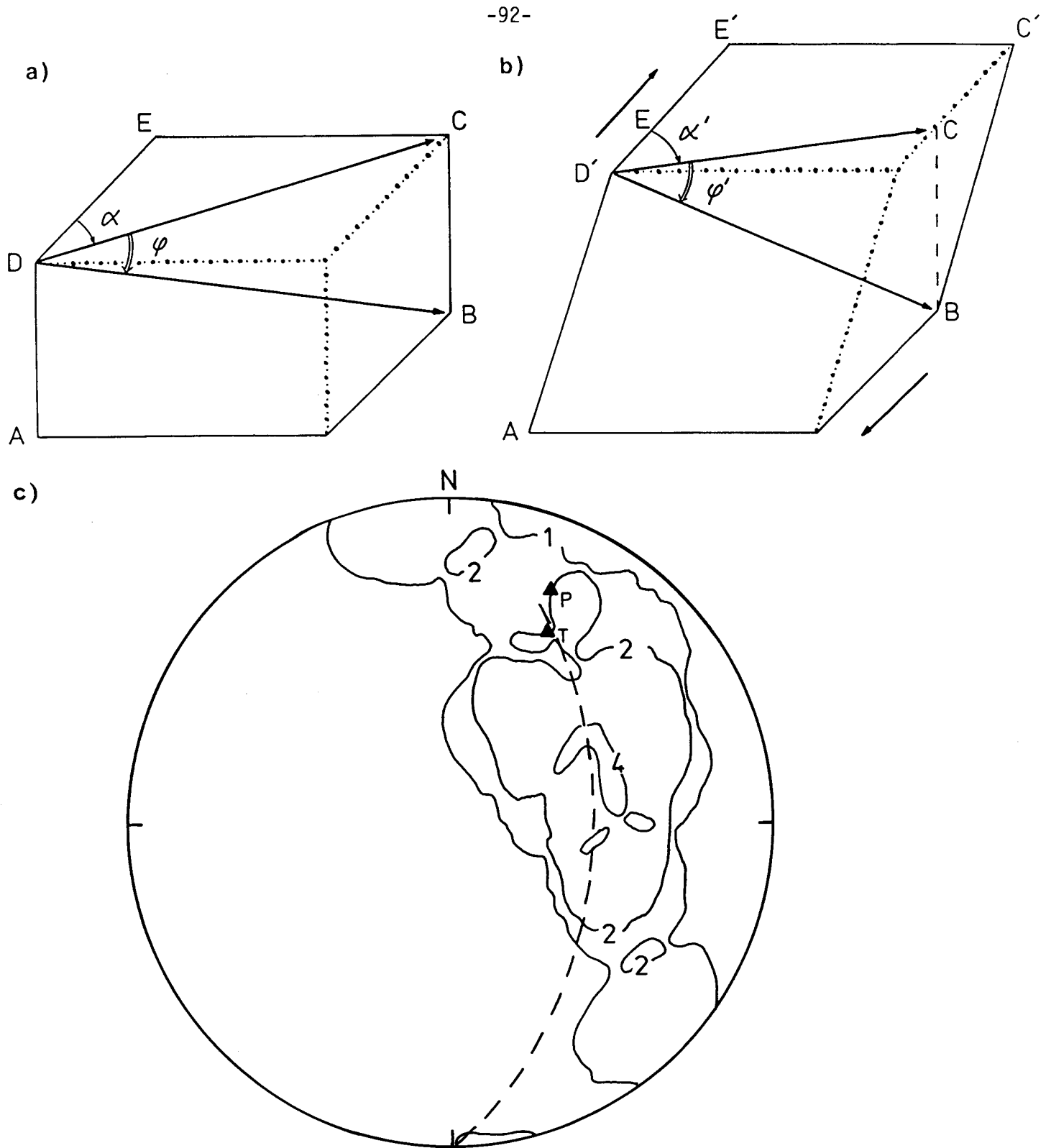
Figure 6.7. Structural deformation model for horizontal simple shear.
a) Block diagram before deformation; DB represents the remanence vector,
α is the declination and φ is the inclination. b) Block after undergoing
simple shear; D'B represents the deformed remanence vector, α' is the
declination after deformation and φ' is the inclination after deformation.
c) Equal area density plot showing dispersion of the remanence vectors
resulting from the deformation. The Permian and Triassic directions as
in Figure 6.4. The dashed line indicates the predicted dispersion of
remanence directions due to simple shear.

The behavior of hematite platelets, the carrier of the remanence, in penetrative deformation is not yet adequately understood. An alternative explanation is that the remanence is carried by hematite but that the AMS is carried by paramagentic minerals. As stated in Chapter 5, a separation of the hematite from the paramagnetic component of the anisotropy was not possible.

The measured ChRM directions do in fact appear to be distributed along a great circle as predicted by the simple shear model. However, the model predicts that ChRM directions should deviate furthest from the Permo-Triassic direction where the simple shear strain is the highest. In fact, strain values from the corresponding finite strain ellipsoid for each site projected on a N-S plane, do not vary systematically in such a way along the great circle (Figure 6.8).

6.5 Conclusions

Although the simple shear model is compatible with the observed directional distribution, and suggests that a systematic mechanism was responsible for the dispersion of the ChRM directions in these highly strained red beds, the actual and derived strain data underline the preliminary nature of the model and indicate that it is quantitatively inadequate. It can be be calculated for a three-dimensional simple shear model that an axial ratio for the strain ellipsoid of 2.1 (X/Z) would be necessary to cause the Permo-Triassic direction to be displaced to the ϕ position (071/50) where the inclination is maximum. The predicted maximum inclination (ϕ) for the model ($\phi = 54°$) would require a strain ellipsoid with an axial ratio of 2.5. These strains are much lower than the average axial ratios (6.8) found in the Lower Glarus Nappe complex. However, this average value assumes that the reduction spots are initially spherical. The initial shape of the spots before the deformation is not known, and it may well be oblate, i.e., X/Z greater than 1, due to sedimentary compaction. Since bedding and cleavage are both relatively flat, superposition of the strain ellipsoid over a bedding-flattened ellipsoid would result in a total ellipsoid which overestimates the shear strain.
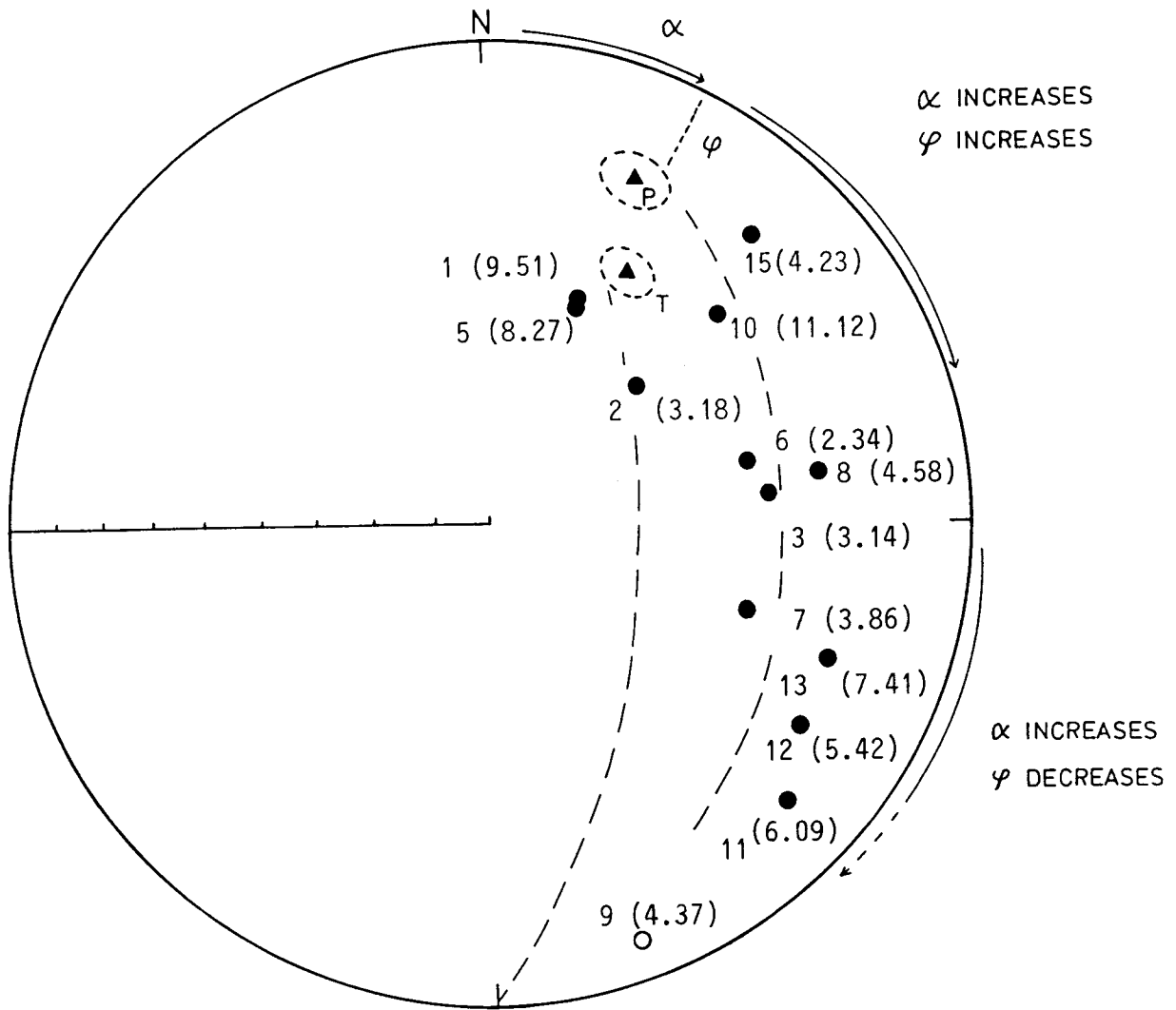
Figure 6.8. ChRM directions plotted on the lower hemisphere except for the very flat direction at site GV9. The two dashed great circles represent the envelope of expected dispersions of Permian and Triassic directions due to N-S simple shear. Numbers in parentheses are the finite strain values on a north-south plane at each numbered site (Chapter 5, Table 5.2 and 5.3).

Chapter 7. THE ANISOTROPY OF MAGNETIC SUSCEPTIBILITY AS A STRAIN INDICATOR IN THE SUDBURY BASIN, ONTARIO

7.1 Introduction

The origin of the Sudbury basin in the Canadian Shield has long been intensely debated. The basin was originally considered to be of volcanic origin, and was thought to be either a composite, ring-dike intrusive of norite and micropegmatite, or a lopolith with an ultramafic mass at depth (Card and Hutchinson, 1972). The Onaping breccia which overlies the Irruptive was considered to have resulted from explosive volcanic events or from diatreme activity associated with the intrusion of gabbros south of the basin (Stevenson, 1972).

Dietz (1962, 1964) proposed a radically different origin for the basin: that it was formed by a meteoritic impact. This idea was supported by the presence of shatter cones around the outside of the basin, which were believed to have been formed from the shock waves emanating from the impact. The later discovery of shock metamorphic features in rock fragments of the Onaping formation, which is proposed to be a fall-back breccia, and in the footwall rocks adjacent to the Irruptive supported an extraterrestrial origin for the basin (French, 1972). Brocoum and Dalziel (1974) maintained that strain analysis of rock and mineral fragments in the Onaping breccia and of concretions in the Chelmsford formation support the idea that the basin was originally circular.

There has been considerable opposition to interpreting the basin as an astrobleme (Card and Hutchinson, 1972), the strongest argument being the present shape of the basin itself. Several geologic features suggest that the pre-deformational shape of the basin must have been originally elliptical. These include:

1) the north rim of the basin is undeformed, and presumably reflects the curvature of the original basin; therefore the pre-deformational shape of the basin would have to extend over 110 km south of Sudbury (Rousell, 1972);

2) paleocurrent directions in the Chelmsford formation are predominantly west-southwest, parallel to the long axis of the basin, which suggests an elongated trough at the time of deposition (Cantin and Walker, 1972; Rousell, 1984a);

3) additional strain analysis on individual fragments in the Onaping breccia shows considerable and inconsistent strain variation, so that the fragments characterize only the local strain fields (Rousell, 1975).

The pre-deformational shape of the basin is at present unknown. With new three-dimensional strain analysis techniques it should be possible to estimate the strain within the basin so that the effects of the strain can be compensated for and the original shape of the basin can be estimated. Concretions within the Chelmsford formation provide strain markers for the central part of the basin. Rousell (1984b) considered the deformation of the concretions to be variable. However, Brocoum and Dalziel (1974) analyzed the finite strain defined by the concretions and suggested that they had been flattened in the foliation and were originally spherical. They claimed that the Chelmsford concretions were shortened 30% normal to the cleavage and extended 10% subhorizontally and 40% subvertically within the plane of cleavage. Unfortunately no detailed strain measurements were provided for individual sites.

The concretions occur in only 26% of the outcrops of the Chelmsford formation in the basin, and therefore do not provide enough information on the finite strain for the entire formation. Kligfield et al. (1977) measured the AMS at eighteen sites within the Chelmsford formation, three sites within the Onaping formation and seven sites in the norite in the Sudbury basin. The k_{max} and k_{int} directions defined a magnetic foliation plane which was subparallel to planar structural elements of the basin, and the k_{max} directions described a magnetic lineation which was subparallel to the mineral elongation in the rocks. The authors noted that the susceptibility magnitude ellipsoid varied systematically across the basin. Although the AMS appeared to accurately reflect the finite strain, the limited amount of data did not allow for a direct comparison of the finite strain and AMS.

An attempt to correlate the finite strain and AMS has been made in order that an equivalent strain value could be derived for areas that do not contain concretions. Increased coverage of strain information within the Chelmsford formation is necessary for future models to restore the original shape of the basin by removal of the effects of strain.

7.2 Geology

The Sudbury basin is located in the Southern province of the Canadian Shield at its junction with the Superior and Grenville provinces (Figure 7.1a). The present shape of the basin is elliptical and it extends approximately 60 km in an east-northeast direction and approximately 27 km across. The basin is outlined by the Nickel Irruptive which consists of a lower gabbroic layer, known as the norite, and an upper granitoid or micropegmatite layer. A transition zone of gabbroic quartz exists between the norite and micropegmatite (Naldrett et al., 1970). The Irruptive forms the topographic high ranges surrounding the basin. The northern lower contact of the Irruptive dips 30° to 50° to the south and the southern contact dips 45° to 70° to the north, although it can be locally vertical or overturned.

The inner basin is filled by the Whitewater Group and consists of the Onaping formation at the base, the Onwatin formation and the Chelmsford formation. The Onaping formation is a complex layered breccia made up of four major units. It has been interpreted alternatively as an ash flow (Stevenson, 1972) or as the fallback of a meteorite impact (French, 1967; Peredery, 1972). The true origin of the breccia is still under debate, and the breccia has an estimated thickness of up to 1600m (Muir and Peredery, 1984). The Onaping breccia has a gradational contact with the overlying Onwatin formation, which is a carbonaceous, pyrite-rich argillite-siltstone. The Onwatin formation is poorly exposed but has an estimated thickness of 600m, and it represents pelagic sediments deposited in a deep, restricted basin (Rousell, 1984b).

The upper member of the Whitewater Group, the Chelmsford formation, has a gradational contact with the Onwatin formation and consists of repetitive sequences of a) greywacke, b) argillite and siltstone, c) graded sandstone, and d) laminated siltstone and argillite. Its present thickness is approximately 850m but due to erosion it may have been originally thicker and more extensive (Rousell, 1984a). The formation has been described as a proximal turbidite in which many original sedimentary structures are preserved (Cantin and Walker, 1972; Rousell, 1972). Indicators of preserved paleocurrents are oriented predominantly to the southwest along the long axis of the basin, which suggests that the basin was already elongate at the time of deposition of the Chelmsford formation. Ellipsoidal concretions (major axes X > Y > Z) are found in 26% of the beds and differ from the matrix in composition in their higher calcium carbonate

and slightly higher iron content. Since the foliation passes through the concretions without deviating, their rheologic properties probably reflect those of the rock as a whole. In general, the concretions are flattened in the cleavage (Brocoum and Dalziel, 1974; Kligfield et al., 1977).

The overall structure of the Whitewater Group is one of a doubly plunging synclinorium confined by the Sudbury Irruptive. The strata of the group are gently folded about axes parallel to the long axis of the basin. The folds are gently plunging in both directions. Faults cut both the Whitewater Group and the older rocks and these trend northeast to east-northeast. In the northern part of the basin there are a series of faults which trend north-northwest and dip steeply (Figure 7.1a).

Deformation varies across the width of the basin. A penetrative cleavage is well-developed in the southeast. There is a steeply dipping mineral elongation within the cleavage plane of the Onaping formation (Brocoum and Dalziel, 1974; Rousell, 1975, 1984b) and intensive flow banding and fluidal textures are present (Muir and Peredery, 1984). Cleavage is less well-developed or absent in the northwestern part of the basin. The Chelmsford formation has been folded in open, concentric folds with axial planar cleavage. The cleavage is a penetrative, pressure solution cleavage in which mineral grains have been flattened by pressure dissolution on their boundaries. Insoluable residue is concentrated along these boundaries and is of variable thickness (Clendenen, 1986).

The Sudbury Irruptive has been radiometrically dated at approximately 1850 Ma (Krogh et al., 1984; Faggart et al., 1985). Deformation occurred shortly afterwards during the Penokean orogeny at 1750 Ma (Krogh et al., 1984). Rousell (1984a) speculated that deformation of the basin may have occurred during the deposition of the Chelmsford formation.

7.3 Sampling and Magnetic Mineralogy

Sampling

A total of sixteen sites were collected in the Chelmsford formation and twenty sites in the Onaping formation (Figure 7.1b). The locations of the sampling sites were limited by the outcrop exposure. Between nine and fifteen samples (yielding 24 to 42 specimens) were drilled at each site in the Chelmsford formation. Concretions were found at ten sites and at these sites at least three of the samples were taken from the concretions. Axial ratios and orientations of the concretions were measured on at least
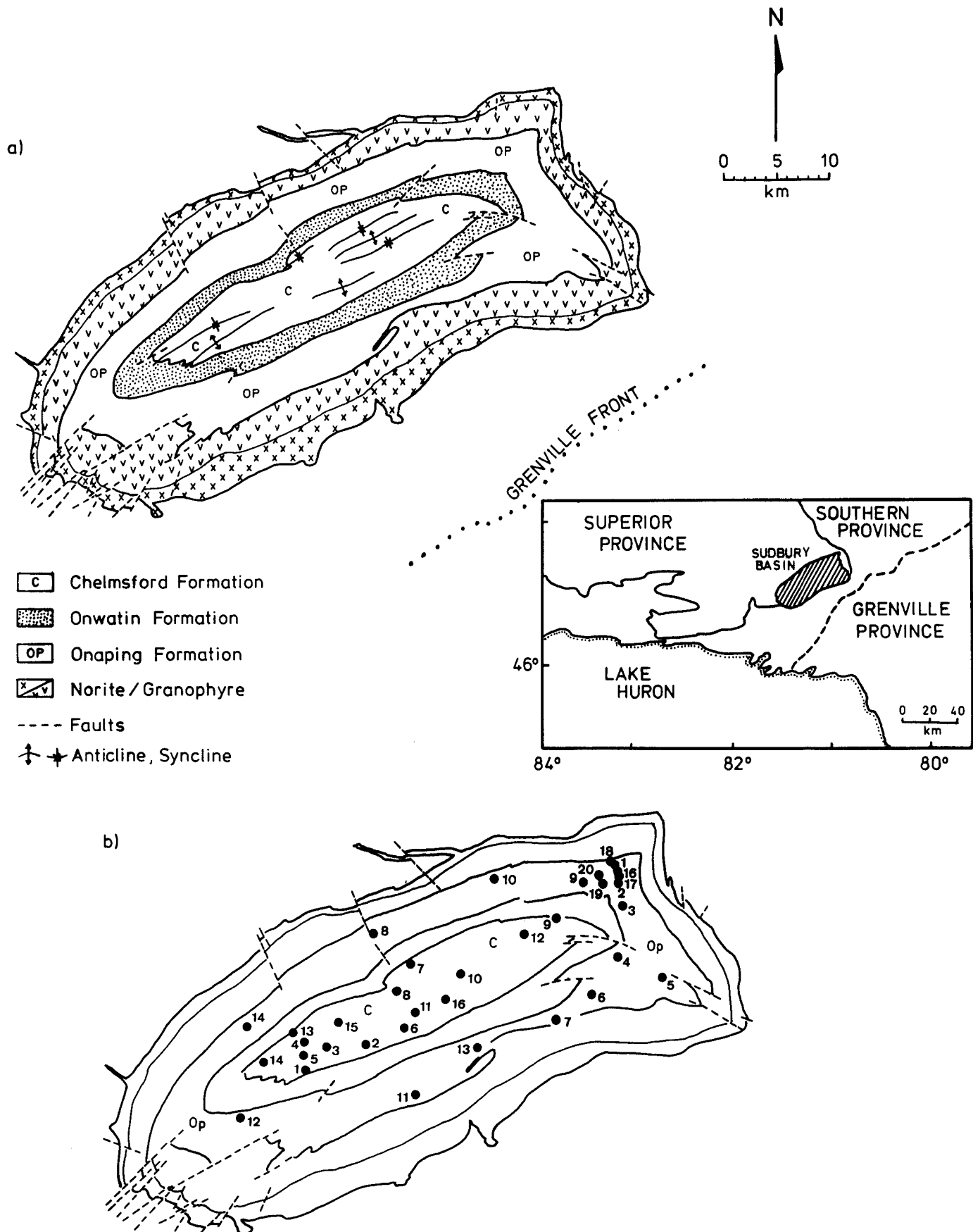
Figure 7.1. a) Generalized geologic map, and b) Site location map.

three surfaces per site. Only concretions with well-defined elliptical cross-sections were used for the strain analysis (which was done by W. Clendenen at the University of Colorado, Boulder). Microfabric analysis was also done on thin sections cut on three mutually perpendicular surfaces from at least one core from each site, in order that the strain of the quartz grains in the Chelmsford sandstones could be determined. The microfabric strain analysis was done using the Frey Method (Clendenen, 1986).

In the Onaping formation one main profile was sampled along the eastern margin of the basin in order to observe the progressive change in deformation from the north range to the south range. Additional sites were taken along the little deformed northern limb and the more deformed southern limb of the basin (Figure 7.1b). Between nine and seventeen samples (yielding 24 to 45 specimens) were taken at each site.

Magnetic mineralogy of the Chelmsford formation

The curve of IRM acquisition shows a change in shape after the first field of 0.016T and again at 0.08T. Saturation of the IRM occurs between 0.5T and 0.6T (Figure 7.2a). Demagnetization by application of direct magnetic fields antiparallel to the IRM shows two linear segments. The first phase shows a rapid drop of the magnetization until -0.04T, with an extrapolated, coercivity of remanence (H_{cr}) of -0.06T. The second phase has a shallower slope and the corresponding H_{cr} is between -0.09T and -0.12T (Figure 7.2a). The behavior of the IRM acquisition and reverse field demagnetization is the same for the matrix and the concretions.

A 1.0T field was applied along the cylinder (z) axis of the specimens and then a 0.1T field was applied along the sample x-axis, perpendicular to the first component. Thermal demagnetization of the saturation IRM shows a 30% drop in intensity between 150°C and 250°C followed by another large drop in the magnetization between 330°C and 360°C (Figure 7.2b). The vector plot shows the decay of a vector component, the direction of which initially results from both the high and low coercivity components (Figure 7.2b). After 360°C the magnetization decays gradually until 520°C along the x-axis of the plot, which indicates only the presence of lower coercivity material in this high temperature range. The combination of IRM acquisition, reverse field demagnetization and thermal demagnetization suggests that pyrrhotite is probably responsible for the higher coercivity,

a)

CM6.13
$M_m = 9.08 \times 10^{-2} A/m$

b)

Figure 7.2. a) Acquisition of IRM and reverse field demagnetization of a representative sample from the Chelmsford formation. b) Normalized intensity plot showing the intensity variation and vector diagram showing directional behavior during thermal demagnetization. Closed (open) symbols represent vector end points projected on the horizontal (vertical) plane for this and subsequent figures.
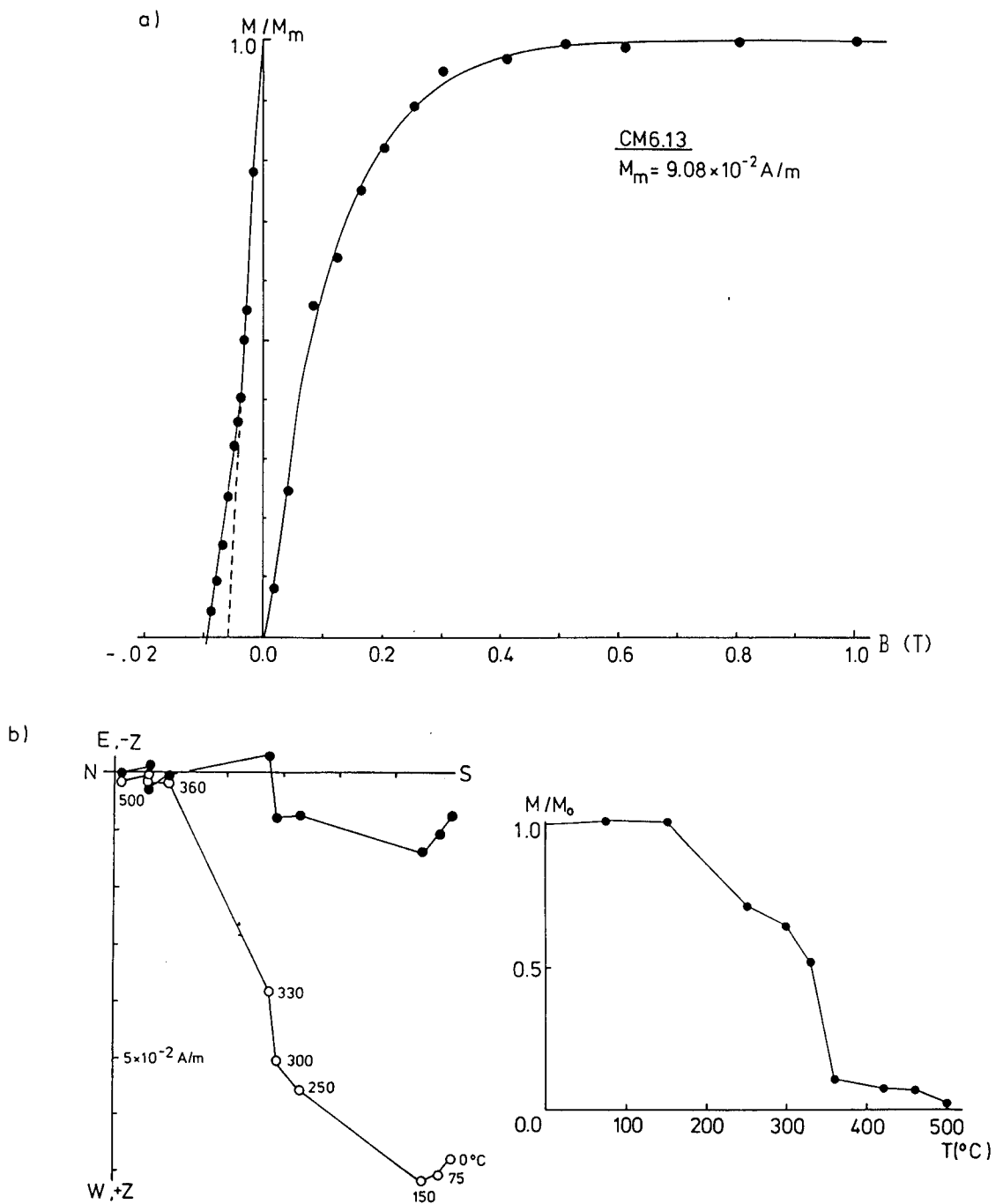
low temperature component of the magnetization and magnetite with low titanium content for the lower coercivity, high temperature component.

Magnetic mineralogy of the Onaping formation

The Onaping specimens are not as uniform in their magnetic mineralogy as those of the Chelmsford formation but can be classified into two broad groups. The first group is characterized by a dominant low coercivity component of magnetization in the acquisition of IRM. Saturation occurs in most samples around 0.2T, although some samples may also show a slight increase of the IRM until 0.4T after which they are saturated. Reverse field demagnetization reveals a single coercivity of remanence between -0.013 and -0.020T (Figure 7.3a). After applying a 1.0T field along the specimen's z-axis and and a 0.1T field along the specimen's x-axis, the samples were thermally demagnetized. The magnetization of the specimens decreases rapidly between 200°C and 250°C and the specimens are completely demagnetized by 360°C (Figure 7.3b). The effect of both coercivity components is seen in the vector decay (Figure 7.3b). The IRM acquisition curves after heating the specimens remains similar in shape as before thermal demagnetization (Figure 7.4). Although saturation occurs in fields as low as 0.2T, the thermal demagnetization behavior of the specimens suggests that pyrrhotite is the only magnetic mineral present in these specimens.

Rock magnetic analysis of the second group indicates the presence of at least two and possibly three magnetic minerals. IRM acquisition curves show a kink in the shape of the curve at 0.08T and the specimens are not saturated by 1.0T. Reverse field demagnetization is made up of two linear segments, one with H_{cr} of approximately -0.030T and a second with H_{cr} approximately -0.045T (Figure 7.5a). Thermal demagnetization of the specimens magnetized in a 1.0T field along their z-axis and a 0.1T field along their x-axis shows the presence of the combined coercivity component until 360°C, where the magnetization is reduced by approximately 80%. At this stage a component probably carried by pyrrhotite has been demagnetized. The remaining 20% of the magnetization gradually decays until 520°C and is dominated by the low coercivity component of magnetization which can be associated with magnetite (Figure 7.5b). Thus, like the Chelmsford specimens the second group of rocks of the Onaping formation have magnetic properties determined by both magnetite and pyrrhotite. The IRM acquisition curves after thermal demagnetization

a) Acquisition of IRM and reverse field demagnetization, with axes M/Mm vs B(T), annotated $M_m = 1.36 \times 10^2$ A/m, $H_{cr} = 0.017$ T

Vector diagram labeled SO 6.6 with axes Z, X, -X, Y.-Z, -Y.Z, annotations IRM, 200°C, 300, 400

b) Normalized intensity plot M/Mm vs T(°C)
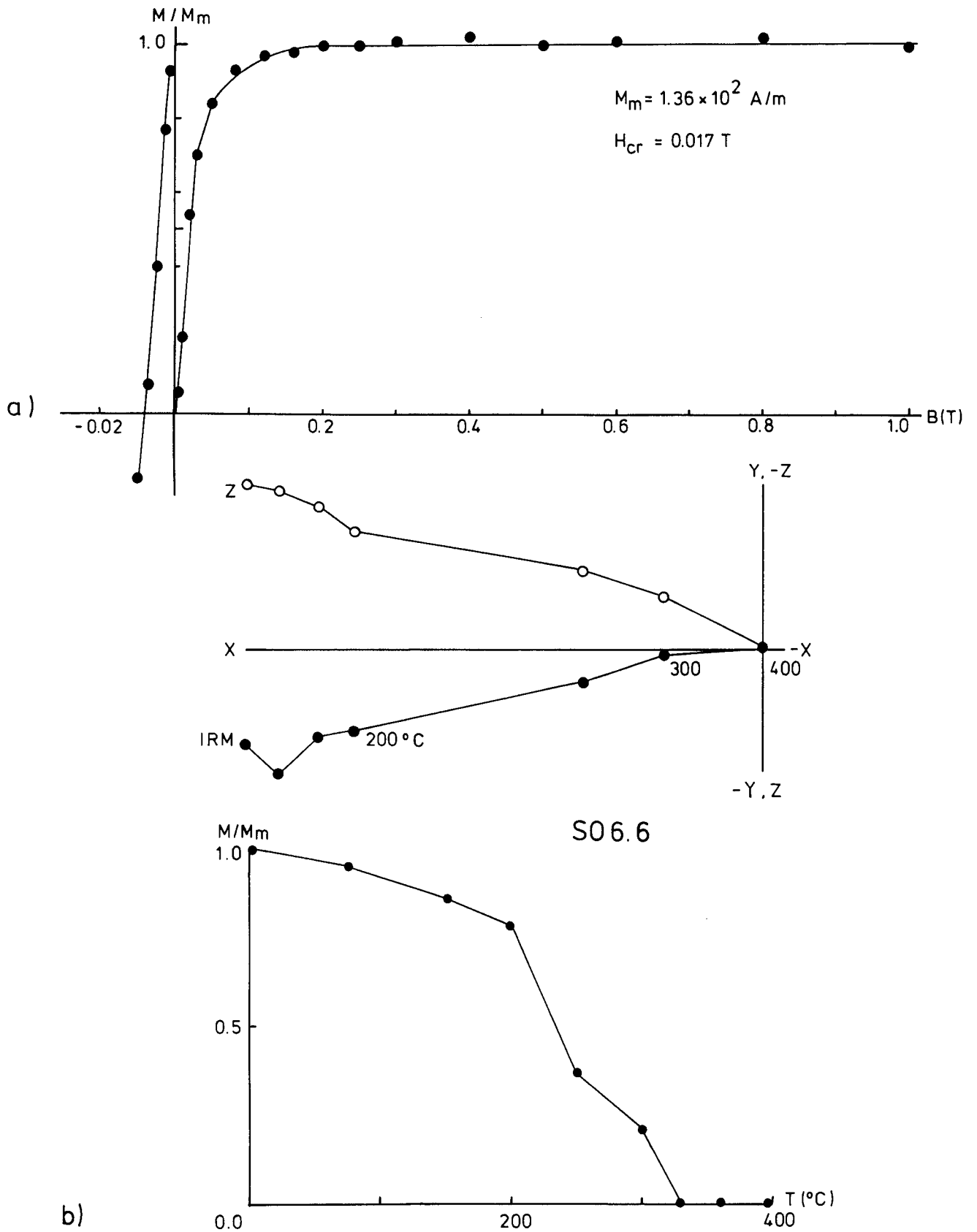
Figure 7.3. a) Acquisition of IRM and reverse field demagnetization of a representative sample from the Onaping formation which possesses one magnetic mineral. b) Normalized intensity plot showing the intensity variation and vector diagram showing directional behavior during thermal demagnetization.

SO 6.6

$$M_m = 1.86 \times 10^2 \, A/m$$
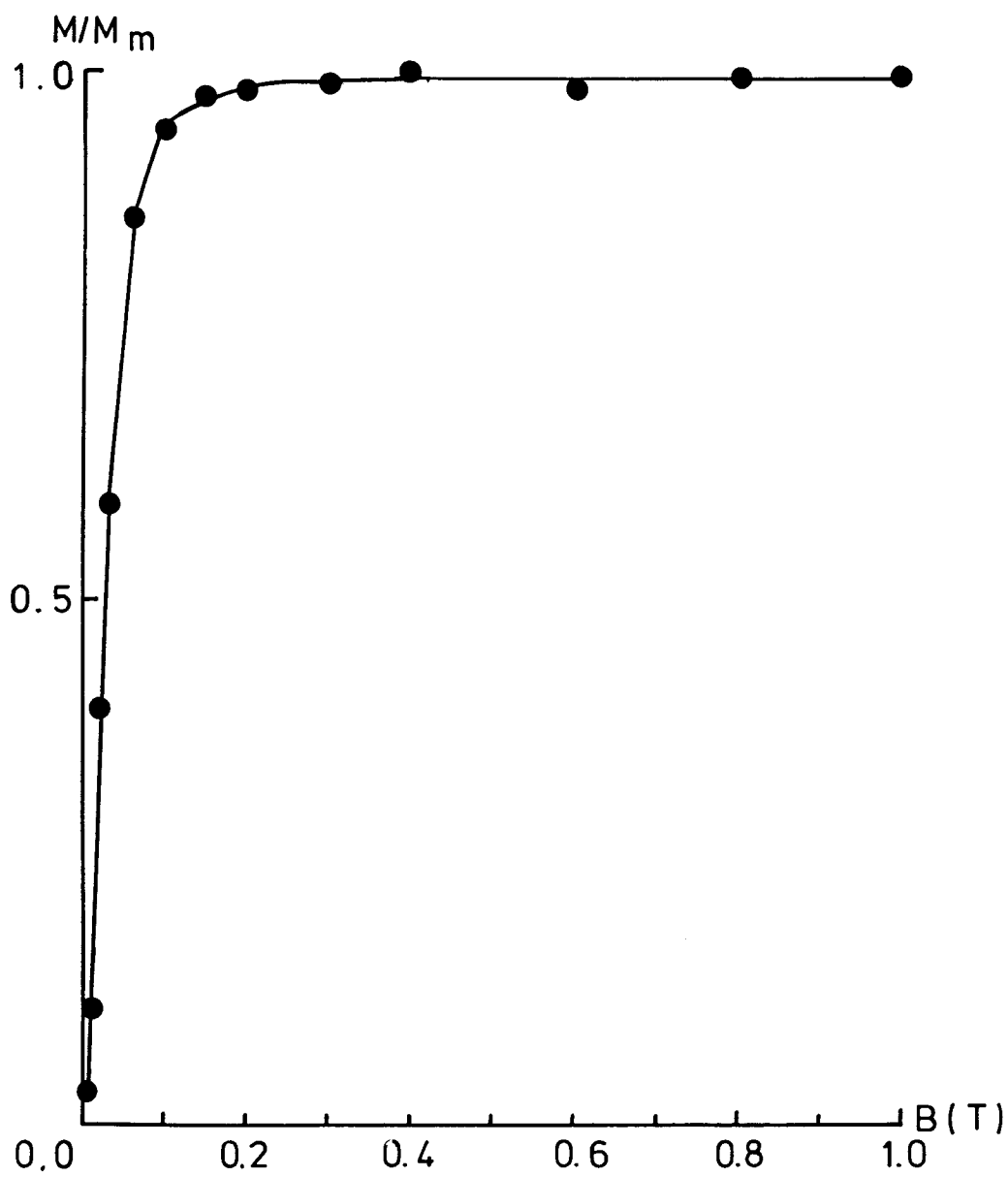
Figure 7.4. Acquisition of IRM of a specimen which possesses one magnetic mineral after thermal demagnetization.
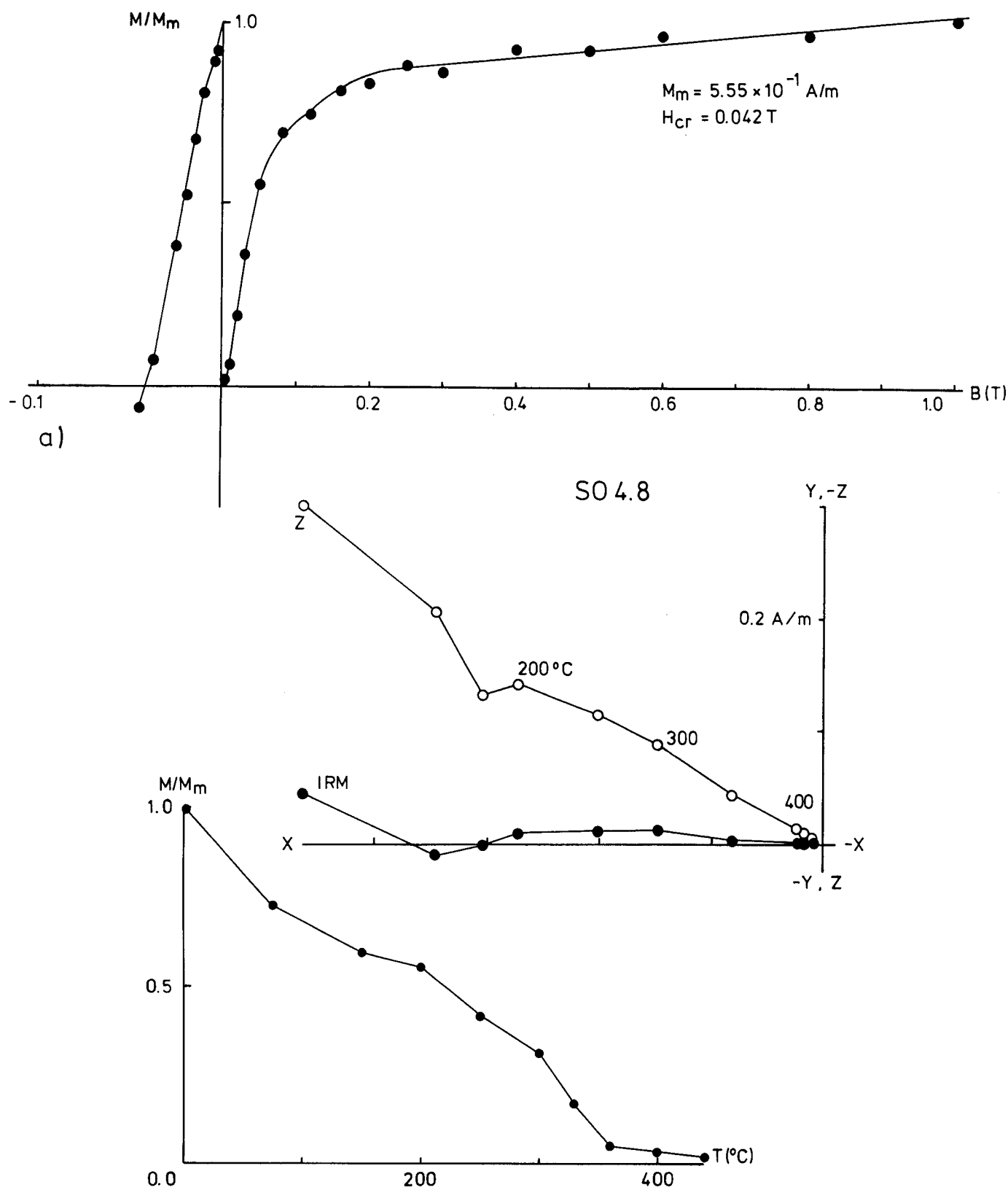
Figure 7.5. a) Acquisition of IRM and reverse field demagnetization of a representative sample from the Onaping formation which possesses more than one magnetic mineral. b) Normalized intensity plot showing the intensity variation and vector diagram showing directional behavior during thermal demagnetization.
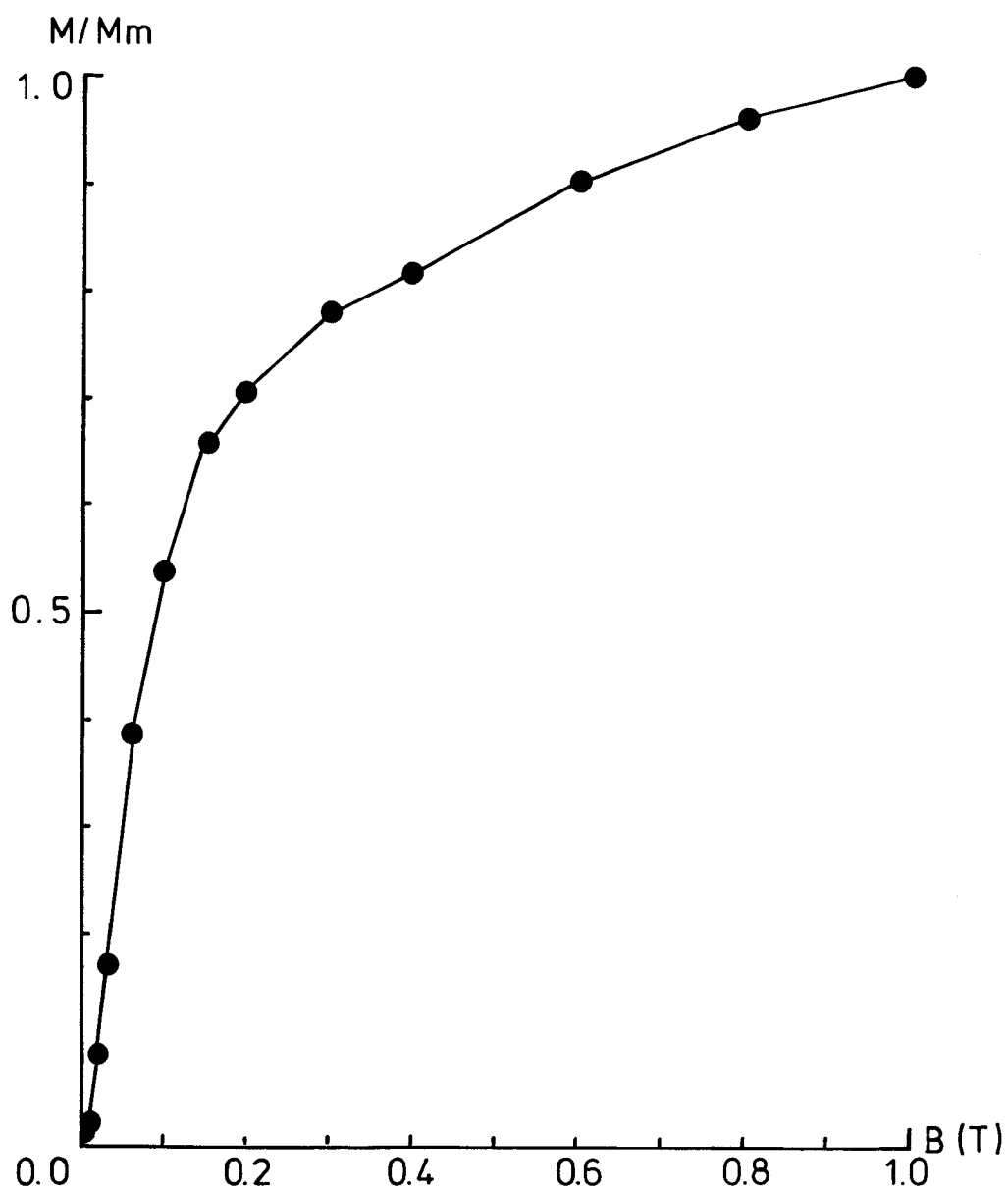
Figure 7.6.   Acquisition of IRM of specimen which possesses more   than one magnetic mineral after thermal demagnetization.

are similar to those before heating, indicating that the magnetic mineralogy is thermodynamically stable (Figure 7.6). The fact that the IRM curves do not saturate by 1.0T may indicate that a high coercivity mineral, such as, hematite may also be present in small quantities.

Pyrrhotite and low titanium magnetite are probably mainly responsible for the AMS in the Chelmsford and the Onaping rocks. Magnetite is governed by a shape anisotropy, and pyrrhotite is governed mainly by a magnetocrystalline anisotropy, with the magnetization controlled to lie in the basal planes within which the grains may also possess a shape-dependent anisotropy. The paramagnetic minerals may also contribute to the susceptibility anisotropy in these rocks.

7.4 Results

Chelmsford Formation

The magnetic fabric of the Chelmsford formation is controlled by the cleavage in fourteen of the sixteen sites. Site CM13 and CM14, whose fabrics are not controlled by the cleavage, are located in the northwest end of the basin. Site CM13 consists of two groups of samples, those controlled by the bedding and those controlled by the cleavage. These samples will be further considered as two separate sites that will be labeled CM13B for the bedding controlled fabric and CM13C for the cleavage controlled fabric. Site CM14 possesses a triaxial anisotropy ellipsoid but does not appear to be controlled either by bedding or cleavage. The magnetic fabric is anomalous and will be excluded from further analysis, because it is uncertain that the glacially scoured outcrop is in situ.

The k_{min} axes are subnormal to the plane of cleavage and the k_{max} and k_{int} axes lie within the cleavage plane (Figure 7.7). These maximum and intermediate axes are girdled within the cleavage or separated in tight groups. As seen by Kligfield et al. (1977) the susceptibility magnitude ellipsoid for individual specimens at a site may vary from prolate ($k_{int} \simeq k_{min}$) to oblate ($k_{max} \simeq k_{int}$) in shape. However, the shape of the site mean ellipsoids are mainly oblate (Figure 7.8).

Figure 7.9 illustrates the magnetic foliation planes for the Chelmsford formation on a map plan and Table C.1 (Appendix C) lists the intensities and directions of the susceptibility magnitude ellipsoids for individual site means. The magnetic foliation is sub-parallel to the long axis of the basin and, in general, steeply dipping.

CHELMSFORD FM. SITE MEANS
AFTER CORE & CLEAVAGE CORRECTIONS

Number of
samples: 17

■ maximum
▲ intermediate
● minimum

CHELMSFORD FM. SITE MEANS
IN GEOGRAPHIC COORDINATES

Number of
samples: 17

■ maximum
▲ intermediate
● minimum
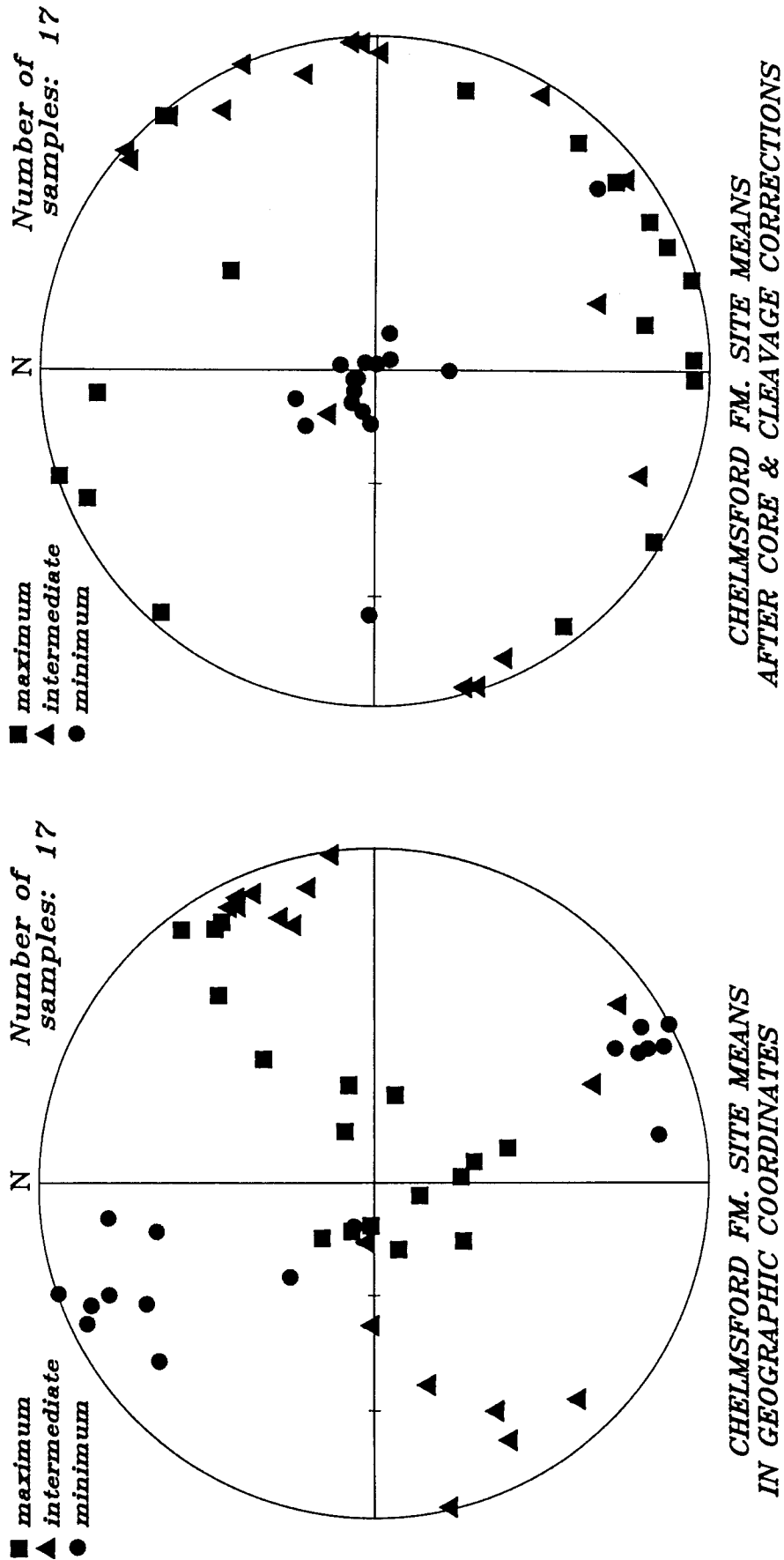
Figure 7.7. Equal area plots of the principal axes of the susceptibility magnitude ellipsoid for the site means of the Chelmsford formation on a lower hemisphere projection for this and subsequent figures.
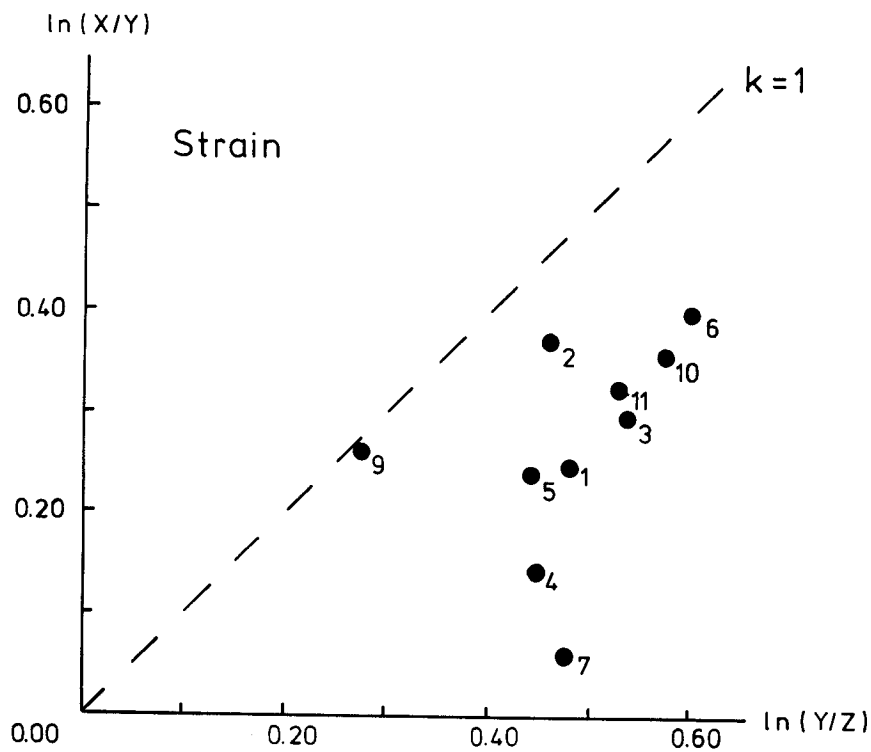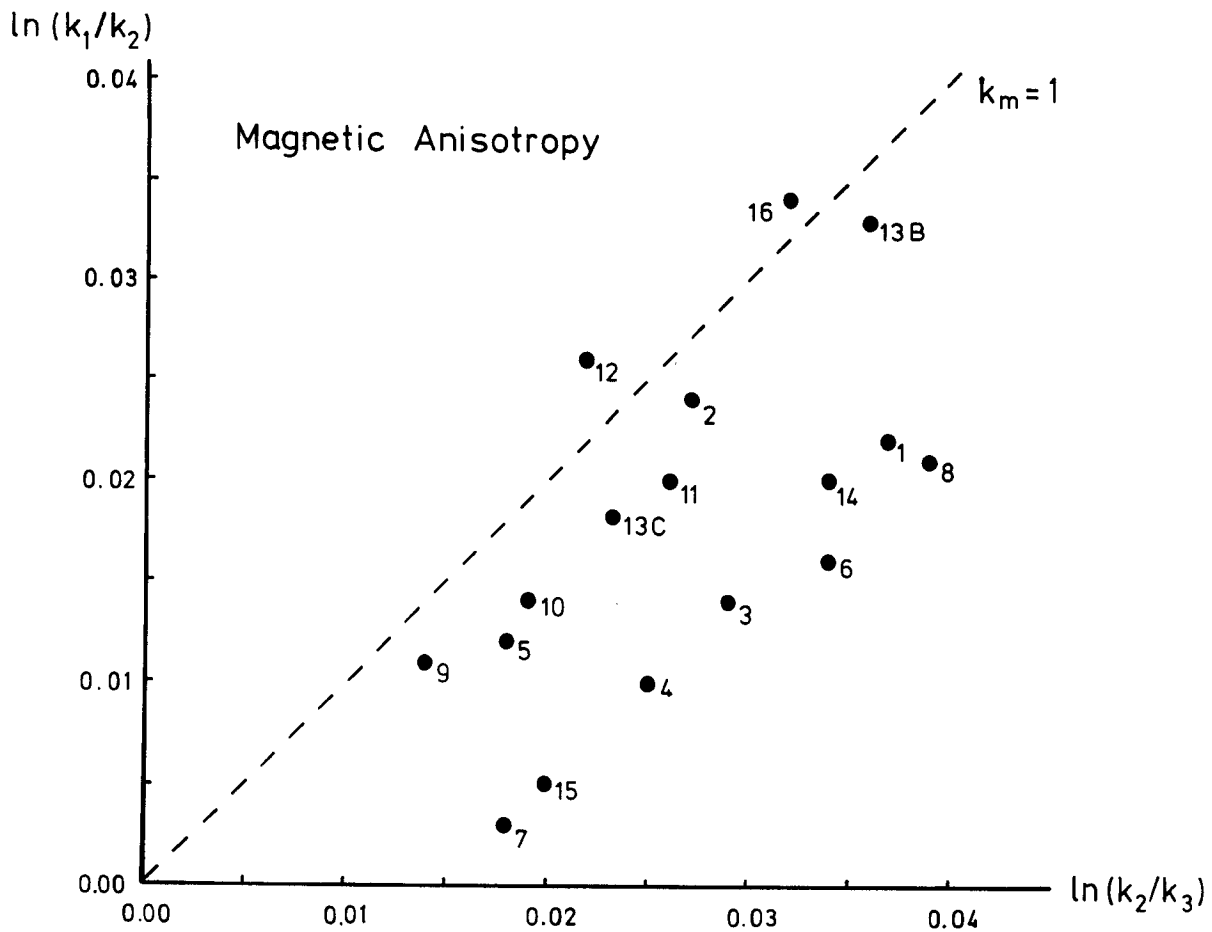
Figure 7.8. Logarithmic plot for the finite strain and an equivalent plot for the susceptibility magnitude ellipsoids of the site means of the Chelmsford formation.

The finite strain was derived for ten sites from concretions in the Chelmsford formation. The R_f/ϕ technique (Ramsay, 1967; Dunnet, 1969; Dunnet and Siddans, 1971) was employed to define the two-dimensional finite strain of the concretions. The results of the strain analysis are given in Table C.2 (Appendix C). The orientations of the principal axes of both the finite strain and the susceptibility magnitude ellipsoids are in good agreement (Figure 7.10). As seen with the AMS, the finite strain shows the X and Y axes lying within the plane of cleavage where this plane is oriented subparallel to the long axis of the basin. The X-axes tend to lie down-dip in the cleavage. The Z-axes are subhorizontal and sub-parallel to the short axes of the basin.

The lengths of the principal axes of the strain and the anisotropy ellipsoids can be correlated by the first four methods outlined in Chapter 5.3, where Method 1 is a direct correlation of the lengths of the principal axes of the strain and anisotropy ellipsoids; Method 2 is a correlation of the ratios of the principal axes; Method 3 is the log correlation of the individual principal axes; and Method 4 is the log correlation of the principal axes of all three groups together. The susceptibility magnitude ellipsoids were sectioned parallel to the principal planes of the strain ellipsoid, and the lengths of the axes in these elliptical sections were then used to correlate the magnitude ellipsoid with the strain ellipsoid. The principal axes of site CM4 varied by more than 30° from the strain ellipsoid, so the site was excluded from further analysis.

A linear fit was defined for the four correlation methods, in which a first-order regression with bi-square weighting was used. The results are listed in Table 7.1.

Onaping Formation

The magnetic fabric of the Onaping formation is more variable than that in the Chelmsford formation. The degree of deformation decreases towards the northwest corner of the basin, where it is completely absent. Table C.3 (Appendix C) lists the AMS data for the Onaping sites. Strongly deformed sites located along the southern and eastern ranges possess a magnetic fabric defined by a triaxial ellipsoid, where each group of axes is tightly grouped. The k_{min} axes are normal to the cleavage plane and the k_{max} and k_{int} axes lie within the plane of cleavage (Figure 7.11a). Less deformed sites show a change across the basin from the well-defined triaxial susceptibility magnitude ellipsoids in the southeast to a fabric in
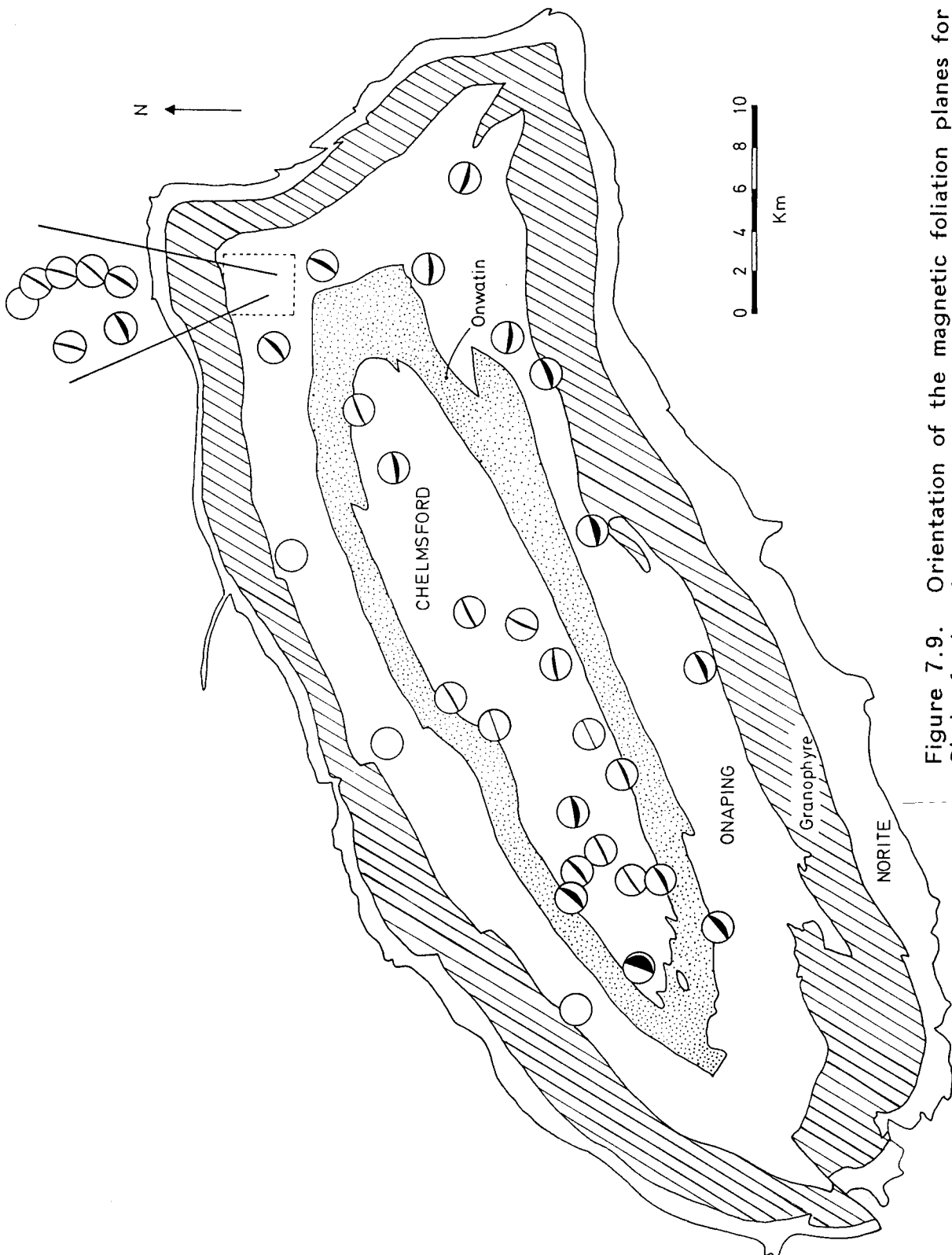
Figure 7.9. Orientation of the magnetic foliation planes for sites in the Chelmsford and Onaping formations shown on equal area, lower hemisphere projections.
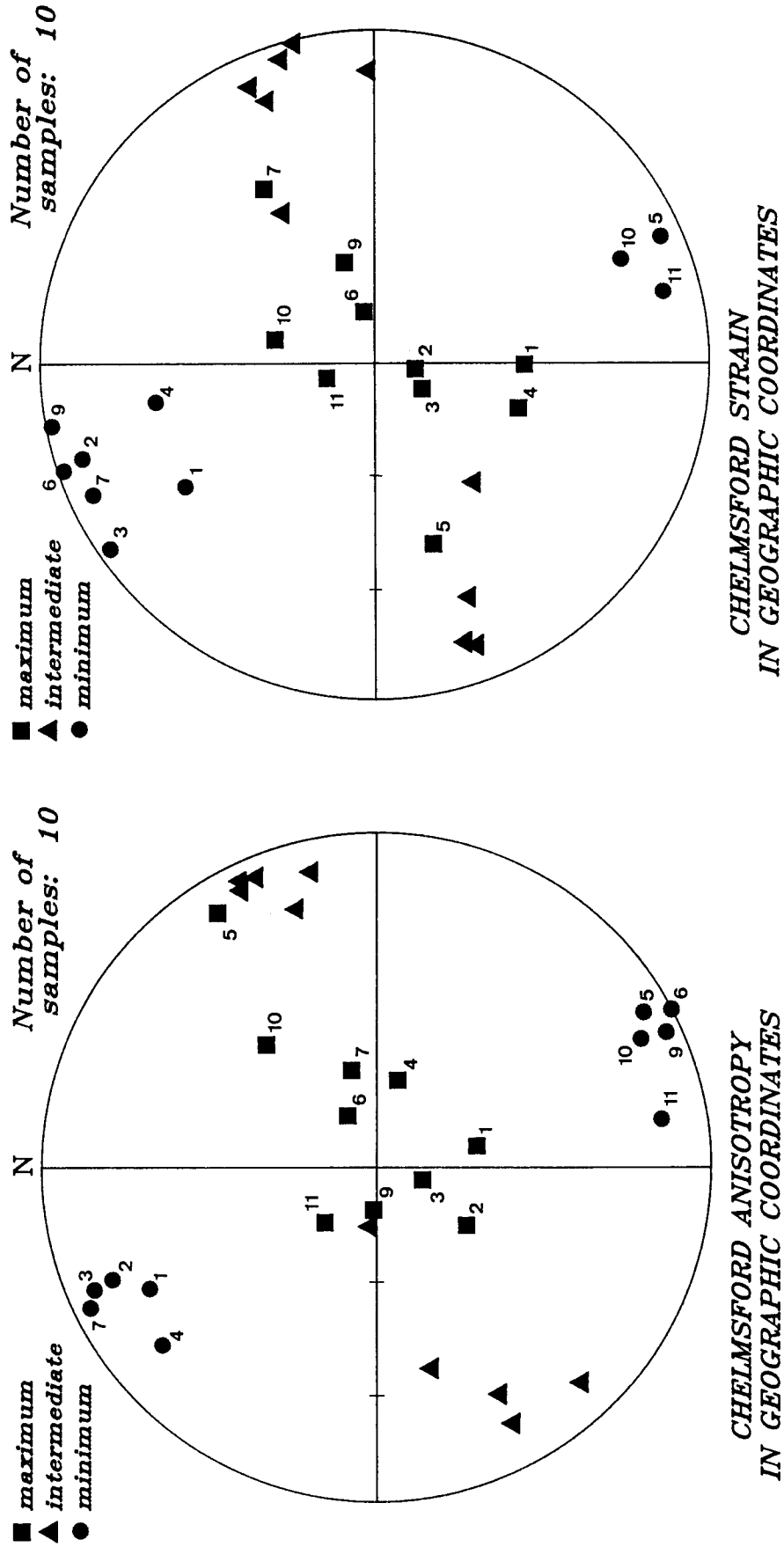
Figure 7.10. Equal area plots of the principal axes of the finite strain and susceptibility magnitude ellipsoids for the Chelmsford formation.

Table 7.1. Correlation of the finite strain with the AMS. N is the number of sites used in computing the regression. The correlation coefficients are significant at the 95% confidence level, except for those indicated by a star.

Direct comparison of principal axes (Method 1). N = 9	Comparison of ratios of the principal axes (Method 2). N = 9	Separate comparison of ε_i' and M_i (Method 3). N = 9	Global correlation of ε_i' and M_i (Method 4). N = 36
$X = 16.22\ k_{max} - 15.09$ $r = 0.83$	$\dfrac{X}{Y} = 16.76\ \dfrac{k_{max}}{k_{int}} - 15.68$ $r = 0.82$	$\varepsilon_1' = 11.58 M_1 + 0.14$ $r = 0.82$	
$Y = 8.43\ k_{int} - 7.31$ * $r = 0.59$ *1	$\dfrac{Y}{Z} = 8.16\ \dfrac{k_{int}}{k_{min}} - 6.72$ * $r = 0.52$	$\varepsilon_2' = 8.08 M_2 + 0.04$ *1 $r = 0.65$	$\varepsilon_i' = 19.97 M_i$ $r = 0.99$
$Z = 5.18\ k_{min} - 4.41$ *1 $r = 0.66$	$\dfrac{X}{Z} = 19.54\ \dfrac{k_{max}}{k_{min}} - 18.15$ $r = 0.75$	$\varepsilon_3' = 8.19 M_3 - 0.23$ $r = 0.71$	

[1] Correlation coefficients are only marginally insignificant at the 95% confidence level.

which the tight group of axes become less well-defined and eventually in the northeast become girdled within the cleavage (Figure 7.11b). Sites SO8, SO10 and SO14 located in the undeformed northern range of the basin do not display a systematic anisotropic magnetic susceptibility (Figure 7.11c). Site SO18, which is located in the extreme northeast corner of the basin, possesses a pencil-style fabric in which the suceptibility magnitude ellipsoid is prolate and the k_{max} axes are well-grouped and the k_{int} and k_{min} axes are less well-grouped (Figure 7.11d). As in the Chelmsford formation, the magnetic foliation of the Onaping breccia is subparallel to the long axis of the basin and shows the bifurcation of the basin at its east end (Figure 7.9). The k_{min} axes are subnormal to the cleavage at the sites which are deformed (Figure 7.12).

The shape of the susceptibility magnitude ellipsoid changes gradually as the deformation increases. The undeformed sites lie essentially in the field of flattening near the origin of the logarithmic plot, adapted for magnetic data (Figure 7.13). As the deformation increases the ellipsoids become prolate, where there is a well-defined lineation down-dip in the cleavage plane. The shape becomes oblate again for the southern sites, and prominent flow textures are seen in thin section. Site SO7 shows the strongest deformation with well-defined flow banding (Figure 7.14). The shape parameter, however, resembles that of the least deformed sites. Site SO7 has pyrrhotite as its only magnetic mineral. Schwarz (1974) found that pyrrhotite is easily mobilized at temperatures of a few hundred degrees, and in massive sulphide ores, the AMS of pyrrhotite may have resulted from the youngest metamorphic event. The fabric have reflected the stress at the time of recrystallization or the mechanical deformation of the existing pyrrhotite crystal. It is possible that pyrrhotite has been remobilized at site SO7 so that the shape of its ellipsoid is similar to the undeformed sites.

The strain markers in the red mudstones of the Lower Glarus Nappe complex and in the Chelmsford formation reflect the total finite strain. Since such strain markers do not exist for the Onaping formation, the mineral fragments within the breccia could be used as a measurement of the finite strain. Rousell (1975) compared axial ratios of glass, quartzite and quartz fragments in the Onaping and found that within the same sample, glass fragments were more deformed than the quartzite grains, which were in turn more deformed than the quartz grains. Microanalysis of the strain based on the clasts in the breccia has been made on thin sections by W. Clendenen (Clendenen, 1986).
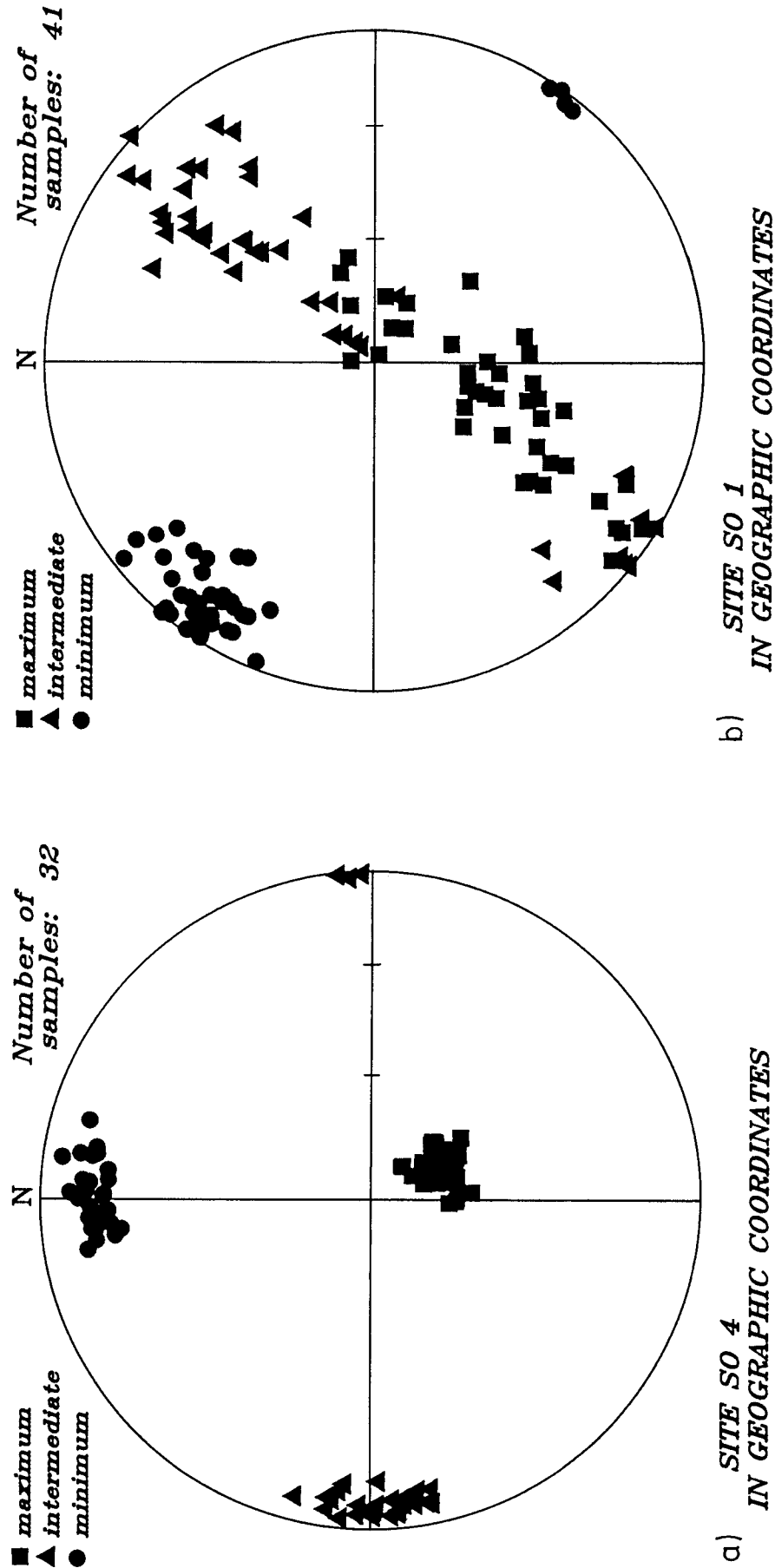
Figure 7.11. Equal area plots of the principal axes of the suceptibility magnitude ellipsoid for four sites of the Onaping formation: a) Site with well-developed, penetrative cleavage and triaxial susceptibility magnitude ellipsoid; b) site with penetrative cleavage and an oblate ellipsoid; c) undeformed site; and d) site with minor deformation.
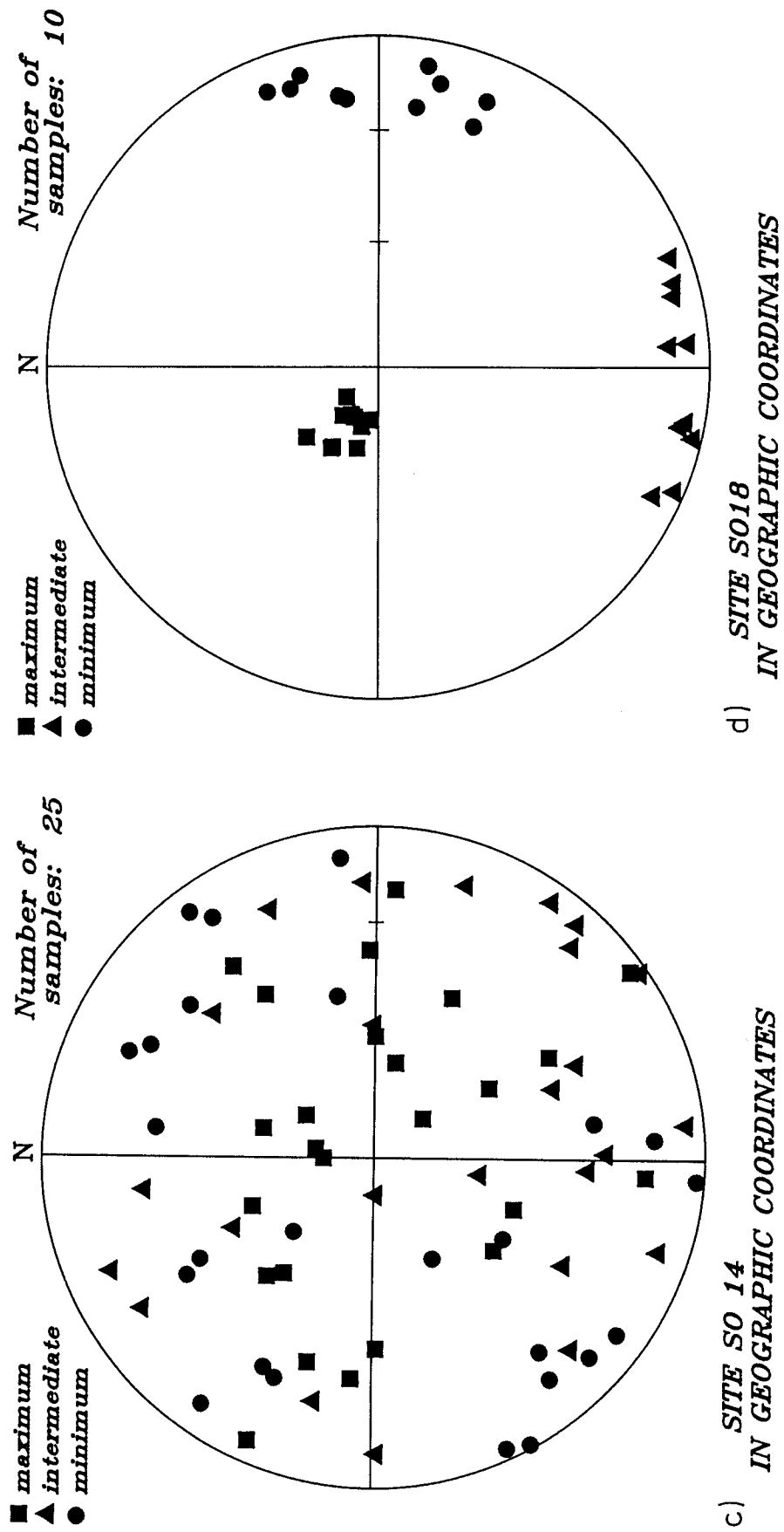
Figure 7.11. (continued)
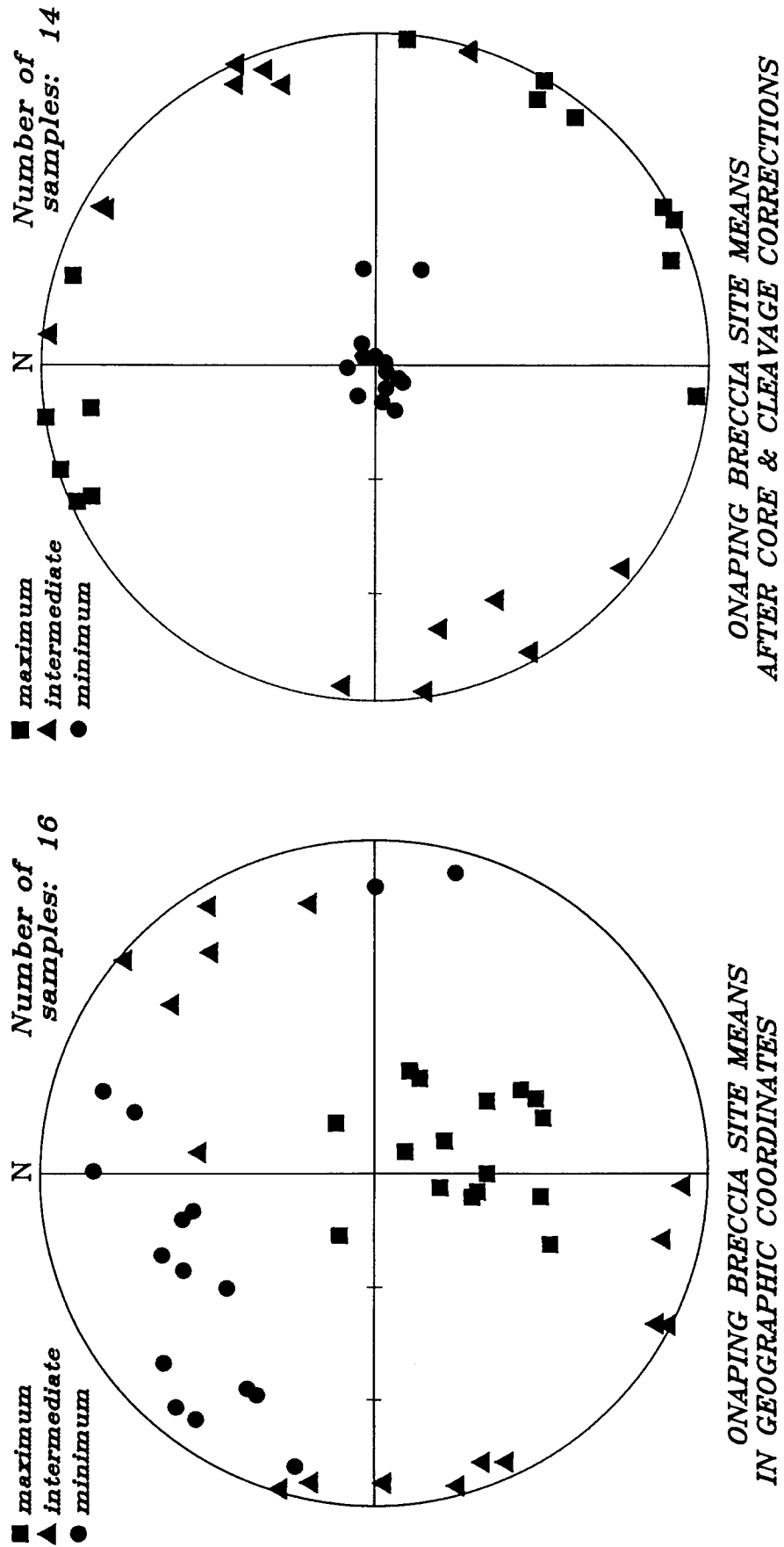
Figure 7.12. Equal area plots of the principal axes of the susceptibility magnitude ellipsoid for the site means of the Onaping formation.
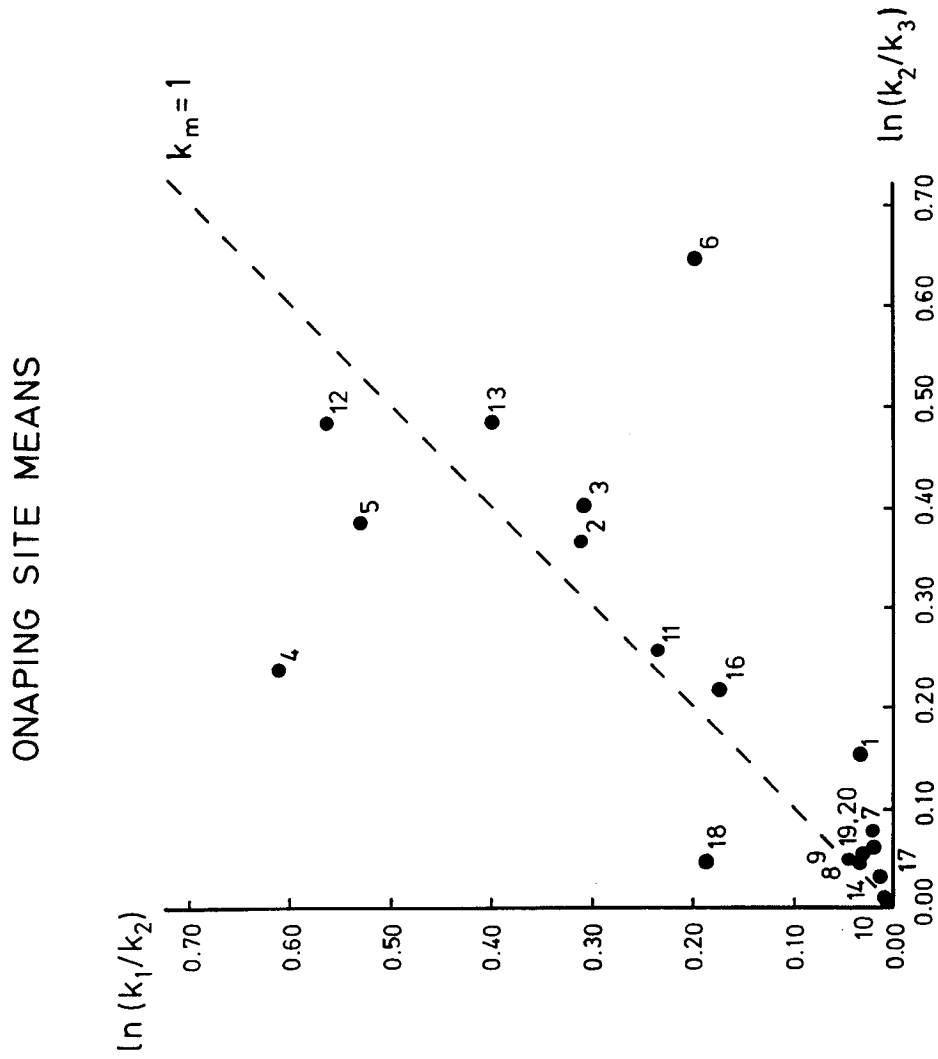
Figure 7.13. Logarithmic plots for the susceptibility magnitude ellipsoids for the site means of the Onaping formation.

Since the strain values can be dependent on the individual grains used for analysis, the question arises if the strain of the individual clasts can be correlated with the AMS. The strain value is determined for a single sample, therefore the strain should be correlated only with the AMS of that sample. Does this correlation provide an accurate measure for the strain at the site?

Figure 7.14.   Textural flow banding seen in thin section for site SO7. Quartz and plagioclase grains surrounded by mafic matrix minerals.

Strain of quartz grains in the Chelmsford formation

The finite strain of the Chelmsford formation was determined for one sample per site. Strain values and the equivalent AMS values for the individual samples are given in Table C.4 and C.5, respectively (Appendix C). The directions of the principal axes of the finite strain ellipsoids are not in as good agreement with the principal axes of the susceptibility magnitude ellipsoids as seen with the concretions (Figure 7.15). This is seen particularly when the magnitude ellipsoids are sectioned parallel to the planes of their respective strain ellipsoids. Of the sixteen sites, four sites (CM3, CM5, CM6 and CM7) were rejected from further analysis because the axes of the two ellipsoids varied by more than 30° from one another. Figure 7.16 compares the shapes of the finite strain and susceptibility magnitude ellipsoids.

The normalized lengths of the principal axes of the strain and magnetic ellipsoids for each sample can be compared as above, using the four correlation methods described earlier. Two further sites were eliminated from these correlations. The principal susceptibilities for site SO4 are anomalously low for their corresponding strain values, and for site SO10, the principal susceptibilities are too high. A total of ten samples were used in correlating the finite strain with the AMS and the results are given in Table 7.2.

In order to define an equivalent strain for each site, all samples at a single site had their principal susceptibilities converted to strains. The site mean for the equivalent strain ellipsoid was then defined by processing this information through AVANI. This mean equivalent strain ellipsoid can be compared to the finite strain ellipsoid derived from the concretions.

7.5 Discussion

Orientation of the finite strain and susceptibility magnitude ellipsoids

The orientation of the site mean susceptibility magnitude ellipsoid was found to reflect accurately the orientation of the respective finite strain ellipsoid at each site. A direct comparison of the orientations of the two ellipsoids on a sample level is not as good. It is possible that the strain and AMS of the sample are controlled by different phenomena on this very localized scale.
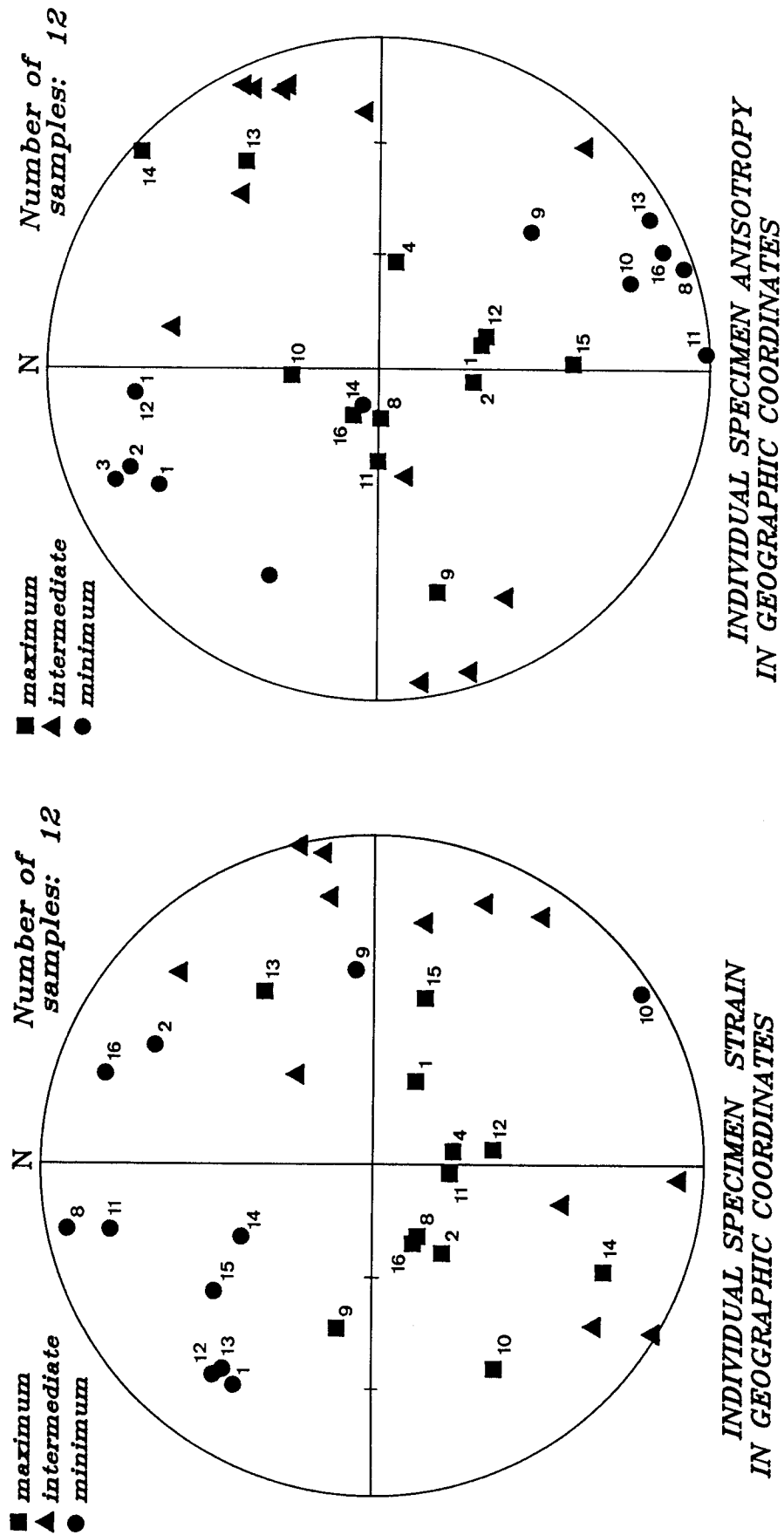
Figure 7.15. Equal area plots of the principal axes of the finite strain and susceptibility magnitude ellipsoids for individual specimens of the Chelmsford formation.

CHELMSFORD FORMATION   Individual Cores
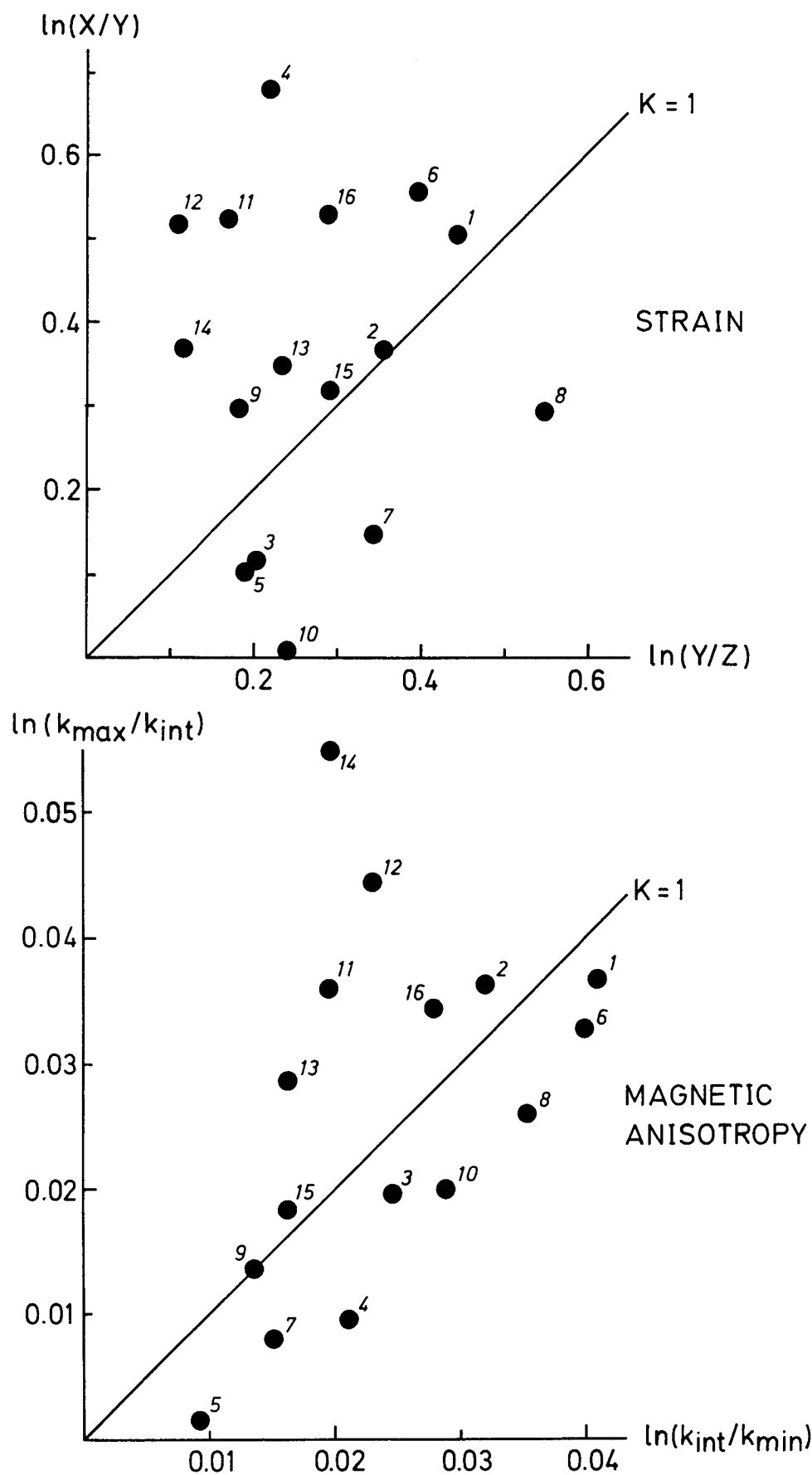
Figure 7.16. Logarithmic plots for the finite strain and an equivalent plot for the susceptibility magnitude ellipsoids for individual specimens of the Chelmsford formation.

Table 7.2. Correlation of the finite strain with the AMS. N is the number of samples used in computing the regression. The correlation coefficients are significant at the 95% confidence level.

Direct comparison of principal axes (Method 1). N = 10	Comparison of ratios of the principal axes (Method 2). N = 10	Separate comparison of ϵ_i' and M_i (Method 3). N = 10	Global correlation of ϵ_i' and M_i (Method 4) N = 30
$X = 8.89\ k_{max} - 7.71$ $r = 0.77$	$\dfrac{X}{Y} = 11.12\ \dfrac{k_{max}}{k_{int}} - 9.94$ $r = 0.78$	$\epsilon_1' = 6.17 M_1 + 0.19$ $r = 0.79$	$\epsilon_i' = 13.48 M_i - 0.01$ $r = 0.99$
$Y = 19.29\ k_{int} - 18.30$ $r = 0.87$	$\dfrac{Y}{Z} = 18.24\ \dfrac{k_{int}}{k_{min}} - 17.34$ $r = 0.80$	$\epsilon_2' = 20.49 M_2$ $r = 0.89$	
$Z = 7.60\ k_{min} - 6.69$ $r = 0.82$	$\dfrac{X}{Z} = 13.93\ \dfrac{k_{max}}{k_{min}} - 12.68$ $r = 0.75$	$\epsilon_3' = 9.80 M_3 - 0.08$ $r = 0.79$	

Principal axes of the finite strain and susceptibility magnitude ellipsoids

A comparison of the degree of flattening of the equivalent strain ellipsoids, X/Z, is made for the four correlation methods for the concretions. Although the Z-k_{min} correlation of Method 1 and the ε_2'-M_2 correlation of Method 3 are marginally not significant on the 95% confidence level (Table 7.1), they are used for deriving an equivalent strain in the following analysis. Table 7.3 lists the derived values of X/Z for the sixteen sites of the Chelmsford formation. The mean derived strain value averaged over ten sites, was between 2.16 (s.d. 0.25) and 2.23 (s.d. 0.54), depending on which of the four correlations was used. This is in excellent agreement with the mean strain value of 2.14 (s.d. 0.35) determined for the concretions of the same ten sites. Methods 1, 2 and 3 yield practically identical values for each site. Although actual site values may vary between one another for a site, no generalization can be made as to what method predicts the strain more accurately.

To predict the amount of down-dip extension within the cleavage plane, the X/Y ratio can be compared. Methods 2, 3 and 4 show significant correlations between finite strain and magnetic anisotropy, which can be used to derive equivalent strain values at each site. The actual strain measurements yield an average value of X/Y = 1.32 (s.d. 0.13) for the ten sites. The derived strain values are given in Table 7.4; the mean values for the three methods range from 1.33 (s.d. 0.10) to 1.35 (s.d. 0.17). As above, Methods 2 and 3 yield practically identical values for the equivalent strain at a given site, and the "global correlation" (Method 4) yields values very close to the other methods.

In general, each correlation method provides a reasonable estimate of the finite strain. Figure 7.17 shows the horizontal projections of the calculated strain ellipsoid for Methods 2, 3 and 4 on a map plan of the basin along with the projections from the concretion-derived strain.

Prediction of the site-mean finite strain ellipsoid from the microfabric - AMS correlation for individual specimens

The validity as to whether the AMS can be correlated to the finite strain derived from a single mineral has never been adequately tested. Since an eventual correlation of the AMS with a strain derived from mineral fragments from the Onaping is necessary in order to calculate the original shape of the Sudbury Basin, a test of the method would be appropriate.

Table 7.3. Comparison of the derived X/Z correlation with the directly
measured strain values. N is the number of sites used to
calculate the mean strain value.

Site	Method 1	Method 2	Method 3	Method 4	Strain from Concretions
1	2.574	2.562	2.618	3.185	2.071
2	2.406	2.406	2.447	2.769	2.291
3	2.212	2.230	2.222	2.315	2.303
4	2.057	2.093	2.066	2.012	1.800
5	1.969	1.976	1.970	1.821	1.978
6	2.366	2.387	2.384	2.660	2.710
7	1.784	1.800	1.790	1.521	1.714
8	2.594	2.582	2.642	3.250	
9	1.875	1.879	1.875	1.647	1.707
10	2.034	2.054	2.035	1.932	2.527
11	2.289	2.289	2.301	2.456	2.333
12	2.358	2.347	2.382	2.610	
13	2.871	2.792	2.107	3.967	
13	2.206	1.398	1.577	2.268	
14	2.466	2.465	2.513	2.941	
15	1.856	1.879	1.865	1.648	
16	2.783	2.719	2.865	3.737	

a.) N=10   N=10   N=10   N=10   N=10
     X/Z=2.16   X/Z=2.16   X/Z=2.17   X/Z=2.23   X/Z=2.14
     s.d. 0.25 s.d. 0.25 s.d. 0.27 s.d. 0.54 s.d. 0.35

b.) N=17   N=17   N=17   N=17
     X/Z=2.28   X/Z=2.23   X/Z=2.22   X/Z=2.51
     s.d. 0.32 s.d. 0.37 s.d. 0.35 s.d. 0.73

a.) Only sites with directly measured finite strain values.

b.) All sites.

Table 7.4. Comparison of the derived X/Y correlation with directly
measured strain values. N is the number of sites used to
calculate the mean strain value.

Site	Method 2	Method 3	Method 4	Strain from Concretions
1	1.451	1.458	1.553	1.281
2	1.486	1.471	1.615	1.449
3	1.317	1.329	1.323	1.347
4	1.251	1.269	1.222	1.151
5	1.285	1.285	1.271	1.270
6	1.350	1.365	1.377	1.489
7	1.134	1.170	1.062	1.063
8	1.434	1.446	1.522	
9	1.268	1.266	1.245	1.300
10	1.318	1.315	1.323	1.420
11	1.418	1.410	1.491	1.377
12	1.529	1.495	1.681	
13	1.649	1.661	1.972	
13	1.381	1.385	1.433	
14	1.417	1.425	1.491	
15	1.167	1.198	1.105	
16	1.662	1.660	2.011	

	Method 2	Method 3	Method 4	Strain from Concretions
a.)	N=10 X/Y=1.33 s.d. 0.10	N=10 X/Y=1.33 s.d. 0.09	N=10 X/Y=1.35 s.d. 0.17	N=10 X/Y=1.32 s.d. 0.13
b.)	N=17 X/Y=1.38 s.d. 0.15	N=17 X/Y=1.39 s.d. 0.14	N=17 X/Y=1.39 s.d. 0.32	

a.)   Only sites with directly measured strain values.

b.)   All sites.
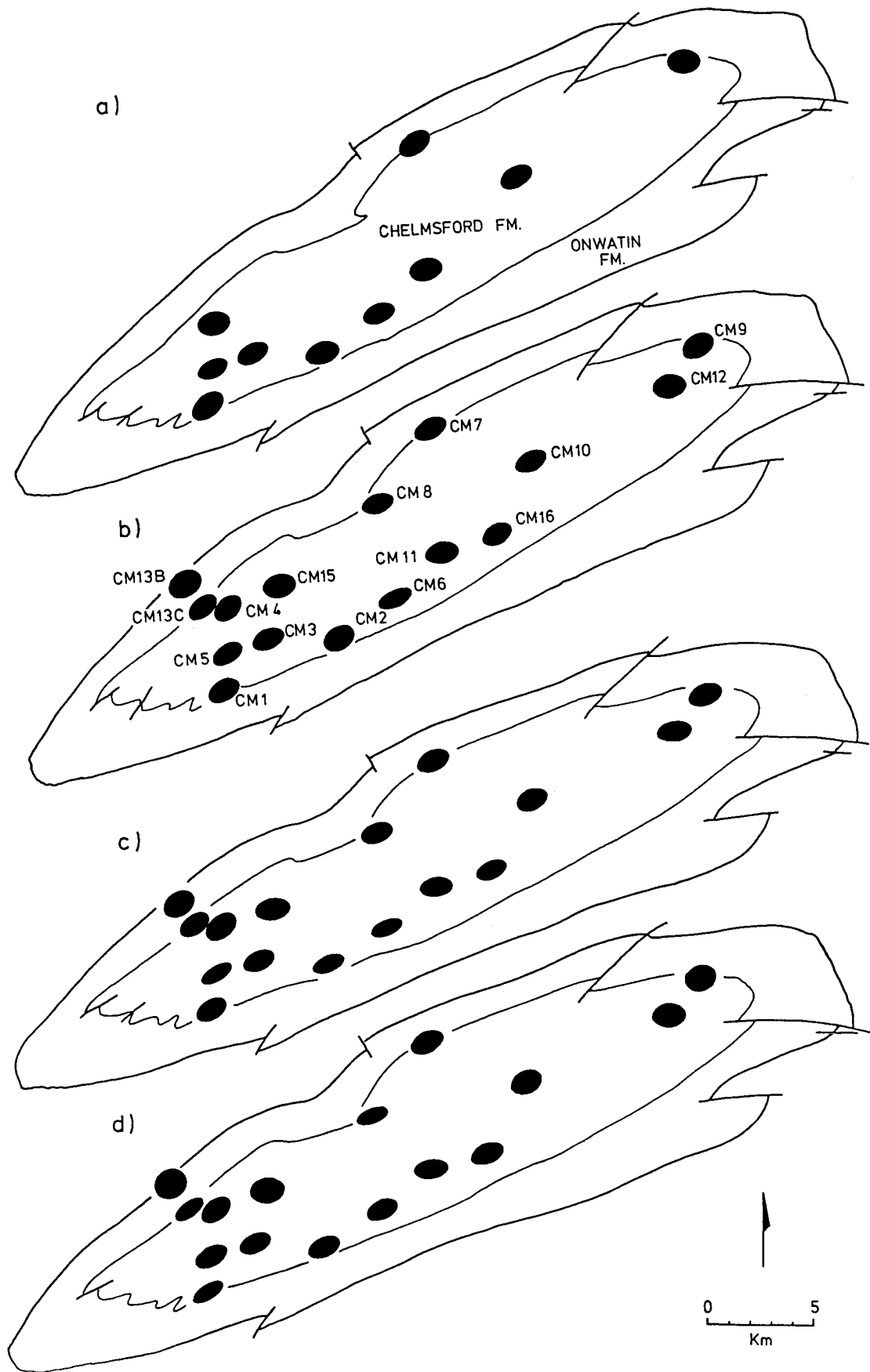
Figure 7.17. Horizontal projection of the finite strain ellipsoids a) which were calculated from the concretions, b) which were derived from the AMS, using the correlation of Method 2, c) Method 3 and d) Method 4 on a map plan of the Sudbury Basin.

A comparison of the total finite strain derived from the concretions with the equivalent strain site means derived from the microfabric - AMS correlation should show strain values that are similar. Figure 7.18a-d shows the lengths of the principal axes of the concretion-derived strain ellipsoid plotted against the lengths of the principal axes of the sample-derived equivalent strain ellipsoid. If the sample-derived equivalent strain is an accurate estimation of the total finite strain, then the points should lie close to a line with positive unit slope. Although the slopes vary between 0.568 to 1.261, in each of the four cases the t-test shows that the regression slope is not statistically different from a unit slope ($t_1 < t_{crit}$) at a 95% confidence level (Table 7.5). The site-mean strain derived by applying the microfabric - AMS correlation to convert all anisotropies to an equivalent strain is a good approximation of the total finite strain.

7.6 Conclusions

The AMS can accurately predict the orientation of the finite strain ellipsoid in the Chelmsford formation of the Sudbury Basin. The orientations of the principal axes of the individual sample strain may not reflect exactly the anisotropy on such a local scale. Strain determinations must be made for several samples and averaged for a site, rather than relying on strain data from a single sample. This average value will not be strongly affected by any local strain effects.

All four correlation methods tested predict equally well the lengths of the principal axes of the strain ellipsoid. The derived strain values provide additional estimates of strain in the Chelmsford formation where concretions are not found. These measurements are necessary for future modeling of the basin to remove the effect of strain.

The Chelmsford formation does not show a large variation of strain across the basin. The analysis of how well microfabric can be correlated to the AMS to predict the total finite strain at a site was successful in the Chelmsford formation. The Onaping shows a progressive change of the susceptibility magnitude ellipsoid across the basin with increasing deformation. The ability to determine an equivalent finite strain by correlating the microfabric and AMS data in the Onaping formation will be important in determining the original shape of the basin.
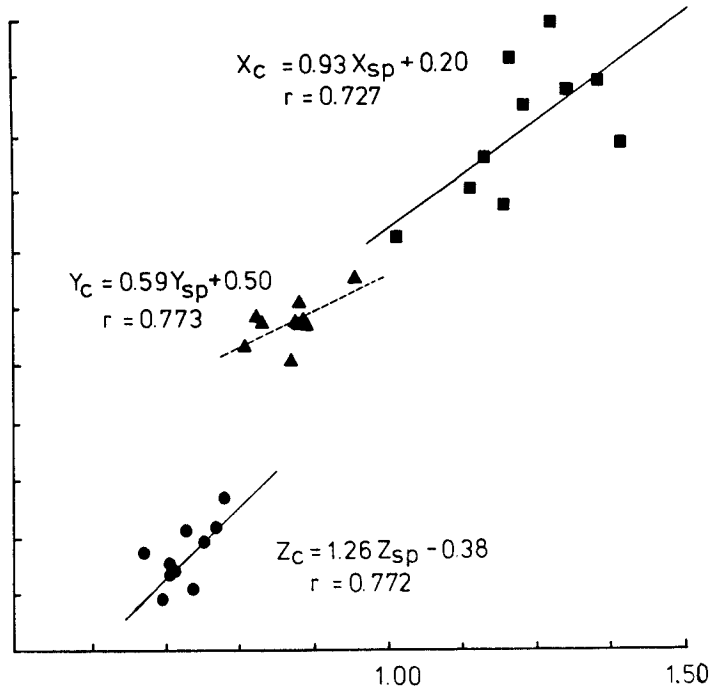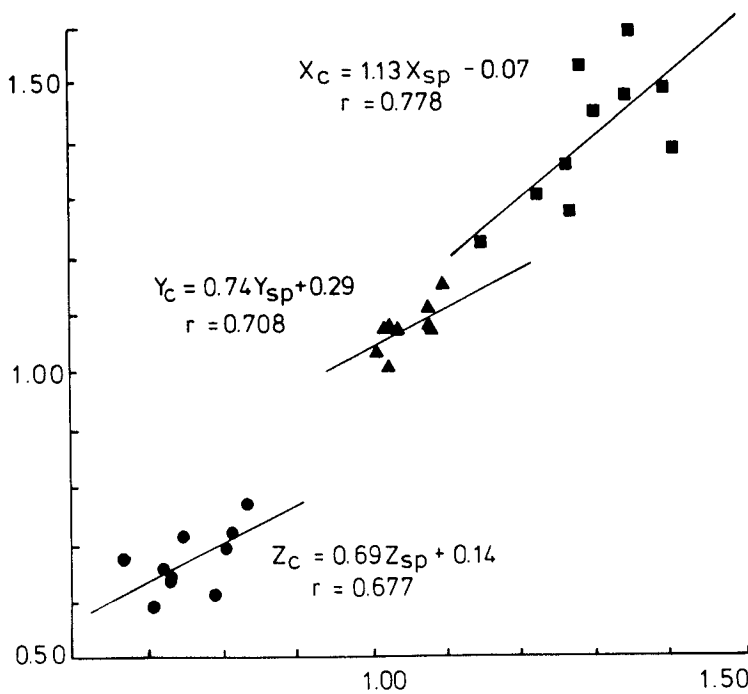
Figure 7.18. Correlation of the total finite strain with the finite strain derived from the individual samples, using the correlation from: a) Method 1, b) Method 2, c) Method 3 and d) Method 4. Lengths of the principal axes of the total finite strain are plotted on the ordinate and the lengths of the principal axes of the site means of the finite strain derived from the individual samples are plotted on the abscissa. The correlation co-efficient, r, is given at the 95% confidence level.

Table 7.5. T-test statistics for the comparison of the total finite strain derived from concretions with the finite strain derived from the microfabric - AMS correlation.

	Regression slope	t_o	t_1	t_{crit}
Method 1				
Maximum	1.134	3.480	0.412	2.306
Intermediate	0.744	2.837	0.979	2.306
Minimum	0.692	2.605	1.162	2.306
Method 2				
Maximum	0.935	2.997	0.209	2.306
Intermediate	0.593	3.448	2.360	2.306
Minimum	1.261	3.434	0.711	2.306
Method 3				
Maximum	1.172	3.522	0.516	2.306
Intermediate	0.724	2.876	1.099	2.306
Minimum	0.705	2.622	1.002	2.306
Method 4				
Maximum	0.940	3.715	0.237	2.306
Intermediate	0.737	2.620	0.936	2.306
Minimum	0.568	2.802	2.135	2.306

Chapter 8. SUMMARY AND GENERAL DISCUSSION

Paleomagnetic and AMS data provide valuable information in the study of areas which have undergone tectonic deformation. Paleomagnetism not only predicts large-scale plate motions but it can also indicate regional and local displacements and rotations. It has been seen in the first study in this dissertation (described in Chapter 4) that paleomagnetic vectors provide cogent evidence that the curvature of the northern Apennine mountain belt is primary. The mean paleomagnetic direction for all the sites suggests that the Umbria-Marches region has only undergone trans- lation relative to the autochthonous areas of the Adriatic promontory. More generally, the study of the Majolica formation illustrates that the quality of paleomagnetic data from deformed areas depends on the geological, particularly structural, information available. The between-site scatter of directions in the Majolica formation is probably due to defor- mation that has not been compensated for, either on a regional or site scale. Although paleomagnetic data can afford a better insight into how a region has been affected by deformation, detailed structural control is necessary to assure the accuracy of this information.

A phenomenon which is not as yet well understood is the effect that deformation can have on the remanent magnetization. This must be un- derstood, however, in order that paleomagnetic data can be corrected for the effect of this deformation. In the Lower Glarus Nappe complex (Chapter 6) the ChRM directions have been systematically displaced from their expected Permo-Triassic direction. A model for horizontal simple- shear explains not only the observed deformation in the nappe complex, but it also predicts the dispersion of the ChRM vectors. The AMS of the Glarus sites was correlated with the finite strain and was used to compute the finite strain at paleomagnetic sites where direct strain data were not available. However, the calculated strain values for the individual sites do not vary as predicted by the simple shear model. It is clear that if paleomagnetism is to be used as a tool to decipher tectonic deformation, then more information is required on how the remanent magnetization is affected by various types of deformation. The degree of deformation necessary to have an effect on the magnetization must also be evaluated. Future work should include experimental modeling under known conditions of deformation. Under controlled situations it should be possible to gain additional insight into the phenomenon of how remanence is affected by deformation.

The AMS was found to be an accurate indicator of the orientation of the finite strain ellipsoid. Borradaile and Mothersill (1984) have questioned the accuracy with which the AMS can predict the magnitude of the finite strain. To answer this question five methods of correlating the finite strain ellipsoid with the susceptibility magnitude ellipsoid (see Chapter 5.3) were evaluated in this study. The specific conclusions for the two AMS investigations are given at the end of each chapter (Chapter 5 and 7). A general discussion about these methods of correlation follows.

The correlation of the shape of the finite strain and the susceptibility magnitude ellipsoids (Method 5) was found to be an unreliable method. The change of shape of the susceptibility ellipsoid was seen to be saturated with increasing deformation as expected on physical grounds. The other four methods of correlation predict the magnitudes of the principal strain axes in the Chelmsford formation with equal accuracy. In the Lower Glarus Nappe complex some correlation methods appeared to predict the finite strain better than others. The correlation of the separate axes of the two ellipsoids and the correlation of the ratios of the principal axes provided the best estimates of the strain ellipsoids. The correlation of the separate axes with one another can be made by comparing (a) $X_i/\bar{X}$ with $k_i/\bar{k}$ (for i = 1, 2, 3, where $X_1 > X_2 > X_3$ and $k_1 > k_2 > k_3$), or (b) ϵ_i' ($\ln[X_i/\bar{X}]$) with M_i ($[k_i - \bar{k}]/\bar{k}$). Since $\ln(z) \simeq z-1$ for $z \simeq 1$, M_i is essentially $\ln(k_i/\bar{k})$ because the ratio $k_i/\bar{k}$ is always close to one. For such a situation the correlation of Method 3 used in the present studies is essentially equivalent to the correlation method applied by Rathore (1979, 1980).

From the analysis in the Glarus and Sudbury it can be seen that both Methods 1 and 3 provide a significant correlation of the finite strain with the AMS. This can be explained as follows. When correlating the individual axes of the finite strain against the AMS, the range of magnitudes of the k_i axes is relatively small. The k_i values generally vary by less than one percent from their mean value. On the other hand, X_i can vary greatly from its mean value for a given axis. For a direct correlation of the magnitudes of the axes of the finite strain with those of the anisotropy (Method 1), we can write

$$X_i/\bar{X} = a(k_i/\bar{k}) + b .$$

The log correlation (Method 3) defined by

$$\ln(X_i/\overline{X}) = c \, \ln(k_i/\overline{k}) + d$$

and taking the exponential on both sides gives

$$X_i/\overline{X} = e^{c \, \ln(k_i/\overline{k}) + d} \qquad .$$

Letting $d' = e^d$, we can now write

$$X_i/\overline{X} = d'(k_i/\overline{k})^c \quad .$$

When plotted, this has the form shown in Figure 8.1 when $c > 1$. If $k_i/\overline{k}$ does not vary greatly, the tangent to the curve in this small range will have a slope which approximates the slope a of Method 1. Therefore, when $k_i/\overline{k}$ varies by less than a few percent, the direct correlation of the principal axes approximates the correlation of the log values of these axes. If $k_i/\overline{k}$ varies by more than a few percent, then the direct correlation will not be as accurate since the linearization of the logarithmic model is not valid.
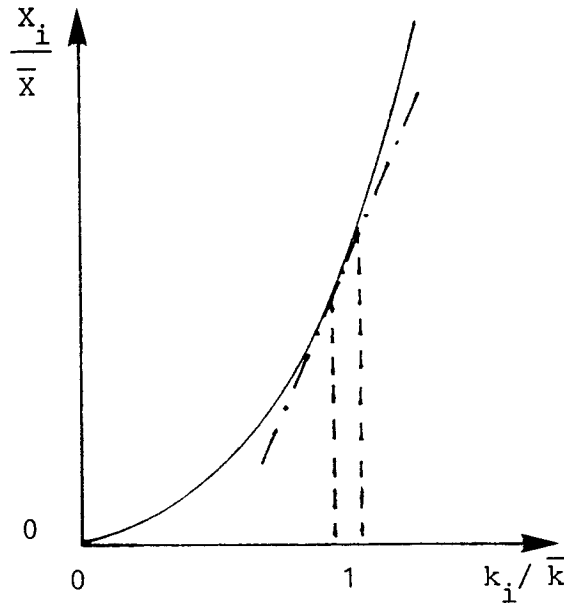
Figure 8.1. Power-law relationship of the normalized magnitudes of the principal axes of the finite strain with the AMS.

From the AMS study in the Lower Glarus Nappe complex, it was seen that the global correlation of all the principal axes together did not provide an accurate finite strain value. This result suggests that the power-law relationship above does not provide an accurate description of the relation between finite strain and the anisotropy under all circumstances. The global correlation did provide accurate strain values for the Chelmsford formation. Here the magnitude of the principal axes of the susceptibility magnitude ellipsoid varied by only two percent and the strain ellipsoid by eighteen percent. In the Lower Glarus Nappe complex the anisotropy magnitudes varied by three percent, but the strain magnitudes of the principal axes varied by over 100%. The global correlation does not appear to be sufficiently accurate when there are large variations in either the strain or the anisotropy.

In answer to the question, which correlation method provides an accurate estimate of the finite strain, it can be seen that a correlation of the magnitudes of the principal finite strains with the normalizesd principal susceptibilities works best when the maximum, intermediate and minimum axes are considered separately (Methods 1 ,2 and 3). Here the variations in the strain and the anisotropy are not large, and an equivalent finite strain calculated from the correlation is relatively accurate. It is not always possible to have a significant correlation of the separate axes, and sometimes only the global correlation method provides a means of estimating a finite strain from the anisotropy data. It should be noted that if the anisotropy values do not vary by more than a few percent and the finite strain does not vary by more than a few tens of percent, then the global correlation probably provides reliable strain results. However, if the anisotropy values at a site vary by more than a few percent from the mean anisotropy of all the sites, or if there is a large range of strain values in the area, then the equivalent strain predicted from this AMS data using the global correlation will deviate from the true strain value.

Appendix A: Measurement of AMS with a Spinner Magnetometer

The basic principles behind measurement of AMS with a spinner magnetometer are discussed by Lowrie (1968). It involves spinning a specimen in a constant applied field, generated by a pair of Helmholtz coils applied coaxially with detection coils. A magnetization, M, is induced and the polarity is changed twice during each rotation cycle. If a specimen is isotropic, no change of flux occurs in the pick up coils. If the specimen is anisotropic, then the magnitude of the induced signal depends on the variation of the susceptibility in the plane of rotation. A maximum induced magnetization is produced when the maximum susceptibility parallels the field. The change of magnetization in the detection coil induces a voltage with amplitude and phase which are determined by the differences in the length of the axes of the susceptibility magnitude ellipsoid in the plane of the spin. It is therefore the susceptilibity differences which are being measured (see Chapter 2, section 2.5). The direction of these axes are related to the reference axes.

If a specimen is rotated about its vertical (z) axis with an angular velocity of ρ, after time t, the reference X-axis makes an angle $\theta = \rho t$ relative to an applied field (Figure A.1). The components M_x and M_y of M induced in the X-Y plane by the horizontal field can be expressed by
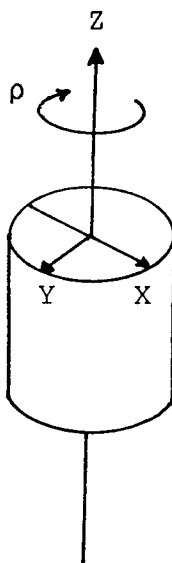
Figure A.1. Specimen coordinate system.

$$M_i = k_{ij}H_j \tag{A.1}$$

which now becomes

$$M_x = H[k_{xx}\cos(\rho t) - k_{xy}\sin(\rho t)]$$

$$M_y = H[k_{xy}\cos(\rho t) - k_{yy}\sin(\rho t)] .$$

The magnetization in the direction of the field is

$$M_H = M_x\cos(\rho t) - M_y\sin(\rho t)$$

$$= H\ k_{xx}\cos^2(\rho t) - 2k_{xy}\sin(\rho t)\cos(\rho t) + k_{yy}\sin^2(\rho t)$$

$$= H(k_{xx} + k_{yy})/2 + H(k_{xx} - k_{yy})\cos(2\rho t)/2$$

$$- Hk_{xy}\sin(2\rho t) .$$

The first term is constant, so it does not contribute to the induced signal in the coils. The second term is inphase with the system reference signal (inphase component), $I_z = H(k_{xx} - k_{yy})/2$, and the third term is shifted 90 in phase (quadrature component), $Q_z = -Hk_{xy}$. If the specimen is now spun around the x- and y-axes, the corresponding inphase and quadrature components can be found, where

$$I_x = H(k_{yy} - k_{zz})/2 , \quad Q_x = -Hk_{yz} , \text{ and}$$

$$I_y = H(k_{zz} - k_{xx})/2 , \quad Q_y = -Hk_{zx} .$$

The susceptilibity differences can now be defined as

$$k_{xx} - k_{yy} = 2I_z/H = A_z , \quad k_{xy} = -Q_z/H = -B_z$$

$$k_{yy} - k_{zz} = 2I_x/H = A_x , \quad k_{yz} = -Q_x/H = -B_x \tag{A.2}$$

$$k_{zz} - k_{xx} = 2I_y/H = A_y , \quad k_{zx} = -Q_y/H = -B_y .$$

Next, the orientations and the dimensions of the susceptibility magnitude ellipsoid discussed in Chapter 2 (section 2.4) can be calculated from (A.1) and (A.2). When one of the principal axes of the ellipsoid corresponds to the field direction, then with $i = x$, y or z,

$$M_i = \beta H_i .$$
(A.3)

Combining (A.1) and (A.3) gives the condition for the principal axes, where $i,j = x$, y or z, such that

$$M_i = k_{ij}H_j = \beta H_i$$

or

$$(k_{ij} - \beta\delta_{ij})H_j = 0 .$$
(A.4)

In order to have a nontrivial solution, the determinant of the coefficients, $D(\beta)$, must equal zero,

$$D(\beta) = \begin{vmatrix} (k_{xx} - \beta) & k_{xy} & k_{xz} \\ k_{yx} & (k_{yy} - \beta) & k_{yz} \\ k_{zx} & k_{xy} & (k_{zz} - \beta) \end{vmatrix} = 0 .$$
(A.5)

The determinant can be simplified by expressing it in terms of the quantities A_i and B_i of (A.2). It is then possible to write

$$\beta = \bar{k} + \alpha,$$

where $\bar{k} = (k_{xx} + k_{yy} + k_{zz})/3$, so that

$$k_{xx} - \beta = k_{xx} - \bar{k} - \alpha$$

$$= (2k_{xx} - k_{yy} - k_{zz})/3 - \alpha$$

$$= [(k_{xx} - k_{yy}) - (k_{zz} - k_{xx})]/3 - \alpha$$

$$= (A_y - A_z)/3 - \alpha$$

$$= C_x - \alpha .$$

Doing the same for $(k_{yy} - \beta)$ and $(k_{zz} - \beta)$ thus finding C_y and C_z, (A.5) reduces to

$$D(\alpha) = \begin{vmatrix} (C_x - \alpha) & B_z & B_y \\ B_z & (C_y - \alpha) & B_x \\ B_y & B_x & (C_z - \alpha) \end{vmatrix} = 0 . \qquad (A.6)$$

We can expand the determinant as

$$D(\alpha) = (C_x C_y C_z + 2B_x B_y B_z - C_x B_x^2 - C_y B_y^2 - C_z B_z^2)$$

$$+ \alpha(B_x^2 + B_y^2 + B_z^2 - C_x C_y - C_y C_z - C_z C_x)$$

$$+ \alpha^2(C_x + C_y + C_z) - \alpha^3,$$

and since

$$(C_x + C_y + C_z) = 0 \quad \text{and}$$

$$2(C_x C_y + C_y C_z + C_z C_x) =$$

$$(C_x + C_y + C_z)^2 - (C_x^2 + C_y^2 + C_z^2) =$$

$$-(C_x^2 + C_y^2 + C_z^2) ,$$

we can write

$$\alpha^3 - P\alpha + Q = 0 , \qquad (A.7)$$

where

$$P = \Sigma(B_i^2) + (1/2)\Sigma(C_i)^2 , \quad i = x,y,z$$

and

$$Q = C_x C_y C_z + 2B_x B_y B_z - C_x B_x^2 - C_y B_y^2 - C_z B_z^2 .$$

The solution to (A.7) has been given by Granar (1958) in the form

$$\alpha_1 = -2\alpha_o \cos(t)$$

$$\alpha_2 = -2\alpha_o \cos(t - 2\pi/3)$$

$$\alpha_3 = -2\alpha_o \cos(t + 2\pi/3),$$

where $\alpha_o = \sqrt{P/3}$ and $\cos(3t) = Q/(2\alpha_o)^3$.

These can be written as

$$\alpha_1 = -2\alpha_o \cos(t)$$

$$\alpha_2 = \alpha_o [\cos(t) - \sqrt{3} \sin(t)]$$

$$\alpha_3 = \alpha_o [\cos(t) + \sqrt{3} \sin(t)] .$$

The lengths of the principal axes of the AMS magnitude ellipsoid are found by adding the average susceptibility, k, to α_i, according to

$$K_{max} = \bar{k} + \alpha_{max}$$

$$K_{int} = \bar{k} + \alpha_{int}$$

$$K_{min} = \bar{k} + \alpha_{min}$$

To calculate the orientations of these axes, the α_i solutions can be substituted into (A.5) in turn, to obtain the directional cosines of the particular axis.

Seite Leer /
Blank leaf

Appendix B: Magnetic Susceptibility and Finite Strain Data for the Lower Glarus Nappe Complex.

Table B.1. Intensities and directions for the site mean principal axes
of the magnetic susceptibility ellipsoid. N is the number
of specimens per site, D is the declination and I is the
inclination in geographic coordinates.

Site	N	k_{max}	D	I	k_{int}	D	I	k_{min}	D	I
GV1	15	1.022	182.9	0.4	1.015	92.8	8.3	0.965	275.5	81.7
GV2	6	1.017	225.3	10.7	1.011	130.5	23.8	0.973	337.8	63.6
GV3	13	1.050	191.9	21.7	1.007	98.5	8.5	0.947	348.3	66.5
GV4	28	1.020	331.9	0.2	1.006	241.8	29.1	0.975	62.2	60.9
GV5	21	1.027	357.4	0.3	1.014	87.5	13.6	0.960	266.0	76.4
GV6	13	1.011	158.8	19.4	1.002	62.1	18.2	0.988	292.2	62.9
GV7	25	1.018	214.6	25.9	1.010	102.9	37.3	0.973	330.2	41.7
GV8	12	1.022	144.7	0.7	1.010	54.7	3.6	0.969	245.1	86.4
GV9	20	1.025	322.1	35.7	1.005	61.8	13.3	0.971	168.8	51.1
GV10	26	1.030	155.4	25.1	1.019	60.2	11.1	0.953	308.4	62.2
GV11	16	1.025	167.4	6.7	1.017	262.6	37.4	0.960	68.8	51.8
GV12	28	1.021	190.9	13.2	1.008	95.5	22.0	0.971	309.7	64.0
GV13	16	1.019	35.0	3.4	1.007	125.6	11.3	0.974	288.6	78.2
GV14	9	1.032	29.3	8.5	1.005	120.6	9.0	0.964	256.7	77.6
GV15	15	1.034	15.6	0.2	1.008	105.7	16.8	0.959	285.1	73.2
GV16	14	1.013	194.4	0.3	1.001	284.5	16.2	0.986	103.3	73.8
GV17	12	1.012	203.9	5.5	1.002	296.3	23.9	0.986	101.8	65.4
GV18	16	1.009	181.5	9.2	1.002	272.8	8.0	0.990	43.3	77.8
GV19	17	1.008	211.4	25.7	1.002	104.0	31.9	0.990	332.3	46.9
GV20	23	1.018	190.3	26.4	1.007	281.7	2.9	0.975	17.6	63.4
GV21	16	1.022	196.8	14.0	1.009	101.0	21.8	0.970	317.0	63.7
GV22	19	1.023	197.3	7.4	1.017	288.2	6.6	0.961	59.8	80.1
GV23	18	1.023	197.3	14.3	1.021	102.6	17.9	0.958	323.8	66.8
GV24	28	1.022	13.5	2.5	1.005	103.6	1.8	0.973	229.9	86.9
GV25	23	1.012	356.3	5.2	1.007	86.7	4.6	0.981	217.8	83.1
GV26	22	1.026	325.6	5.5	1.009	55.8	1.3	0.966	158.8	84.4
GV27	16	1.011	328.7	3.2	1.007	59.9	21.5	0.982	230.6	68.2

Table B.2. Intensities and directions for the principal axes of the finite strain ellipsoid.   D is the declination and I is the inclination in geographic coordinates. Strain data of the starred sites (*) were provided by Dr. O. A. Pfiffner.

Site	X	D	I	Y	D	I	Z	D	I
GV1	9.633	180.0	20.0	4.296	87.0	8.0	1.000	337.0	68.0
GV2	4.902	216.0	15.0	2.360	117.0	31.0	1.000	328.0	54.0
GV3*	3.160	176.0	3.0	1.680	86.0	2.0	1.000	325.0	85.0
GV4	4.573	159.0	2.0	1.967	251.0	33.0	1.000	67.0	57.0
GV6	2.629	60.0	5.0	1.872	329.0	5.0	1.000	198.0	83.0
GV7	5.173	216.0	27.0	2.943	105.0	35.0	1.000	335.0	43.0
GV10*	13.490	164.0	20.0	7.100	63.0	1.0	1.000	342.0	71.0
GV11	7.826	159.0	25.0	3.110	259.0	20.0	1.000	23.0	57.0
GV12	5.495	180.0	13.0	3.477	88.0	10.0	1.000	323.0	73.0
GV13*	8.474	190.0	5.0	4.460	97.0	26.0	1.000	289.0	63.0
GV14*	7.060	206.0	4.0	2.000	114.0	26.0	1.000	316.0	63.0
GV15	4.631	200.0	13.0	2.908	290.0	3.0	1.000	66.0	86.0
GV20	5.751	161.0	27.0	2.289	63.0	15.0	1.000	306.0	58.0

Seite Leer /
Blank leaf

Appendix C: Magnetic Susceptibility and Finite Strain Data for the Sudbury Basin, Ontario, Canada.

Table C.1.   Intensities and   directions for the site mean principal axes of the magnetic susceptibility ellipsoid for the   Chelmsford Formation.   N is the number of specimens per site,   D is the declination and   I   is the inclination in geographic co-ordinates.

Site	N	k_{max}	D	I	k_{int}	D	I	k_{min}	D	I
CM1	42	1.027	167.5	64.9	1.005	64.6	6.0	0.969	331.9	24.3
CM2	30	1.025	212.2	64.0	1.001	72.9	20.3	0.974	337.0	15.5
CM3	35	1.019	194.0	78.5	1.005	67.6	6.9	0.977	336.5	9.1
CM4	39	1.015	103.6	67.8	1.005	226.2	12.4	0.980	320.3	18.1
CM5	29	1.014	58.1	11.4	1.002	275.6	75.8	0.984	149.8	8.5
CM6	39	1.022	61.7	75.5	1.006	241.8	14.5	0.973	151.8	0.0
CM7	26	1.008	75.9	65.2	1.005	241.3	24.1	0.987	333.8	5.5
CM8	25	1.027	248.9	73.0	1.006	70.7	17.0	0.968	340.6	0.5
CM9	24	1.012	273.5	79.9	1.001	64.1	8.8	0.987	154.9	4.9
CM10	29	1.016	48.5	49.0	1.002	254.5	38.0	0.983	154.0	13.1
CM11	35	1.022	313.5	71.9	1.002	77.6	10.4	0.977	170.4	14.7
CM12	33	1.025	175.3	68.7	0.999	82.8	1.0	0.977	352.4	21.3
CM13B	13	1.035	59.9	10.6	1.001	155.8	28.6	0.966	311.6	59.2
CM13C	16	1.020	50.6	28.0	1.002	270.3	55.3	0.979	151.0	18.7
CM14	28	1.025	52.9	5.6	1.005	143.9	10.1	0.971	294.2	78.4
CM15	24	1.010	165.0	55.9	1.005	256.6	1.0	0.986	347.3	34.1
CM16	26	1.034	294.5	77.4	1.000	62.6	7.8	0.968	154.0	9.8

Table C.2.   Intensities and   directions   for the   principal axes   of the finite strain ellipsoid for the Chelmsford formation.   D   is the declination and I is the inclination in geographic coor-dinates.

Site	X	D	I	Y	D	I	Z	D	I
CM1	1.384	180.0	53.0	1.080	68.0	16.0	0.668	327.0	33.0
CM2	1.492	186.0	80.0	1.029	73.0	5.0	0.651	342.0	9.0
CM3	1.448	207.0	77.0	1.075	66.0	10.0	0.629	335.0	8.0
CM4	1.275	197.0	53.0	1.107	89.0	13.0	0.708	350.0	34.0
CM5	1.359	252.0	43.0	1.070	59.0	46.0	0.687	156.0	7.0
CM6	1.592	79.0	77.0	1.069	250.0	12.0	0.587	341.0	2.0
CM7	1.221	58.0	38.0	1.149	230.0	52.0	0.713	325.0	4.0
CM9	1.304	74.0	64.0	1.004	248.0	26.0	0.764	349.0	2.0
CM10	1.531	14.0	65.0	1.073	252.0	14.0	0.606	157.0	21.0
CM11	1.478	344.0	78.0	1.071	76.0	1.0	0.633	166.0	12.0

Table C.3. Intensities and directions for the site mean principal axes of the magnetic susceptibility ellipsoid for the Onaping Formation. N is the number of specimens per site, D is the declination and I is the inclination in geographic coordinates.

Site	N	k_{max}	D	I	k_{int}	D	I	k_{min}	D	I
SO1	41	1.077	194.3	65.3	1.042	39.7	22.6	0.896	305.7	9.5
SO2	34	1.399	115.8	64.5	1.022	207.3	0.7	0.706	297.7	25.5
SO3	37	1.410	109.1	63.8	1.037	208.1	4.4	0.695	300.3	25.8
SO4	32	1.643	155.8	71.3	0.894	268.1	7.3	0.705	0.3	17.1
SO5	36	1.642	193.2	73.6	0.967	286.4	0.9	0.658	16.7	16.4
SO6	31	1.410	180.7	62.4	1.155	281.4	5.5	0.625	14.2	27.0
SO7	29	1.042	150.6	48.3	1.018	249.4	7.8	0.943	346.2	40.6
SO8	22	1.034	113.9	58.3	1.007	306.0	31.1	0.963	212.7	5.4
SO9	40	1.047	190.7	64.3	1.001	53.5	19.4	0.955	317.7	16.1
SO10	15	1.002	83.7	70.6	0.999	340.6	4.6	0.998	249.0	18.9
SO11	45	1.292	147.7	57.2	1.021	245.4	4.9	0.789	338.5	32.3
SO12	38	1.727	155.5	45.9	0.981	58.2	7.0	0.604	321.6	43.2
SO13	33	1.442	162.1	45.9	1.069	255.1	2.9	0.660	348.0	43.9
SO14	22	1.011	78.8	77.8	1.000	311.6	7.4	0.990	220.4	9.6
SO16	24	1.214	52.3	74.8	1.021	193.0	11.9	0.823	285.0	9.3
SO17	13	1.020	146.1	81.0	1.006	40.4	2.5	0.975	310.0	8.7
SO18	10	1.149	298.3	72.4	0.955	182.4	7.9	0.913	90.2	15.6
SO19	9	1.036	188.3	48.3	1.008	76.5	18.3	0.958	332.6	35.9
SO20	17	1.034	202.4	1.2	1.015	6.7	46.4	0.954	105.1	7.9

Table C.4.   Normalized intensities and   directions for the magnetic   sus-
ceptibility of the individual samples of the   Chelmsford   For-
mation.   D is the declination and I is the inclination in geo-
graphic coordinates.

Sample	k_{max}	D	I	k_{int}	D	I	k_{min}	D	I
CM1.10	1.043	167.4	64.2	1.002	64.3	5.9	0.957	331.6	25.9
CM2.7	1.028	188.5	66.5	0.999	72.1	11.0	0.973	337.9	20.4
CM4.9	1.014	98.6	63.4	1.004	240.6	21.6	0.983	336.6	14.8
CM8.6	1.029	267.8	77.4	1.003	70.7	12.0	0.968	161.5	3.6
CM9.8	1.014	255.2	30.3	1.000	11.3	36.9	0.986	137.7	38.3
CM10.9	1.023	355.0	68.4	1.003	252.8	4.8	0.974	160.9	21.0
CM11.12	1.031	270.2	66.7	0.995	86.8	23.3	0.975	177.3	1.3
CM12.5	1.036	163.4	62.5	0.994	261.8	4.9	0.971	35414	27.0
CM13.5	1.025	57.0	26.6	0.996	255.4	62.2	0.980	150.8	7.5
CM14.9	1.024	42.1	3.3	0.998	132.7	9.3	0.979	292.9	80.1
CM15.2	1.013	178.7	41.1	0.999	51.9	33.5	0.988	297.4	29.8
CM16.6	1.034	298.0	76.7	0.997	65.8	8.2	0.970	157.3	8.2

Table C.5.   Normalized intensities and   directions for the finite strain of
the individual specimens of the Chelmsford Formation.   D is
the declination and   I is the   inclination in geographic coor-
dinates.

Site	X	D	I	Y	D	I	Z	D	I
CM1	1.620	117.0	67.0	0.980	211.0	1.0	0.630	302.0	23.0
CM2	1.440	232.0	62.0	1.000	124.0	10.0	0.700	29.0	26.0
CM4	1.690	171.0	70.0	0.860	77.0	1.0	0.690	346.0	20.0
CM8	1.460	238.0	69.0	1.090	81.0	19.0	0.630	348.0	7.0
CM9	1.290	282.0	48.0	0.960	183.0	8.0	0.800	85.0	40.0
CM10	1.090	239.0	29.0	1.080	50.0	61.0	0.850	147.0	4.0
CM11	1.500	187.0	71.0	0.890	81.0	5.0	0.750	350.0	18.0
CM12	1.460	173.0	60.0	0.870	45.0	19.0	0.780	307.0	22.0
CM13	1.360	58.0	38.0	0.960	192.0	41.0	0.760	306.0	25.0
CM14	1.330	205.0	24.0	0.920	102.0	26.0	0.820	331.0	53.0
CM15	1.360	107.0	46.0	0.990	216.0	18.0	0.740	321.0	39.0
CM16	1.560	243.0	68.0	0.920	113.0	15.0	0.690	19.0	16.0

REFERENCES

Alvarez W., and Lowrie, W. (1984) Magnetostratigraphy applied to syn-sedimentary slumps, turbidites, and basin analysis: the Scaglia limestone at Furlo (Italy). Geol. Soc. Amer. Bull., 95, pg. 324-336.

Alvarez, W., Colacicchi, R., and Montanari, A. (1985) Synsedimentary slides and bedding formation in Apennine pelagic limestones. Jour. Sed. Petrology, 55, pg. 720-734.

Balsley, J.R., and Buddington, A.F. (1960) Magnetic susceptibility and fabric of some Adirondack granites and orthogneisses. Amer. Jour. Sci., 258-A, pg. 6-20.

Banerjee, S.K. (1971) New grain size limits for paleomagnetic stability in haematite. Nature Phys. Sci., 232, pg. 15-16.

Borradaile, G.F., and Mothersill, J.S. (1984) Coaxial deformed and magnetic fabrics without simply correlated magnitudes of principal values. Phys. Earth Planet. Int., 35, pg. 294-300.

Borradaile, G.F., Mothersill, J., Tarling, D., and Alford, C. (1986) Sources of magnetic susceptibility in a slate. Earth Planet. Sci. Lett., 76, pg. 336-340.

Brocoum, S.J., and Dalziel, I.W.D. (1974) The Sudbury Basin, the Southern Province, the Grenville Front, and the Penokean orogeny. Geol. Soc. Amer. Bull., 85, pg. 1571-1580.

Cantin, R., and Walker, R.G. (1972) Was the Sudbury Basin circular during deposition of the Chelmsford Formation? In: New Developments in the Sudbury Geology; Guy-Bray, J.V. (ed.). Geol. Assoc. Canada, Sp. Pap. Nr. 10, pg. 93-102.

Card, K.D., and Hutchinson, R.W. (1972) The Sudbury structure: Its regional geological setting. In: New Developments in the Sudbury Geology; Guy-Bray, J.V. (ed.). Geol. Assoc. Canada, Sp. Pap. Nr. 10, pg. 67-78.

Centamore, E., Chiocchini, M., Deiana, G., Micarelli, A., and Pieruccini, U. (1971) Contributo alla conoscenza del Giurassico dell' Appennino umbro-marchigiano. Stud. Geol. Cam., 1, pg. 7-89.

Channell, J.E.T., and Horváth, F. (1976) The African/Adriatic promontory as a paleogeographic premise for Alpine orogeny and plate movements in the Carpatho-Balkan region. In: Theory and Experiment Relevant to Geodynamic Processes; Anderson, O.L. and Bolt, B.A. (eds.). Tectonophysics, 35, pg. 71-101.

Channell, J.E.T., and Tarling, D.H. (1975) Paleomagnetism and the rotation of Italy. Earth Planet. Sci. Lett., 25, pg. 177-188.

Channell, J.E.T., Lowrie, W., Medizza, W., and Alvarez, W. (1978) Paleomagnetism and tectonics in Umbria, Italy. Earth Planet. Sci. Lett., 39, pg. 199-210.

Channell, J.E.T., D'Argenio, B., and Horváth, F. (1979) Adria, the African promontory, in Mesozoic Mediterranean paleogeography. Earth Sci. Rev., 15, pg. 213-292.

Chikazumi, S. (1964) Physics of Magnetism. Wiley Publ. Co., New York, 554 pp.

Cirelli, S., Márton, P., and Vigli, L. (1984) Implications of a combined biostratigraphy and paleomagnetic study of the Umbrian Maiolica Formation. Earth Planet. Sci. Lett., 69, pg. 203-214.

Clendenen, W.S. (1986) Finite strain study of the Sudbury Basin. M.Sc. Thesis, University of Colorado, Boulder, Colorado, 253 pp. (Unpublished).

Cogné, J.-P., and Gapais, D. (1986) Passive rotation of hematite during deformation: a comparison of simulated and natural redbeds. Tectonophysics, 121, pg. 365-372.

Cogné, J.-P., and Perroud, H. (1985) Strain removal applied to paleomagnetic directions in an orogenic belt: the Permian red slates of the Alpes Maritimes, France. Earth Planet. Sci. Lett., 72, pg. 125-140.

Colacicchi, R., Passeri, L., and Pialli, G. (1970) Nuovi dati sul Giurese umbro-marchigiano ed ipotesi per un suo inquadrimento regionale. Soc. Geol. It. Mem., 9, pg. 839-874.

Coli, M. (1981) Studio strutturale della "Linea Ancona-Anzio" tra Postat ed Antrodoco (Gole del Velano). Boll. Soc. Geol. It., 100, pg. 171-182.

Collinson, D.W. (1983) Methods in Rock Magnetism and Paleomagnetism. Chapman and Hill, London, 503 pp.

Consiglio Nazionale de Ricerche (1982) Carta strutturale dell'Appennino Settentrionale; Boccaletti, M., and Coli, M. (eds.), Publ. no. 49.

Cox, A., and Doell, R.R. (1960) Review of paleomagnetism. Geol. Soc. Amer. Bull., 71, pg. 647-768.

Curray, J.R. (1956) The analysis of two-dimensional orientation data. Jour. Geol., 64, pg. 117-131.

Daly, L.F. (1967) Anisotropy measurements with a translation inductometer. In: Methods in Paleomagnetism; Collinson, D.W., Creer, K.M., and Runcorn, S.K. (eds.). Elsevier, Amsterdam, pg. 425-428.

D'Argenio, B., and Alvarez, W. (1980) Stratigraphic evidence for crustal thickness changes on the southern Tethyan margin during the Alpine cycle. Geol. Soc. Am. Bull., 91, pg. 681-689.

Dietz, R.S. (1962) Sudbury structure as an astrobleme. Trans. Amer. Geophys. Union, 43, pg. 445-446.

Dietz, R.S. (1964) Sudbury structure as an astrobleme. Jour. Geol., 72, pg. 412-434.

Dunlop, D.J. (1979) On the use of Zijderveld vector diagrams in multi-component paleomagnetic studies. Phys. Earth Planet. Int., 20, pg. 12-24.

Dunnet, D. (1969) A technique of finite strain analysis using elliptical particles. Tectonophysics, 7, pg. 117-136.

Dunnet, D., and Siddans, A.W.B. (1971) Non-random sedimentary fabrics and their modification by strain. Tectonophysics, 12, pg. 307-325.

Eldredge, S., Bachtase, V., and Van der Voo, R. (1985) Paleomagnetism and the orocline hypothesis. Tectonophysics, 119, pg. 153-179.

Faggart, B.E., Jr., Basu, A.R., and Tatsumoto, M. (1985) Origin of the Sudbury complex by meteorite impact: Neodymium isotope evidence. Science, 230, p. 436-439.

Fisch, W.P. (1961) Der Verrucano auf der Nordost-Seite des Sernftales. Mitt. geol. Inst. ETH und Univ. Zürich Ser. C, 84, 88 pp.

French, B.M. (1967) Sudbury structure, Ontario: Some petrographic evidence for origin by meteorite impact. Science, 156, pg. 1094-1095.

French, B.M. (1972) Shock metamorphic features in the Sudbury structure, Ontario: A review. In: New Developments in the Sudbury Geology; Guy-Bray, J.V. (ed.). Geol. Assoc. Canada, Sp. Pap. Nr. 10, pg. 19-28.

Frey, M., Hunziker, J.C., Frank, W., Bocquet, J., Dal Piaz, G.V., Jaeger, E., and Niggli, E. (1974) Alpine metamorphism of the Alps: a review. Schweiz. mineral. petrog. Mitt., 54, pg. 247-290.

Fuller, M.D. (1963) Magnetic anisotropy and paleomagnetism. Jour. Geophys. Res., 68, pg. 293-309.

Fuller, M.D. (1964) On the magnetic fabric of certain rocks. Jour. Geol., 72, pg. 368-376.

Fuller, M.D. (1970) Geophysical aspects of paleomagnetism. Crit. Rev. Solid State Phys., 1, pg. 137- 219.

Geissman, J.W., Van der Voo, R., Kelly, W.C., and Brimhall, G., Jr. (1980) Paleomagnetism, rock magnetism, and aspects of structural deformation of the Butte Mining District, Butte, Montana. Jour. Geol., 88, pg. 129-159.

Ghelardoni, R. (1962) Stratigrafia e tettonica del Trias di M. Malbe presso Perugia. Boll. Soc. Geol. It., 81, pg. 247-256.

Giannini, E., and Lazzarotta, A. (1975) Tectonic evolution of the Northern Apennines. In: Geology of Italy; Squyers, C. (ed.). Earth Sci. Soc. Libyan Arab. Rep., Tripoli, pg. 237-297.

Goree, W.S., and Fuller, M.D. (1976) Magnetometers using RF driven SQUIDS and their applications to rock magnetism and paleomagnetism. Rev. Geophys. Space Phys., 14, pg. 592-608.

Graham, J.W. (1966) Significance of magnetic anisotropy in Appalachian sedimentary rocks. In: The Earth Beneath the Continents; Steinhart, J.S., and Smith, T.J. (eds.). Amer. Geophys. Union, Geophys. Monogr. 10, pg. 627-648.

Graham, R.H. (1978) Quantitative deformation studies in Permian rocks of the Alpes-Maritimes. Mém. Bur. Rech. géol. min. Fr., 91 pg. 219-238.

Granar, L. (1958) Magnetic measurements of Swedish varved sediments. Arkiv för Geofysik, 3, pg. 1-40.

Groshung, R.H., Pfiffner, O.A., and Pringle, L.R. (1984) Strain partitioning in the Helvetic thrust belt of eastern Switzerland from the leading edge to the internal zone. Jour. Structural Geol., 6, pg. 5-18.

Hargraves, R.B. (1959) Magnetic anisotropy and remanent magnetism in hemo-ilmenite from ore deposits at Allard Lake, Quebec. Jour. Geophys. Research, 64, pg. 1565-1578.

Harvey, P., and Laxton, R. (1980) The estimation of finite strain from the orientation distribution of passively deformed linear markers: eigenvalue relationships. Tectonophysics, 70, pg. 285-307.

Heller, F. (1980) Paleomagnetic evidence for Late Alpine rotation of the Lepontine area. Eclog. geol. Helv., 73, pg. 607-618.

Hounslow, M.W. (1985) Magnetic fabric arising from paramagnetic phyllosilicate minerals in mudrocks. Jour. geol. Soc. London, 142, pg. 995-1006.

Hrouda, F. (1976) The origin of cleavage in the light of magnetic anisotropy investigations. Phys. Earth Planet. Int., 13, pg. 132-142.

Hrouda, F. (1979) The strain interpretation of magnetic anisotropy in rocks of the Nízký Jeseník Mountains (Czechoslovakia). Sbor. Geol. Vĕd., 16, pg. 27-62.

Hrouda, F. (1982) Magnetic anisotropy of rocks and its application in geology and geophysics. Geophys. Surveys, 5, pg. 37-82.

Hrouda, F., Stephenson, A., and Woltär, L. (1983) On the standardization of measurements of the anisotropy of magnetic susceptibility. Phys. Earth Planet. Sci., 32, pg. 203-208.

Hrouda, F., and Janák, F. (1976) The change in shape of the magnetic susceptibility ellipsoid during progressive metamorphism and deformation. Tectonophysics, 34, pg. 135-148.

Horner, F.J. (1983) Paleomagnetismus von Karbonatsedimenten der süd-lichen Tethys: Implikationen für die Polarität des Erdmagnetfeldes im unteren Jura und für die Tektonik der ionischen Zone Griechen-lands. Dissertation, ETH-Zürich, 139 pp. (Unpublished).

Huber, R. (1964) Etude géologique du massif du Gufelstock avec strati-graphie du Verrucano. Mitt. Geol. Inst. ETH und Univ. Zürich N.F. 23, 154 pp.

Irving, E. (1977) Drift of major continental blocks since the Devonian. Nature, 270, pg. 304-309.

Irving, E. (1979) Pole positions and continental drift since the Devon-ian. In: Earth: Its Origin, Structure and Evolution; McElhinney, M.W. (ed.). Academic Press, London and New York, pg. 567-593.

Irving, E. and Major, A. (1964) Post-depositional detrital remanent mag-netization in a synthetic sediment. Sedimentology, 3, pg. 135-143.

Johnson, E.A., Murphy, T., and Torrenson, O.W. (1948) Prehistory of the Earth's magnetic field. Terr. Magn. Atmos. Elec., 53, pg. 349-372.

Kent, D.V. (1973) Post-depostional remanent magnetization in deep-sea sediment. Nature, 246, pg. 32-34.

King, R.F. (1955) The remanent magnetization of artificially deposited sediments. Mon. Not. R. astr. Soc. Geophys. Suppl., 7, pg. 115-134.

Kligfield, R., Lowrie, W., and Dalziel, I.W.D. (1977) Magnetic suscep-tibility as a strain indicator in the Sudbury Basin, Ontario. Tec-tonophysics, 40, pg. 287-308.

Kligfield, R., Lowrie, W., and Pfiffner, O.A. (1982) Magnetic proper-ties of deformed oolites from the Swiss Alps: the correlation of magnetic anisotropy and strain. Eclog. geol. Helv., 75, pg. 127-157.

Kligfield, R., Lowrie, W., Hirt, A., and Siddans, A.W.B. (1983) Effect of progressive deformation on remanent magnetization: Permian red beds from the Maritime Alps. Tectonophysics, 97, pg. 59-85.

Kligfield, R., Owens, W., and Lowrie, W. (1981) Magnetic susceptibility anisotropy, strain and progressive deformation in Permian sediments from the Maritime Alps (France). Earth Planet. Sci. Lett., 55, pg. 181-189.

Klootwijk, C.T. (1979a) A summary of paleomagnetism data from extra-peninsular Indo-Pakistan and south central Asia: implications for collision tectonics. In: Structural Geology of the Himalaya; Saklani, P.S. (ed.), pg. 307-360.

Klootwijk, C.T. (1979b) A review of paleomagnetic data from the Indo-Pakistan fragment of Gondwanaland. In: Geodynamics of Pakistan; Farah, A., and DeJong, K.A. (eds.). Geol. Surv. Pakistan, Quetta, pg. 41-80.

Kneen, S.J. (1976) The relationship between the magnetic and strain fabrics of some haematite-bearing Welsh slates. Earth Planet. Sci. Lett., 31, pg. 413-416.

Koopman, A. (1983) Detachment tectonics in the central Apennines, Italy. Geologica Ultraiectina, 30, 155 pp.

Krogh, T.E., Davis, D.W., and Corfu, F. (1984) Chapter 20: Precise U-Pb zircon and baddeleyite ages from the Sudbury area. In: The Geology and Ore Deposits of the Sudbury Structure, Pye, E.G., Naldrett, A.J., and Giblin, P.E. (eds.). Ont. Geol. Surv. Spec. Vol. 1, pg. 431-446.

Kühn, H. (1966) Observations géologiques dans la région du Spitz-meilen. Diploma thesis, ETH-Zürich, 122 pp. (Unpublished).

Lavecchia, G. (1986) A balanced cross-section through the Umbria-Marches fold belt: Kinematic and structural analysis. Third Swiss Tectonic Studies Group Meeting, ETH Zürich, Switzerland (Abstract).

Lavecchia, G. (1981) Appunti per uno schema strutturale dell' Appennino umbro-marchigiano, 3-lo stile deformativo. Boll. Soc. Geol. It., 100, pg. 271-278.

Lavecchia, G., Minelli, G., and Pialli (1984) L'Appennino Umbro-Marchigiano: tettonica distensiva e ipotesi di sismogenesi. Boll. Soc. Geol. It., 103, pg. 467-476.

Lebel, P. (1985) Inbetriebnahme and Verwendung einer Curiewaage. Diploma thesis, ETH-Zürich, 73 pp. (Unpublished).

Lowrie, W. (1968) The magnetic fabric of rocks: a review of the literature, theory, and instrumentation. Gulf Res. & Dev. Co. Technical Mem. No. 4201T8138, 53 pp.

Lowrie, W. (1980) A paleomagnetic overview of the Alpine system. Bureau Recherches Géol. et Min. Mem. Nr. 115, pg. 316-330.

Lowrie, W. (1986) Paleomagnetism and the Adriatic promontory: a reappraisal. Tectonics, 5, pg. 797-808.

Lowrie, W., and Alvarez, W. (1974) Rotation of the Italian peninsula. Nature, 251, pg. 285-288.

Lowrie, W., and Alvarez, W. (1975) Paleomagnetic evidence for rotation of the Italian peninsula. Jour. Geophys. Research, 80, pg. 1579-1592.

Lowrie, W., and Alvarez, W. (1977) Late Cretaceous geomagnetic polarity sequence: detailed rock and paleomagnetic studies of the Scaglia Rossa limestone at Gubbio, Italy. Geophys. J. R. astr. Soc., 51, pg. 561-581.

Lowrie, W., and Alvarez, W. (1984) Lower Cretaceous magnetic stratigraphy in Umbrian pelagic limestone sections. Earth Planet. Sci. Lett., 71, pg. 315-328.

Lowrie, W., and Channell, J.E.T. (1983) Magnetostratigraphy of the Jurassic-Cretaceous boundary in the Majolica limestone (Umbria, Italy). Geology, 12, pg. 44-47.

Lowrie, W., and Hirt, A.M. (1986) Paleomagnetism in arcuate mountain belts. In: The Origin of Arcs, F.-C. Wezel (ed.), Elsevier, Amsterdam, pg. 141-158.

Lowrie, W., and Heller, F. (1982) Magnetic properties of limestones. Rev. Geophys. Space Phys., 20, pg. 171-193.

Lowrie, W., Alvarez, W., Premoli-Silva, I., and Menechi, S. (1980) Lower Cretaceous magnetic stratigraphy in Umbrian pelagic carbonate rocks. Geophys. J.R. astr. Soc., 60, pg. 263-281.

Lowrie, W., Channell, J.E.T., and Heller, F. (1980) On the credibility of remanent magnetization measurements. Geophys. J.R. astr. Soc., 60, pg. 493-496.

Lowrie, W., Hirt, A.M., and Kligfield, R. (1986) Effect of tectonic deformation on the remanent magnetization of rocks. Tectonics, 5, pg. 713-722.

March, A. (1932) Mathematische Theorie der Regelung nach Korngestalt bei affiner Deformation. Z. Kristallogr., 81, pg. 285-297.

Markus, J.H. (1967) Geologische Untersuchungen in den Flumserbergen (St. Galler Oberland). Mitt. geol. Inst. ETH und Univ. Zürich N.F. 71, 119 pp.

Márton, E., and Márton P. (1983) A redefined apparent polar wander curve for the Transdanubian Central Mountains and its bearings on the Mediterranean tectonic history. Tectonophysics, 98, pg. 43-57.

Márton, E., and Veljovic, D. (1983) Paleomagnetism of the Istrian peninsula, Yugoslavia. Tectonophysics, 91, pg. 73-87.

McElhinney, M.W. (1973) Paleomagnetism and Plate Tectonics. Cambridge Univ. Press, Cambridge, 358 pp.

Merrill, R.T., and McElhinney, M.W. (1983) The Earth's Magnetic Field: Its History, Origin and Planetary Perspective. International Geophysical Series, 32, Donn, W.L. (ed.). Academic Press, London, 410 pp.

Micarelli, A., Potetti, M., and Chiocchini, M. (1977) Ricerche micro-biostratigrafiche sulla Maiolica della regione umbro-marchigiana. Stud. Geol. Cam., 3, pg. 57-86.

Milnes, A.G., and Pfiffner, O.A. (1977) Structural development of the Infrahelvetic complex, eastern Switzerland. Eclog. geol. Helv., 70, pg. 83-95.

Milnes, A.G., and Pfiffner, O.A. (1980) Tectonic evolution of the Central Alps in the cross section St. Gallen-Como. Eclog. geol. Helv., 73, pg. 619-633.

Milton, N.J. (1980) Determination of the strain ellipsoid from measurements on any three sections. Tectonophysics, 64, pg. T19-T27.

Morel, P., and Irving, E. (1978) Tentative paleocontinental maps for the early Phanerozoic and Proterozoic. Jour. Geol., 86, pg. 535-561.

Muir, T.L., and Peredery, W.V. (1984) Chapter 7: The Onaping formation. In: The Geology and Ore Deposits of the Sudbury Structure, Pye, E.G., Naldrett, A.J., and Giblin, P.E. (eds.). Ont. Geol. Surv. Spec. Vol. 1, pg. 139-210.

Nagata, T. (1961) Rock Magnetism (2nd Ed.). Maruzen Co., Tokyo, 350 pp.

Naldrett, A.J., Bray, J.G., Gasparrini, E.L., Podolsky, T., and Rucklidge, J.L. (1970) Cryptic variation and the petrology of the Sudbury Nickel Irruptive. Econ. Geol., 65, pg. 122-155.

Néel, L. (1955) Some theoretical aspects of rock magnetism. Adv. Phys., 4, pg. 191-243.

Oberholzer, J. (1933) Geologie der Glarner Alpen. Beitr. geol. Karte Schweiz N.F. 28/I+II, 626 pp.

O'Reilly, W. (1984) Rock and Mineral Magnetism. Blackie, Glasglow, 220 pp.

Owens, W.H. (1974) Mathematical model studies on factors affecting the magnetic anisotropy of deformed rocks. Tectonophysics, 24, pg. 115-131.

Owens, W.H., and Bamford, D. (1976) Magnetic, seismic and other anisotropic properties of rock fabrics. Phil. Trans. Roy. Soc. London, Ser. A, 283, pg. 55-68.

Parry, G.R. (1971) The Magnetic Anisotropy of Some Deformed Rocks. Ph.D. Dissertation, Univ. of Birmingham. (Unpublished).

Peredery, W.V. (1972) Chemistry of fluidal glasses and melt bodies in the Onaping formation. In: New Developments in the Sudbury Geology; Guy-Bray, J.V. (ed.). Geol. Assoc. Canada, Sp. Pap. Nr. 10, pg. 49-60.

Pfiffner, O.A. (1977) Tektonische Untersuchungen im Infrahelvetikum der Ostschweiz. Mitt..geol. Inst. ETH und Univ. Zürich N.F. 217, 423 pp.

Pfiffner, O.A. (1978) Der Falten- und Kleindeckenbau im Infrahelvitikum der Ostschweiz. Eclog. geol. Helv., 71, pg. 61-84.

Pfiffner, O.A. (1981) Fold and thrust tectonics in the Helvetic Nappes (E. Switzerland). In: Thrust and Nappe Tectonics; McClay, K.R., and Price, N.J. (eds.). Spec. Publ. geol. Soc. London 9, London, pg. 319-327.

Porath, H., and Raleigh, C.B. (1967) An origin of the triaxial basal-plane anisotropy in hematite crystals. Jour. Appl. Phys., 38, pg. 2401-2402.

Porath, H., Stacey, F.D., and Cheam, A.S. (1966) The choice of specimen shape for magnetic anisotropy measurements on rocks. Earth Planet. Sci. Lett., 1, pg. 92.

Ramsay, J.G. (1967) Folding and Fracturing of Rocks. McGraw-Hill Book Co., Inc., New York, 568 pp.

Rathore, J.S. (1979) Magnetic susceptibility anisotropy in the Cambrian slate belt of North Wales and correlation with strain. Tectonophysics, 53, pg. 83-97.

Rathore, J.S. (1980) The magnetic fabrics of some slates from the Borrowdale volcanic group in the English Lake District and their correlation with strains. Tectonophysics, 67, pg. 207-220.

Rathore, J.S., and Henry, B. (1982) Comparison of strain and magnetic fabrics in Dalradian rocks from the southwest Highlands of Scotland. Jour. Structural Geol., 4, pg. 373-384.

Reutter, K.J. and Groscurth, J. (1978) The pile of nappes in the northern Apennines, its unravelment and emplacement. In: Alps, Apennines, Hellenides; Closs, H., Roeder, D., and Schmidt, K. (eds.). Naegeli and Obermiller, Stuttgart, pg. 234-243.

Richter, H. (1968) Die Geologie der Guschagruppe im St. Galler Oberland. Mitt. geol. Inst. ETH und Univ. Zürich N.F. 99, 111 pp.

Rousell, D.H. (1972) The Chelmsford formation of the Sudbury Basin - A precambrian turbidite. In: New Developments in the Sudbury Geology; Guy-Bray, J.V. (ed.). Geol. Assoc. Canada, Sp. Pap. Nr. 10, pg. 79-92.

Rousell, D.H. (1975) The origin of foliation and lineation in the Onaping formation and the deformation of the Sudbury Basin. Can. Jour. Earth Sci., 12, pg. 1379-1395.

Rousell, D.H. (1984a) Chapter 5: Structural geology of the Sudbury Basin. In: The Geology and Ore Deposits of the Sudbury Structure, Pye, E.G., Naldrett, A.J., and Giblin, P.E. (eds.). Ont. Geol. Surv. Spec. Vol. 1, pg. 83-99.

Rousell, D.H. (1984b) Chapter 8: Onwatin and Chelmsford formations. In: The Geology and Ore Deposits of the Sudbury Structure, Pye, E.G., Naldrett, A.J., and Giblin, P.E. (eds.). Ont. Geol. Surv. Spec. Vol. 1, pg. 211-218.

Roy, J.L., Reynolds, J., and Sanders, S. (1973) An alternating field demagnetizer for rock magnetism studies. Pub. Earth Phys. Bur., Energy, Mines and Resources, Ottawa, 44, pg. 37-45.

Ryf, W.H. (1965) Geologische Untersuchungen im Murgtal (St. Galler Oberland). Mitt. geol. Inst. ETH und Univ. Zürich N.F. 30, 104 pp.

Schielly, H.P. (1964) Geologische Untersuchungen im Deckengebiet des westlichen Freiberges (Kt. Glarus). Mitt. geol. Inst. und Univ. Zürich N.F. 44, 293 pp.

Schultz-Krutisch, T., and Heller, F. (1985) Measurement of magnetic susceptibility anisotropy in Bundsandstein deposits from southern Germany. Jour. Geophys., 56, pg. 51-58.

Schwartz, S., and Van der Voo, R. (1983) Paleomagnetic evaluation of the orocline hypothesis in the central and southern Appalachians. Geophys. Res. Lett., 10, pg. 505-508.

Schwarz, E.J. (1974) Magnetic fabrics in massive sulfide deposits. Can. Jour. Earth Sci., 11, pg. 1669-1675.

Schwarz, E.J., and Vaughan, D.J. (1972) Magnetic phase relations of pyrrhotite. J. Geomag. Geolelec., 24, pg. 441-458.

Siddans, A.W.B. (1979) Deformation, metamorphism and texture development in Permian mudstones of the Glarus Alps (eastern Switzerland). Eclog. geol. Helv., 72, pg. 601-621.

Siddans, A.W.B., Henry, B., Kligfield, R., Lowrie, W., Hirt, A., and Percevault, M.N. (1984) Finite strain patterns and their significance in Permian rocks of the Alpes Maritimes (France). Jour. Struct. Geol., 6, pg. 339-368.

Smith, A.G., Hurley, A.M., and Briden, J.C. (1981) Phanerozoic Paleocontinental World Maps. Cambridge Univ. Press, Cambridge, 102 pp.

Stacey, F.D., and Banerjee, S.K. (1974) Physical Principals of Rock Magnetism. Elsevier, Amsterdam, 195 pp.

Stevenson, J.S. (1972) The Onaping ash-flow sheet, Sudbury, Ontario. In: New Developments in the Sudbury Geology; Guy-Bray, J.V. (ed.). Geol. Assoc. Canada, Sp. Pap. Nr. 10, pg. 41-48.

Stoner, E.C. (1945) The demagnetization factors for ellipsoids. Phil. Mag., 36, pg. 803-821.

Uyeda, S., Fuller, M.D., Belshé, J.C., and Girdler, R.W. (1963) Anisotropy of magnetic susceptibility of rocks and minerals. Jour. Geophys. Res., 68, pg. 279-291.

Van den Berg, J. (1983) Reappraisal of paleomagnetic data from Gargano (south Italy). Tectonophysics, 98, pg. 29-41.

Van den Berg, J., and Wonders, A.A.H. (1976) Paleomagnetic evidence of large fault displacements around the Po-basin. Tectonophysics, 33, pg. 301-320.

Van den Berg, J., and Zijderveld J.D.A. (1982) Paleomagnetism in the Mediterranean area. In: Alpine Mediterranean Geodynamics; Berkheimer, H., and Hsu, K. (eds.). Geodynamic Series, Amer. Geophys. Union, Washington D.C., 7, pg. 83-112.

Van den Berg, J., Klootwijk, C.T., and Wonders, A.A.H. (1978) The late Mesozoic and Cenozoic movements of the Italian peninsula: further paleomagnetic data from the Umbrian sequence. Geol. Surv. Amer. Bull., 89, pg. 133-150.

Van der Voo, R., and Channell, J.E.T. (1980) Paleomagnetism and orogenic belts. Rev. Geophys. Space Phys., 18, pg. 455-481.

Van der Voo, R., and French, R.B. (1974) Apparent polar wandering for the Atlantic-bordering continents: Late Carboniferous to Eocene. Earth Sci. Rev., 10, pg. 99-119.

Veitch, R.J., Hedley, I.G., and Wagner, J.-J. (1983) Magnetic anisotropy delineator calibration error. Geophys. J.R. astr. Soc., 75, pg. 407-409.

Willis, D. (1977) A kinematic model of preferred orientation. Geol. Soc. Amer. Bull., 88, pg. 883-894.

Wonnacott, R.J., and Wonnacott, T.H. (1985) Introductory Statistics, Fourth Edition. John Wiley and Sons, New York, 649 pp.

Wood, D.S., Oertel, G., Singh, J., and Bennett, H.F. (1976) Strain and anisotropy in rocks. Phil. Trans. Roy. Soc. London, Ser. A, 283, pg. 27-42.

Zijderveld, J.D.A. (1967) A.C. demagnetization of rocks: analysis of results. In: Methods in Paleomagnetism; Collinson, D.W., Creer, K.M., and Runcorn, S.K. (eds.). Elsevier, Amsterdam, pg. 254-286.

Curriculum Vitae

Ann Marie Hirt-Tasillo

Born on July 6, 1955, in Pittsburgh, Pennsylvania, U.S.A., to Edward J. Tasillo, Mechanical Engineer, and Rosemary C., maiden name Holland.

Education

1961-1969   St. Gabriel's Elementary School, Pittsburgh, PA.

1969-1973   St. Francis Academy, Highschool, Pittsburgh, PA.

1973-1974   Duquesne University, Dept. of Education, Pittsburgh, PA.

1974-1977   Waynesburg College, Dept. of Geology, Waynesburg, PA. Bachelor of Science degree, awarded June, 1977, grad. Summa Cum Laude.

1977-1980   University of Toronto, Dept. of Geology, Toronto, Ontario, Canada. Master of Science degree awarded February, 1980. Thesis topic: Paleomagnetism of the Blake River Group, Abitibi Greenstone Belt, Ontario.

1980   Doctoral program, Dept. of Geology, University of Toronto.

1981-1982   Candidate at the Institute for Geophysics, ETH Zürich, Switzerland. Admission examination, passed in July, 1982.

1982-1986   Doctoral student at the Institute for Geophysics, ETH Zürich.

Married to Walter Hirt Jr. since February, 1981.